Investigations of DNA-Mediated Protein Oxidation

Thesis by

Anna Ruth Arnold

In Partial Fulfillment of the Requirements

for the Degree of

Doctor of Philosophy

California Institute of Technology

Pasadena, California

2015

(Defended June 1, 2015)

Acknowledgements

I would first like to thank Professor Jackie Barton, who has been a wonderful advisor during my time at Caltech. Jackie is a pioneer in her field and I feel honored to have contributed to her remarkable collection of research. I always felt excited after talking to her about science, inspired to do the next experiment in order to uncover more information about the system. Jackie has great ideas as well as an ability to help identify important aspects of an experiment, very effectively directing your work. I also really appreciate how strong of an advocate she has always been for me; it is clear that she truly cares about her students. Without Jackie none of this thesis work would have been possible, and I thank her very sincerely for allowing me to be part of her research group.

The other members of my thesis committee have also been integral to my graduate studies: Professors Harry Gray, Doug Rees, and Dave Tirrell. Each of them has been very positive and encouraging throughout my time at Caltech. I especially appreciate how they put me at ease at key meetings, allowing me to focus on the science and enjoy our discussions. I would also like to thank Dr. Angelo Di Bilio, who has worked tirelessly to help me do EPR experiments. He was always available whenever I wanted to do experiments, and was dedicated to making sure the instrument was functioning well.
I also appreciate the instrumentation and expertise available at the Beckman Institute Laser Resource Center (BILRC), with particular thanks to Dr. Jay Winkler. Furthermore, I would

like to acknowledge Mo Renta, the administrative assistant to the Barton group, for all of her efforts in facilitating our research, especially with helping me meet deadlines. A number of other staff members have been particularly helpful during my time at Caltech: Amy Woodall-Ojeda, Agnes Tong, Joe Drew, and Memo Correa. Finally, I would like to thank my collaborator at Stanford, Yang Ha of the Solomon and Hodgson groups, for all of his excellent work in measuring and analyzing our XAS data.

I would like to acknowledge the members of the Barton Group, past and present, for making the lab a good place to work. Overall, labmates have been so helpful: willing to loan you a reagent, negotiate instrument time, or answer your questions. I would especially like to thank Eric Olmon, who was a wonderful mentor to me during my first few years in the lab. Eric taught me how to use the Nd:YAG laser, analyze data, and more generally, inspired me with his meticulous scientific method. Natalie Muren has been so helpful throughout my time at Caltech. She mentored me when I first joined the lab, and helped me through candidacy, my proposals, and writing my thesis.

Many of my good friends have also been my collaborators in the Barton Group. I would especially like to thank Mike Grodick. He is an idea man who always has the time to talk about science: for instance, what results mean and what controls would be best. Mike also constantly adds a dash of ridiculousness and levity to the atmosphere at the lab, which I really appreciate, and he is a great friend. I would like to thank Catrina Pheeney, who along with Mike, I enjoyed working with on our EndoIII multiplexed electrochemistry project. Additionally, I would like to acknowledge Andy Zhou and Phil Bartels, who I have worked

with on other EndoIII projects. Finally, I would like to thank Adam Boynton and Lionel Marcelis. I have had fun doing laser experiments with both of them, and starting TRIR projects with Lionel.

My other friends both within and outside of the Barton group have helped me enjoy my time at Caltech. Hikes with Katie Schaefer and Princess Leia have been really fun as well as taking care of Leia when Katie is out of town. I have also enjoyed the annual Seder at Ariel Furst and Alyson Weidmann's house. Tim Mui has likewise been a good friend; it is always fun to hear about his travel plans and other projects. It has been great spending time with Andrew Wang and Alexis Komor, especially the Game of Thrones parties at their house, and dinners at 101 Noodle Express. I have also enjoyed spending time with some of my other friends: JJ Kang, James Blakemore, Myles Herbert, Nick Swisher, Josh Flores, and Mardig Taslakian.

I would additionally like to thank the chemistry faculty at St. Olaf College, where I obtained my undergraduate degree, especially Professor Gary Miessler. He inspired my interest in inorganic chemistry, with the beauty of symmetry groups and all the information they hold about the physical properties of molecules. Dr. Miessler also connected me with Professor John Enemark, with whom I spent a wonderful year at the University of Arizona. I had not yet had the opportunity to do research in the area of bioinorganic chemistry, but thought that this is where my interests might lie. I wanted some experience before I committed to graduate school, and John allowed me to have a full research experience in his lab and fueled my interest in bioinorganic chemistry. With guidance from the postdocs

Kayunta Johnson-Winters and Asha Rajapakshe, I studied interdomain electron transfer in human sulfite oxidase, and learned many of the techniques that I went on to use in graduate school.

Finally, I would like to thank my amazing family. Thank you to my Dad, Eric, who always told me how proud he is of me, and inspires me with his creativity and work ethic. Thank you to my talented Mom, Beth, for always supporting me throughout my life, and for being the catalyst for all of this graduate work by encouraging me to apply to St. Olaf. I also appreciate each one of my siblings: Catherine, Stephanie and Anders. We are all pursuing very different fields, but we relish the time that we get to spend together when we all travel back to our parent's rural Minnesota home. My time spent on the farm has certainly helped me as I have gone through graduate school.

The biggest thanks of all goes to my wonderful husband, Seth. He has always loved me and supported me in so many ways. When I am working late, he will come and joke around with me and bring me dinner. When I got overwhelmed, he was there to talk things over with me and give perspective. He can even fix equipment in the lab. I have so enjoyed all of our adventures during my time at Caltech: ski trips, late night runs to Donut Man, growing ghost and habanero peppers and making ridiculous hot sauce, and being ill-prepared for hiking Mount Baldy but still making it more than halfway and sharing vodka shots with a friendly stranger. Seth, life with you has been so easy and fun, and you have made this thesis possible.

Abstract

DNA charge transport (CT) involves the efficient transfer of electrons or electron holes through the DNA π-stack over long molecular distances of at least 100 base-pairs. Despite this shallow distance dependence, DNA CT is sensitive to mismatches or lesions that disrupt π-stacking and is critically dependent on proper electronic coupling of the donor and acceptor moieties into the base stack. Favorable DNA CT is very rapid, occurring on the picosecond timescale. Because of this speed, electron holes equilibrate along the DNA π-stack, forming a characteristic pattern of DNA damage at low oxidation potential guanine multiplets. Furthermore, DNA CT may be used in a biological context. DNA processing enzymes with 4Fe4S clusters can perform DNA-mediated electron transfer (ET) self-exchange reactions with other 4Fe4S cluster proteins, even if the proteins are quite dissimilar, as long as the DNA-bound $[4Fe4S]^{3+/2+}$ redox potentials are conserved. This mechanism would allow low copy number DNA repair proteins to find their lesions efficiently within the cell. DNA CT may also be used biologically for the long-range, selective activation of redox-active transcription factors. Within this work, we pursue other proteins that may utilize DNA CT within the cell and further elucidate aspects of the DNA-mediated ET self-exchange reaction of 4Fe4S cluster proteins.

Dps proteins, bacterial mini-ferritins that protect DNA from oxidative stress, are implicated in the survival and virulence of pathogenic bacteria. One aspect of their

protection involves ferroxidase activity, whereby ferrous iron is bound and oxidized selectively by hydrogen peroxide, thereby preventing formation of damaging hydroxyl radicals via Fenton chemistry. Understanding the specific mechanism by which Dps proteins protect the bacterial genome could inform the development of new antibiotics. We investigate whether DNA-binding *E. coli* Dps can utilize DNA CT to protect the genome from a distance. An intercalating ruthenium photooxidant was employed to generate oxidative DNA damage via the flash-quench technique, which localizes to a low potential guanine triplet. We find that Dps loaded with ferrous iron, in contrast to Apo-Dps and ferric iron-loaded Dps which lack available reducing equivalents, significantly attenuates the yield of oxidative DNA damage at the guanine triplet. These data demonstrate that ferrous iron-loaded Dps is selectively oxidized to fill guanine radical holes, thereby restoring the integrity of the DNA. Luminescence studies indicate no direct interaction between the ruthenium photooxidant and Dps, supporting the DNA-mediated oxidation of ferrous iron-loaded Dps. Thus DNA CT may be a mechanism by which Dps efficiently protects the genome of pathogenic bacteria from a distance.

Further work focused on spectroscopic characterization of the DNA-mediated oxidation of ferrous iron-loaded Dps. X-band EPR was used to monitor the oxidation of DNA-bound Dps after DNA photooxidation via the flash-quench technique. Upon irradiation with poly(dGdC)$_2$, a signal arises with $g = 4.3$, consistent with the formation of mononuclear high-spin Fe(III) sites of low symmetry, the expected oxidation product of Dps with one iron bound at each ferroxidase site. When poly(dGdC)$_2$ is substituted with

poly(dAdT)$_2$, the yield of Dps oxidation is decreased significantly, indicating that guanine radicals facilitate Dps oxidation. The more favorable oxidation of Dps by guanine radicals supports the feasibility of a long-distance protection mechanism via DNA CT where Dps is oxidized to fill guanine radical holes in the bacterial genome produced by reactive oxygen species.

We have also explored possible electron transfer intermediates in the DNA-mediated oxidation of ferrous iron-loaded Dps. Dps proteins contain a conserved tryptophan residue in close proximity to the ferroxidase site (W52 in *E. coli* Dps). In comparison to WT Dps, in EPR studies of the oxidation of ferrous iron-loaded Dps following DNA photooxidation, W52Y and W52A mutants were deficient in forming the characteristic EPR signal at g = 4.3, with a larger deficiency for W52A compared to W52Y. In addition to EPR, we also probed the role of W52 Dps in cells using a hydrogen peroxide survival assay. Cells containing W52Y Dps survived the hydrogen peroxide challenge more similarly to those containing WT Dps, whereas cells with W52A Dps died off as quickly as cells without Dps. Overall, these results suggest the possibility of W52 as a CT hopping intermediate.

DNA-modified electrodes have become an essential tool for the study of the redox chemistry of DNA processing enzymes with 4Fe4S clusters. In many cases, it is necessary to investigate different complex samples and substrates in parallel in order to elucidate this chemistry. Therefore, we optimized and characterized a multiplexed electrochemical platform with the 4Fe4S cluster base excision repair glycosylase Endonuclease III (EndoIII). Closely packed DNA films, where the protein has limited surface accessibility, produce

EndoIII electrochemical signals sensitive to an intervening mismatch, indicating a DNA-mediated process. Multiplexed analysis allowed more robust characterization of the CT-deficient Y82A EndoIII mutant, as well as comparison of a new family of mutations altering the electrostatics surrounding the [4Fe-4S] cluster in an effort to shift the reduction potential of the cluster. While little change in the DNA-bound midpoint potential was found for this family of mutants, likely indicating the dominant effect of DNA-binding on establishing the protein redox potential, significant variations in the efficiency of DNA-mediated electron transfer were apparent. On the basis of the stability of these proteins, examined by circular dichroism, we proposed that the electron transfer pathway in EndoIII can be perturbed not only by the removal of aromatic residues but also through changes in solvation near the cluster.

While the 4Fe4S cluster of EndoIII is relatively insensitive to oxidation and reduction in solution, we have found that upon DNA binding, the reduction potential of the $[4Fe4S]^{3+/2+}$ couple shifts negatively by approximately 200 mV, bringing this couple into a physiologically relevant range. Demonstrated using electrochemistry experiments in the presence and absence of DNA, these studies do not provide direct molecular evidence for the species being observed. Sulfur K-edge X-ray absorbance spectroscopy (XAS) can be used to probe directly the covalency of iron-sulfur clusters, which is correlated to their reduction potential. We have shown that the Fe-S covalency of the 4Fe4S cluster of EndoIII increases upon DNA binding, stabilizing the oxidized $[4Fe4S]^{3+}$ cluster, consistent with a negative shift in reduction potential. The 7% increase in Fe-S covalency corresponds to an

approximately 150 mV shift, remarkably similar to DNA electrochemistry results. Therefore we have obtained direct molecular evidence for the shift in 4Fe4S reduction potential of EndoIII upon DNA binding, supporting the feasibility of our model whereby these proteins can utilize DNA CT to cooperate in order to efficiently find DNA lesions inside cells.

In conclusion, in this work we have explored the biological applications of DNA CT. We discovered that the DNA-binding bacterial ferritin Dps can protect the bacterial genome from a distance via DNA CT, perhaps contributing to pathogen survival and virulence. Furthermore, we optimized a multiplexed electrochemical platform for the study of the redox chemistry of DNA-bound 4Fe4S cluster proteins. Finally, we have used sulfur K-edge XAS to obtain direct molecular evidence for the negative shift in 4Fe4S cluster reduction potential of EndoIII upon DNA binding. These studies contribute to the understanding of DNA-mediated protein oxidation within cells.

Contents

List of Figures

List of Tables and Equations

Tables

Equations

Chapter 1

DNA-Mediated Charge Transport

1.1 Introduction

DNA is canonically known as the repository for genetic information in the cell. Individual strands of DNA consist of a phosphate-deoxyribose backbone connecting nitrogenous bases, either purines (adenine and guanine) or pyrimidines (cytosine and thymine). These individual DNA strands assemble into a right-handed double helical structure according to the hydrogen bonding of the bases: adenine with thymine and guanine with cytosine. The sequence of the nitrogenous bases encodes for proteins according to the central dogma of molecular biology (*1*). Herein, DNA is transcribed into messenger RNA (mRNA), which can then be translated into proteins at the ribosome according to three base codons that correspond to specific amino acids. Chains of amino acids compose proteins, which catalyze important reactions in the cell, such as oxidative phosphorylation to form ATP, the ubiquitous cellular energy currency (*2*).

The nitrogenous bases of DNA are composed of aromatic rings with base-pairs spaced 3.4 Å apart in the double helix (Figure 1). This structure allows the electron density of adjacent bases to overlap, a phenomenon referred to as π-stacking. Significant structural similarity exists between stacked base-pairs in DNA and the z-direction of graphite, a known conductive material. Specifically, the gap between adjacent graphene sheets is 3.354 Å (*3*). The similar spacing of aromatic moieties in graphite and DNA led researchers to hypothesize that DNA could also be conductive.

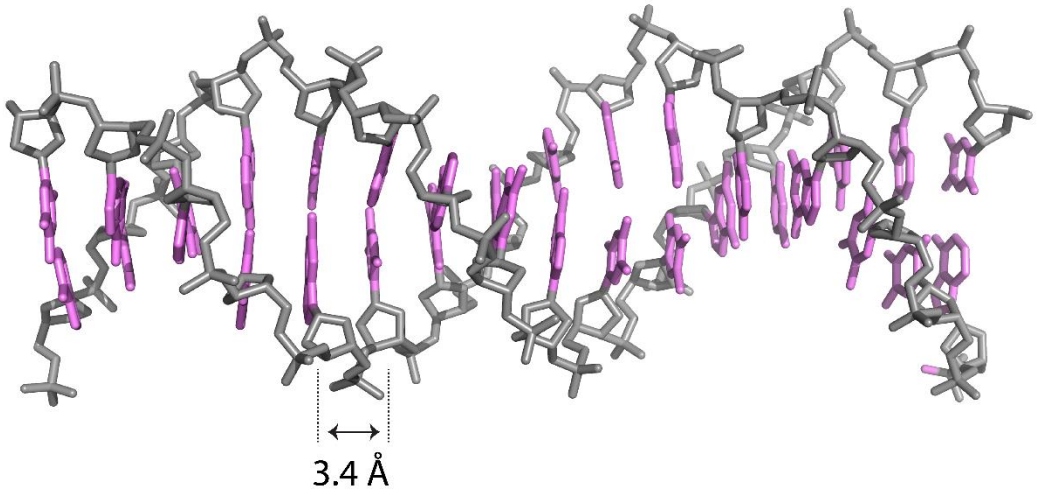

Figure 1. DNA structure with aromatic base-pairs spaced 3.4 Å apart in the double helix. Phosphate-deoxyribose backbone shown in gray, nitrogenous bases in purple. PDB: 3BSE.

1.2 DNA Charge Transport

Decades of research have now established that DNA can indeed conduct charge through the π-stack of the nitrogenous bases in a process termed DNA charge transport (CT) (*4*). Thus in addition to its role as the repository for genetic information, DNA is conductive. Electrons as well as electron holes are efficiently transported through the DNA π-stack (*5*). However, DNA CT is attenuated by disturbances in π-stacking that can occur through DNA mismatches or lesions as well as through protein binding events that significantly bend the DNA (*6-10*). Conversely, nicks in the phosphate-deoxyribose backbone do not impede DNA CT (*11*).

Various platforms for investigating DNA CT have been developed in the Barton group; two of the most effective platforms consist of DNA photooxidant systems in solution (Figure 2), and electrochemistry on DNA monolayers. DNA photooxidants generally contain a planar, aromatic moiety that binds to the DNA via intercalation, wherein the planar photooxidant inserts between two adjacent base-pairs, forming a sandwich-like complex that allows π-stacking between the photooxidant and the DNA bases (*12*). Irradiation of the photooxidant typically produces an excited state that is sufficiently oxidizing and long-lived to withdraw an electron from DNA. Examples of metallointercalators include $[Rh(phi)_2(bpy')]^{3+}$, $[Ru(phen)(bpy')(dppz)]^{2+}$ (which requires a diffusing oxidative quencher to produce a ground state Ru^{3+} oxidant), $[Re(CO)_3(dppz)(py')]^{+}$, and $[Ir(ppy)_2(dppz')]^{+}$, where phi = 9,10-phenanthrenequinone diamine, bpy′ = 4-methyl-4′-(butyric acid)-2,2′-bipyridine, phen = 1,10-phenanthroline,

dppz = dipyrido[2,3-a:2′,3′-c]phenazine, py′ = 3-(pyridin-4-yl)-propanoic acid, ppy = 2-phenylpyridine, and dppz′ = 6-(dipyrido[3,2-a:2′,3′-c]phenazin-11-yl)hex-5-ynoic acid) (*13-15*). The yield of oxidative DNA damage produced by metallointercalators has been found to depend primarily on the thermodynamic driving force for CT, the efficiency of back electron transfer (ET) processes, and the degree of electronic coupling to the DNA π-stack (*15*). These complexes can be covalently tethered to amine-modified DNA via the carboxylic acid moiety appended to either the intercalating (dppz′) or ancillary ligands (bpy′, py′) in order to localize the complex to one end of the DNA (*16*). Organic intercalators such as ethidium and anthraquinone have also been utilized successfully as DNA photooxidants (*13*).

An elegant example of the application of metallointercalators to the study of DNA CT employed intercalating donor $[Ru(phen')(dppz)]^{2+}$ and acceptor $[Rh(phi)_2(phen')]^{3+}$ complexes, where phen′ = 5-amido-glutaric acid-1,10-phenanthroline, covalently tethered to opposite ends of a 15-mer DNA duplex (*17*). $[Ru(phen')_2(dppz)]^{2+}$ is a DNA light-switch complex: whereas its luminescence is quenched in aqueous solution, upon the addition of DNA the ruthenium complex luminesces intensely (*18*). However, when $[Rh(phi)_2(phen')]^{3+}$ is appended to the opposite strand, the DNA-bound $[Ru(phen')_2(dppz)]^{2+}$ luminescence is completely quenched (*17*). Nanosecond time-resolved luminescence experiments were too slow to observe this quenching process. Extensive control experiments, including those that ruled out intermolecular events, coupled with the improbability of energy transfer confirmed that this quenching is due to rapid intramolecular

DNA-mediated electron transfer between the metal complexes, from the

$^*[Ru(phen')_2(dppz)]^{2+}$ excited state to the rhodium complex.

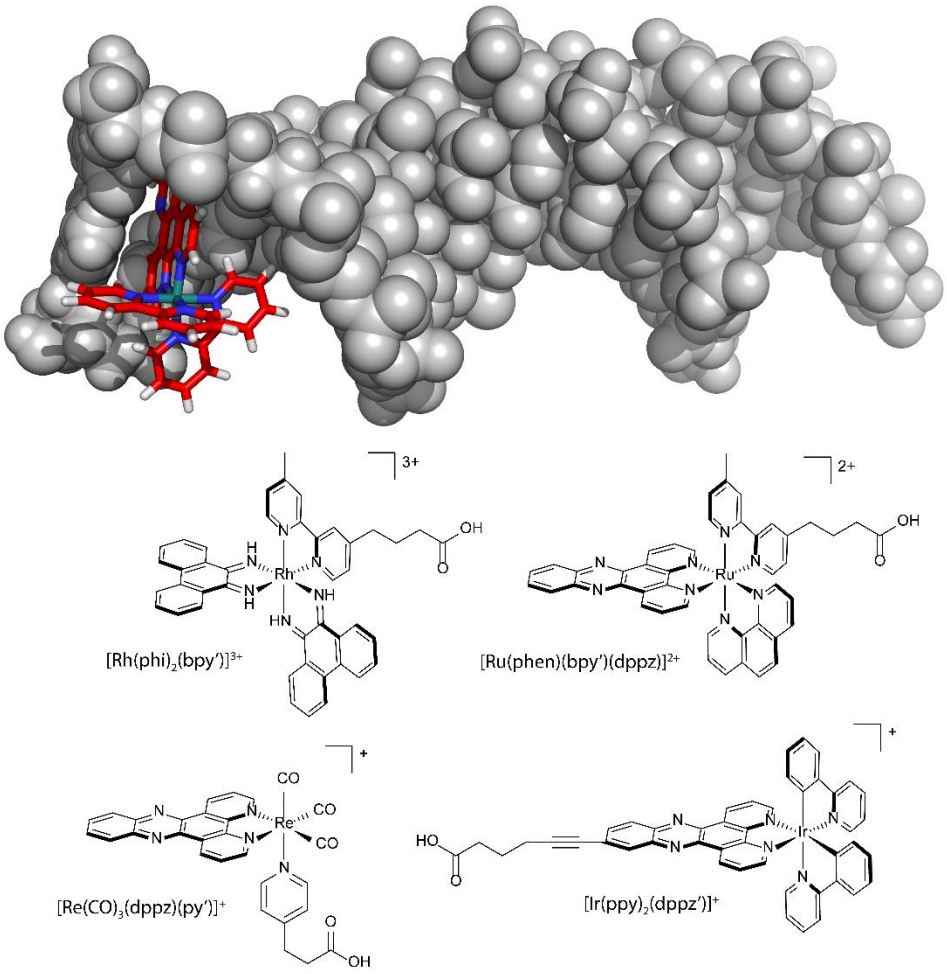

Figure 2. Structures of metallointercalator photooxidants. *Upper*: Crystal structure demonstrating intercalative DNA binding mode with Δ-$[Ru(bpy)_2(dppz)]^{2+}$. Figure created by combining PDB files 3BSE and 4E1U. *Lower*: Examples of commonly used photooxidants: $[Rh(phi)_2(bpy')]^{3+}$, $[Ru(phen)(bpy')(dppz)]^{2+}$ (which requires a diffusing oxidative quencher to produce a ground state Ru^{3+} oxidant), $[Re(CO)_3(dppz)(py')]^{+}$, and $[Ir(ppy)_2(dppz')]^{+}$. Metallointercalators can be tethered to amine-modified DNA via the carboxylic acid moiety appended from the ancillary or intercalating ligand.

1.2.1 Kinetics of DNA CT

Subsequent experiments explored electron transfer between non-covalently bound, intercalated ruthenium and rhodium metal complexes with picosecond spectroscopy (*19*). Even on the picosecond timescale, DNA-mediated charge transport between the metal complexes was faster than the instrumental resolution, with a large decrease in the ruthenium emission intensity at zero time. However, these studies established a lower limit for the electron transfer rate of 3×10^{10} s^{-1} (*19*). Femtosecond transient absorption experiments were finally able to directly observe DNA-mediated electron transfer (*20*). Here, the intercalator ethidium was tethered to one end of the DNA, and the modified base 7-deazaguanine was positioned at varying distances from the ethidium, with either two, three or four intervening base-pairs (10, 14, 17 Å, respectively). Ethidium has a sufficient reduction potential in the excited state (1.2 V versus NHE) to oxidize 7-deazaguanine (1.0 V oxidation potential) but not the other DNA bases, which have higher oxidation potentials. In this study, ethidium was excited using a laser pulse at 500 nm, and a second pulse at 400 nm was used to probe how the absorption of the sample changed as a result of laser excitation (*20*). DNA sequences with guanine substituted for 7-deazaguanine exhibit a lifetime of about 2 ns, corresponding to the inherent rate of decay of the DNA-bound ethidium excited state in the absence of any quenching due to electron transfer. Sequences instead containing 7-deazaguanine show additional 5 ps and 75 ps decay components that can be ascribed to thermodynamically favorable electron transfer from 7-deazaguanine to the ethidium excited state. Fluorescence anisotropy experiments correlated the slower electron

transfer process (75 ps) with the rotation of ethidium in DNA. Therefore, two electron transfer rates were observed that correspond to different ethidium orientations: the 5 ps rate corresponds to an ethidium orientation that is favorable for ET, whereas the slower 75 ps rate corresponds to an initially unfavorable conformation that requires reorientation or rotation of the ethidium in order for ET to occur (*20*). Importantly, the rates of electron transfer are unaffected by donor-acceptor distance from 10 to 17 Å. However, the efficiency of ET was observed to decrease with increasing distance, implicating structural dynamics likely due to the increased probability of transient disorder in stacking, and thus electronic coupling, at longer distances. Overall, this study demonstrated the ultrafast nature of favorable electron transfer through DNA, as well as the shallow distance dependence of the ET rate.

1.2.2 Mechanism and characteristics of DNA CT

Further work has elucidated important aspects of the mechanisms involved in DNA charge transport (*21*). Superexchange involves coherent orbital-mediated tunneling along the entire DNA bridge between the donor and acceptor, and displays an exponential dependence of the rate of electron transfer on distance. This substantial distance dependence with a superexchange mechanism is inconsistent with the fast electron transfer rates that have been measured over relatively long molecular distances (*21*). For example, the DNA-mediated electron transfer from excited $[Ru(phen')(dppz)]^{2+}$ to $[Rh(phi)_2(phen')]^{3+}$ occurs over a distance of 41 Å within just 3 nanoseconds (*17*). Instead, an incoherent hopping mechanism, where there is some intermediate state of charge localization on the bridge, is

more likely for charge transport through DNA because of its more shallow linear distance dependence. However, localized hopping on individual bases is difficult to rationalize with a number of experimental observations (*21*). One of the first clues that pointed towards a delocalized hopping mechanism illustrated the importance of base dynamics by uncovering the temperature dependence of electron transfer through DNA (*22*). In transient absorption experiments with the photooxidant base analog 2-aminopurine as the acceptor and guanine as the electron donor, the rate of ET increased with increasing temperature until duplex melting (*22*). These experiments suggest conformational gating to reach a CT-active state that is enhanced by the increased dynamical motions that modulate electronic coupling at higher temperatures. A periodic length dependence has also been observed in DNA CT (*23-25*). The yield of ET through varying lengths of adenine tracts has been measured by use of a photooxidant with N^2-cyclopropylguanosine (^{CP}G); as the resulting ^{CP}G radical cation undergoes rapid ring opening, the yield of decomposition due to ET can be quantified (*23*,*24*). These studies found an oscillatory component to the distance dependent ET yield with a period of 3 to 4 bases. This result was rationalized by an incoherent CT mechanism wherein charge is delocalized over domains of 3 to 4 bases. Thus, CT is facilitated when the length of the sequence is an integer multiple of these domains, and is less favorable when this is not the case. More recent work by Tao and coworkers investigated the resistance of duplexed DNA between two electrodes (*25*). They found that the resistance of the DNA circuit increases linearly with distance, and observed a periodic oscillation with a period of 2 to 3 bases in sequences with stacked GC base-pairs (*25*). Overall, these experiments suggest

a model for the mechanism of DNA CT. Electron transfer through DNA is best described as an incoherent hopping mechanism, consisting of multiple superexchange steps between delocalized (approximately 3 base pair) domains of well-coupled stacked bases. These CT-active domains of stacked bases are created through conformational dynamics of the bases that modulate their electronic coupling. This mechanism also explains why a mismatch or lesion would attenuate DNA CT: it perturbs the formation of these well-coupled 3 base pair delocalized domains.

A characteristic pattern of oxidative DNA damage results when electron holes are injected into the DNA π-stack with a photooxidant complex such as those described above. Guanine is the most easily oxidized of the DNA bases with an oxidation potential of 1.31 V versus NHE compared to adenine, thymine, and cytosine with potentials of 1.42 V, 1.45 V, and 1.50 V, respectively (*26*). The presence of adjacent guanines can further lower the guanine oxidation potential. Molecular orbital calculations revealed that, of all of the combinations of two stacked bases in DNA, GG/CC has the lowest ionization potential with 70% of the highest occupied molecular orbital (HOMO) localized on the 5′-G of the guanine doublet (*27*). The localization of DNA damage was mapped experimentally using a photosensitizer followed by treatment with hot piperidine (*28*). Piperidine cleaves the DNA backbone at sites of oxidative guanine lesions, as well as abasic sites and other chemical modifications (*29*). This study confirmed that guanine doublets and triplets are electron hole sinks within DNA. Work by Barton and coworkers demonstrated that oxidative damage can be generated from a distance via DNA charge transport, and that this damage is

localized to low potential guanine multiplets (*30*,*31*). Here metallointercalating photooxidants were covalently tethered to one end of the DNA duplex, ensuring spatial separation between the photooxidant and the guanine doublet. Both $[Rh(phi)_2(bpy')]^{3+}$, which is competent to directly abstract electrons from DNA when excited at 365 nm (*30*), and $[Ru(phen)(bpy')(Me_2dppz)]^{2+}$ (where Me_2dppz = 9,10-dimethyl-dipyridophenazine), which requires a diffusing oxidative quencher to produce a ground state Ru^{3+} oxidant in a process known as the flash-quench technique (*31*), were investigated. After irradiation and piperidine treatment of radiolabeled DNA, in both cases damage was observed predominantly at the 5′-G of a guanine doublet located approximately 37 Å away from the site of metallointercalation. Because the timescale of DNA CT (picoseconds) is much faster than the formation of permanent oxidative lesions, the injected electron hole can equilibrate along the base-pair π-stack and localize to the low potential guanine doublet. Thus the pattern of oxidative damage to guanine multiplets is a characteristic of damage from a distance via DNA CT.

The formation of guanine radicals using the flash-quench technique has also been directly observed using transient absorption and EPR spectroscopic methods (*32*,*34*). Nanosecond transient absorption experiments investigated Δ-$[Ru(phen)_2(dppz)]^{2+}$ with a variety of diffusing oxidative quenchers: $[Ru(NH_3)_6]^{3+}$, methyl viologen, and $[Co(NH_3)_5Cl]^{2+}$ (*32*). After the "flash" of laser excitation, the $*Ru^{2+}$ excited state is oxidatively "quenched" by these diffusing species to yield an intercalated ground state Ru^{3+} species with a reduction potential of 1.6 V versus NHE (*33*). In the presence of poly(dAdT) DNA, ruthenium

complex, and diffusing quencher, a long-lived transient ascribed to the decay of the Ru^{3+} species is observed (*32*). However, when poly(dG-dC) is substituted for poly(dA-dT), the long-lived Ru^{3+} transient disappears. Instead, the UV-visible absorbance difference spectrum indicates formation of the neutral guanine radical with maxima at 390 and 550 nm; thus, once formed, the guanine radical cation undergoes rapid deprotonation. The kinetics of the Ru^{2+}* emission decay correspond to the rise of the guanine radical transient, indicating a sequential process. In mixed sequence DNA, the neutral guanine radical transient is long-lived, decaying on a millisecond timescale. Additionally, because $[Co(NH_3)_5Cl]^{2+}$ irreversibly labilizes upon reduction, BET events are inhibited and the highest quantum yield of damage is obtained among the different quenchers (*32*). Guanine radical formation via flash-quench has also been directly monitored spectroscopically via EPR (*34*). When anaerobic samples containing $[Ru(phen)_2(dppz)]^{2+}$, $[Co(NH_3)_5Cl]^{2+}$, and either mixed sequence or poly(dG-dC) DNA were measured at room temperature under continuous irradiation, a signal with an isotropic *g*-value of 2.0048 was observed, whereas this signal was not observed with poly(dA-dT) DNA. These experiments laid the foundation for future studies of DNA-mediated protein oxidation initiated by DNA photooxidation.

1.2.3 DNA electrochemistry

In addition to DNA photooxidant systems in solution, the other major platform that has been effectively used to study DNA CT in the Barton group is electrochemistry on DNA monolayers (Figure 3). Typically, a single strand of DNA is modified with a terminal alkanethiol moiety and annealed to its complementary strand. These thiol-modified DNA

duplexes can then be self-assembled into DNA monolayers on gold electrode surfaces, forming covalent gold-thiol bonds (*35*). Monolayers can be assembled in the absence and presence of $MgCl_2$ to create low and high density monolayers, respectively (*36*). More recently, click chemistry methods have been utilized to enable controlled variation in the amount of DNA on the surface, while concurrently producing more evenly spaced monolayers (*37*). Finally, DNA can also be functionalized with pyrene to form DNA monolayers on highly oriented pyrolytic graphite (HOPG), allowing for a wider potential window than gold electrodes (*38*).

After DNA monolayer formation, a DNA-bound redox probe can be exploited to investigate DNA CT on a surface. Here again, stacking of the redox probe with the DNA base-pair π-stack to facilitate electronic coupling is vital (*39*). The intercalated redox probe may also be covalently tethered to the distal end of the DNA relative to the electrode surface; in this case, the nature of the linkage to the DNA is also important (*40*). Long, saturated linkages do not maintain electronic coupling to the DNA π-stack, in contrast to short, unsaturated linkages which preserve this coupling (*40*). Organic dyes such as nile blue and methylene blue have been commonly used as redox probes (*35*,*36*,*41*). In these systems, charge can flow directly from the electrode to the redox probe, or charge can be conducted in a DNA-mediated fashion, flowing from the electrode through the alkane-thiol tether and the DNA π-stack to reach the redox probe. A DNA-mediated mechanism can be demonstrated by comparing well-matched DNA with DNA that contains a mismatch or abasic site; the disruption to the base pair π-stacking attenuates the amount of charge that reaches the redox

probe. The DNA-mediated pathway can be favored by surface passivation with a backfilling agent such as 6-mercaptohexanol, as well as the use of closely packed monolayers and covalently tethered redox probes with short linkages (*36*). Electrochemical charge transport through the DNA π-stack can occur well below the potential of the DNA bases, likely due to charge delocalization (*21*).

Additionally, redox-active DNA-binding proteins may be utilized as redox probes on DNA-modified electrodes. MutY, a 4Fe4S cluster-containing base excision repair (BER) protein, was the first protein to be thus investigated (*42*). Importantly, these studies were able to determine the DNA-bound redox potential of MutY. The observed redox potential of 90 mV versus NHE was assigned to the $[4Fe4S]^{3+/2+}$ couple, and is consistent with potential ranges for high potential iron-sulfur proteins (HiPIPs). The DNA-mediated nature of the electrochemical signal was confirmed through abasic site discrimination. Finally, a MutY mutant, C199H, where one of the ligating cysteine residues of the 4Fe4S cluster was changed to a histidine, was assayed. C199H MutY displayed a redox potential of 65 mV versus NHE, a negative shift relative to the WT protein as expected for histidine ligation (*42*). This mutant experiment confirmed the iron-sulfur cluster as the origin of the observed electrochemical signal. DNA-modified electrodes have proven a valuable tool for investigating DNA-binding redox-active proteins; their application will be further described in the next section.

DNA electrochemistry experiments have directly demonstrated the shallow distance dependence of DNA charge transport (*41*). Multiplexed chips have been developed that

allow for simultaneous investigation of up to four different types of DNA on a single gold surface with four-fold redundancy (*43*). The multiplexed chips are composed of sixteen individually addressable gold electrodes divided into four quadrants. An elegant application of these chips compared DNA charge transport between 17-mer and 100-mer duplexes covalently modified on the distal end with a nile blue redox probe (*41*). When a chip was modified with half well-matched 100-mer duplex, and half that contained a single C:A mismatch, CT was significantly attenuated even over this long distance. Quantified as cathodic cyclic voltammetry peak area, the ratio of well-matched to mismatched surfaces was 2.3 ± 0.4, similar to what had previously been observed with much shorter DNA duplexes. A second chip was modified with well-matched 100-mer, mismatched 100-mer and well-matched 17-mer DNA and ET kinetics were estimated by measuring the scan-rate dependence of the peak splitting (*41*). The extracted ET rates of 25 - 40 s^{-1} were indistinguishable between the 17-mer and 100-mer duplexes, indicating that tunneling through the alkanethiol tether is rate-limiting (consistent with earlier work, *44*) while ET through the DNA π-stack is rapid. This lower limit for ET through a 100-mer DNA duplex allowed for an estimate of β, an exponential decay parameter characteristic of electronic coupling efficiency that describes the decrease in ET rate with increasing distance between donor and acceptor. The estimated β value for DNA was 0.05 $Å^{-1}$, indicating a much shallower distance dependence than that observed in proteins, where β ranges from 0.85 to 1.5 $Å^{-1}$, with an average value of approximately 1.1 $Å^{-1}$ (*45*). Furthermore, the conformation of the 100-mer duplex on the electrode surface was investigated by cutting with a sequence-

specific restriction enzyme (*41*). Comparing 100-mer duplexes with a restriction site to 17-mer duplexes without such site, almost complete attenuation (90% of the cathodic peak area) of the 100-mer electrochemical signal was observed after incubation with the restriction enzyme as the nile blue-modified section is cleaved and released into solution, while the 17-mer electrochemical signal was unaffected. This established the biologically relevant conformation of the 100-mer DNA on the electrode surface. Overall, this DNA electrochemistry experiment directly demonstrated that charge can be efficiently transported through DNA over long molecular distances, at least up to 100 base-pairs or 34 nm.

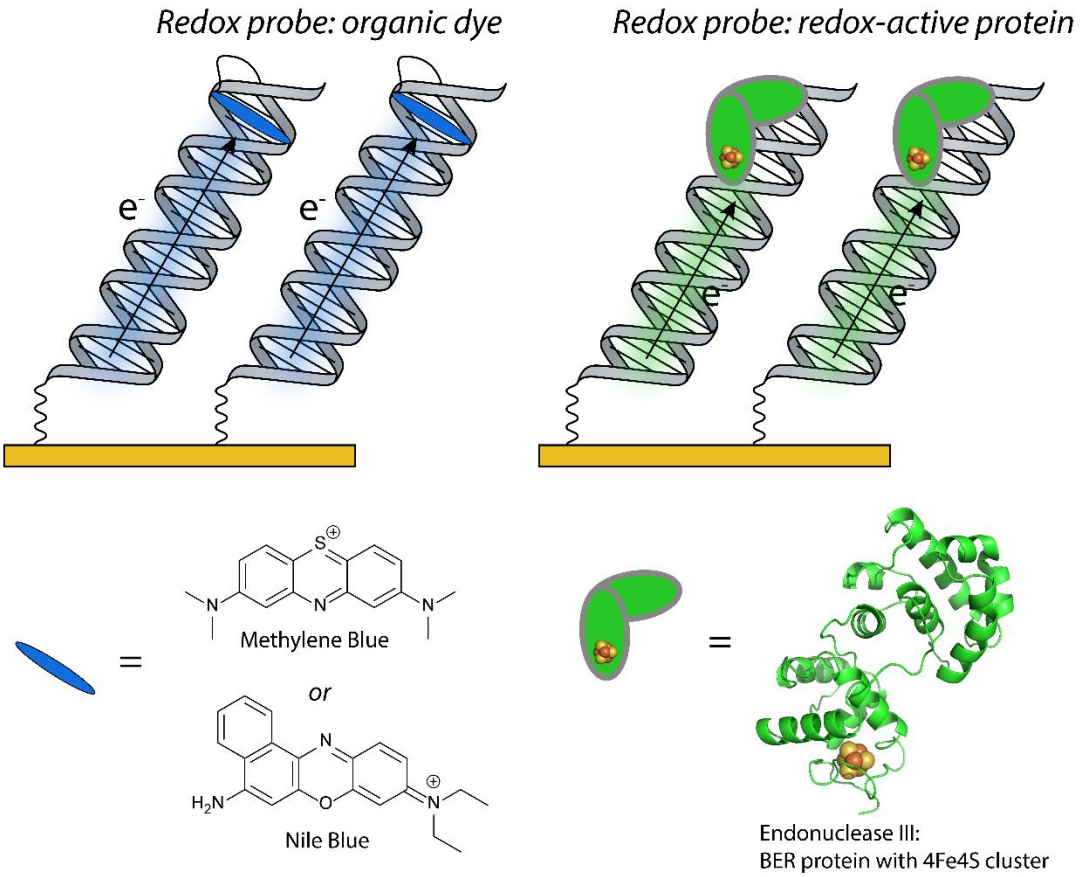

Figure 3. Applications of DNA electrochemistry. DNA monolayers assembled on gold electrodes can be used to probe the ground state DNA-mediated oxidation and reduction of redox probes such as intercalated organic dyes methylene blue or nile blue (*left*) as well as DNA-bound redox active proteins (*right*). Shown is the base excision repair glycosylase Endonuclease III that contains a 4Fe4S cluster. PDB: 2ABK.

1.3 Biological DNA CT

The discovery of the remarkable conductivity of DNA led to speculation about whether DNA CT could be relevant in a biological context inside cells. Because the neutral guanine radical has a relatively long lifetime in DNA (*32*), there is the possibility for interaction with redox-active peptides or proteins that are electronically coupled into the DNA π-stack. This was first demonstrated in proof of principle experiments with the tripeptides KWK and KYK (*46*,*47*), where the aromatic tyrosine (Y) or tryptophan (W) residue intercalates into the π-stack while positively charged lysine (K) residues assist in binding to negatively charged DNA. The oxidation of tyrosine (0.9 V versus NHE) and tryptophan (1.0 V versus NHE) by guanine radical are thermodynamically favorable. Using the flash-quench quench technique with mixed sequence DNA, $[Ru(phen)_2(dppz)]^{2+}$, $[Ru(NH_3)_6]^{3+}$ and KWK, nanosecond transient absorption experiments were used to observe a positive transient at 510 nm that could be assigned to the neutral tryptophan radical given its strong dependence on peptide concentration (*46*). This transient was not present when any of the necessary components (DNA, quencher, or peptide) were omitted. Is this tryptophan oxidation DNA-mediated? First, the peptide itself does not quench the DNA-bound $[Ru(phen)_2(dppz)]^{2+}$ excited state, confirming the absence of direct electron transfer from tryptophan to $*Ru^{2+}$. Given that the free $*Ru^{2+}$ is rapidly quenched (ps) in aqueous solution in the absence of DNA (*18*), further studies compared poly(dA-dT) and poly(dG-dC) DNA. With poly(dG-dC), the rise of the tryptophan radical positive transient at 510 nm corresponds to the disappearance of the guanine radical transient at 373 nm, suggesting

that guanine radical is a necessary intermediate in tryptophan oxidation. In contrast, no positive transient was observed at 510 nm with poly(dA-dT), likely because of fast BET with the diffusing quencher. This control demonstrates that there is no direct contact of KWK with the ground state $[Ru(phen)_2(dppz)]^{3+}$ oxidant. Therefore tryptophan oxidation appears to be mediated by guanine radicals (*46*). Combined with similar experiments using the tripeptide KYK that monitored tyrosine radical formation at 405 nm (*47*), these studies paved the way for work on DNA-mediated protein oxidation.

Indeed, DNA-mediated protein oxidation was soon demonstrated with the methyltransferase HhaI (*48*). This enzyme flips out the central cytosine of its target sequence 5′-GCGC-3′ for methylation, inserting a glutamine side chain (residue 237) into the DNA pocket. Transient absorption experiments with the flash-quench technique utilized a Q237W HhaI mutant, where the intercalating glutamine residue is replaced with aromatic tryptophan. Like studies with the tripeptide KWK, a positive transient corresponding to the neutral tryptophan radical was observed at 510 nm with Q237W HhaI. Here, the ruthenium photooxidant was covalently tethered away from the methylation site, ensuring DNA-mediated tryptophan oxidation. Furthermore, when the distance between the intercalated ruthenium photooxidant and the methylation site is increased from 24 to 51 Å, there was no variation in the rate of transient formation, indicating that CT through the DNA is not rate-limiting (*48*).

1.3.1 Coordination of iron-sulfur cluster DNA processing enzymes via DNA CT

But how could DNA charge transport be used by proteins inside the cell? Following the work with *E. coli* MutY (*42*), other BER proteins with 4Fe4S clusters were discovered to have similar DNA-bound $[4Fe4S]^{3+/2+}$ reduction potentials, including *E. coli* Endonuclease III (EndoIII) and uracil DNA glycosylase (UDG) from *Archeoglobus fulgidus* (*49*). As the first step in the BER pathway, these glycosylase enzymes target and excise specific oxidized lesions within the genome. MutY removes adenine base-paired with 7,8-dihydro-8-oxoguanine (8-oxoG), a result of inaccurate replication of DNA with 8-oxoG, while EndoIII targets oxidized pyrimidines (*50*). After excision of the oxidized or incorrect base to create an abasic site, glycosylase activity is followed by the remaining steps in the BER pathway to restore the integrity of the DNA. While the mechanistic details of glycosylase enzymes once they have found their substrates are relatively well understood (*51*), how the search is efficiently coordinated is less clear given their low copy numbers in the cell. In *E. coli*, there are an estimated 500 copies of EndoIII, and only approximately 30 copies of MutY (*52*). Given their low copy numbers and the vast quantity of DNA that they must search, diffusion-only search models are simply too slow to permit scanning of the entire genome within the doubling time of *E. coli* (*53*).

Could the 4Fe4S cluster of these glycosylase enzymes be involved in the search process? The $[4Fe4S]^{2+}$ cluster of EndoIII is relatively insensitive to reduction and oxidation in solution (*54*), leading to a proposed structural role for the cluster although it is not required for folding or stability in the homologous enzyme MutY (*55*). However, we have

found that the redox potential of the EndoIII cluster shifts upon DNA binding (*56*). The electrochemistry of EndoIII was measured on HOPG electrodes that were either bare or modified with DNA. On DNA-modified HOPG electrodes, the observed midpoint potential of 20 mV versus NHE was assigned to the $[4Fe4S]^{3+/2+}$ couple, similarly to what had been previously reported on DNA-modified gold electrodes. On bare HOPG, two signals were observed: an irreversible anodic peak at 250 mV and a cathodic peak at -300 mV, assigned to the $[4Fe4S]^{3+/2+}$ and $[4Fe4S]^{2+/1+}$ couples, respectively. Thus DNA binding negatively shifts the $[4Fe4S]^{3+/2+}$ redox potential of the cluster by at least 200 mV, activating the cluster towards oxidation (*56*). Because significant conformational changes do not occur upon DNA binding, a thermodynamic consequence of this shift in redox potential is that the oxidized, $[4Fe4S]^{3+}$ form of EndoIII has a much higher affinity for DNA (3 orders of magnitude) than the reduced, $[4Fe4S]^{2+}$ form (*56*). Lower DNA binding affinity for the reduced enzyme was also observed qualitatively with bulk electrolysis experiments on EndoIII, MutY, and UDG (*49*). Therefore while these proteins are relatively insensitive to oxidation in solution, the redox potential of the 4Fe4S cluster shifts into the physiologically relevant range when bound to DNA.

The combination of (*i*) the negative shift in redox potential of the 4Fe4S cluster of glycosylase enzymes upon DNA binding that entails higher binding affinity in the oxidized $[4Fe4S]^{3+}$ state compared to the reduced $[4Fe4S]^{2+}$ state, (*ii*) similar DNA-bound $[4Fe4S]^{3+/2+}$ redox potentials of approximately 80 mV versus NHE for all of the enzymes studied, and (*iii*) the rapid kinetics of DNA CT (ps), suggested a model whereby these proteins could use

interprotein DNA-mediated CT, in a kind of electron transfer self-exchange reaction, to cooperate in order to find lesions inside the cell (*53*) (Figure 4). In this model, a 4Fe4S cluster-containing repair enzyme binding DNA in the reduced form can become oxidized by guanine radicals in the DNA. A second 4Fe4S cluster-containing enzyme can bind within (at a minimum) 100 bases of the first enzyme, becoming activated towards oxidation and releasing an electron into the π-stack of the DNA. This electron can reduce the first distally bound repair enzyme via DNA CT if the intervening DNA is undamaged, resulting in dissociation of this reduced enzyme. Because the DNA-bound redox potentials of the clusters are very similar, this interprotein DNA-mediated CT can be viewed as an activationless self-exchange ET reaction. However, if there is a lesion in the DNA between the proteins, DNA CT will be attenuated and the electron will not reach the distal protein. Instead, both proteins will remain bound to the DNA and can processively diffuse to the location of damage. In this manner, the range over which the slower process of diffusion must occur is significantly reduced. Thus we propose that DNA-mediated signaling would be an efficient way to localize BER proteins to the vicinity of DNA lesions within the cell.

Experiments first focused on gathering *in vitro* evidence for the feasibility of 4Fe4S cluster-protein oxidation by guanine radicals through DNA CT (*57*,*58*). MutY oxidation via the flash-quench technique was monitored by EPR and transient absorption spectroscopies (*57*). With poly(dG-dC) DNA, $[Ru(phen)_2(dppz)]^{2+}$, and diffusing quencher, a mixture of $[4Fe4S]^{3+}$ and its decomposition product, the $[3Fe4S]^{+}$ cluster, is detected upon irradiation in the presence of MutY with low temperature EPR. When poly(dA-dT) is

substituted, a significantly lower intensity EPR signal is observed. With transient absorption and poly(dG-dC) in the absence of protein, a positive transient at 405 nm that decays after approximately 100 μs can be assigned to the guanine radical. Upon the addition of MutY, a very long-lived positive transient is observed at 405 nm that can be fit to obtain coefficients for a fast phase and a slow phase. Absorbance difference spectra plotting coefficients of the fast phase as a function of wavelength correspond to what would be expected for guanine radical, whereas that of the slow phase displayed a maximum at 405 nm, as would be expected for $[4Fe4S]^{3+/2+}$ difference spectra. Therefore this slow phase species can be ascribed to oxidized MutY, likely $[4Fe4S]^{3+}$. The long-lived positive transient is not observed with poly(dA-dT). Furthermore, the yield of guanine oxidation was monitored biochemically in radiolabeled mixed sequence DNA containing a guanine doublet (*57*). In the absence of MutY, damage is localized specifically to the 5′-G of the guanine doublet as expected for oxidative damage generated through DNA CT; this damage is inhibited upon titration of MutY. Overall, these data indicate that while MutY can be oxidized without guanine radical as an intermediate, the thermodynamically favorable oxidation of the MutY $[4Fe4S]^{2+}$ cluster by guanine radical enables more efficient MutY oxidation (*57*). Subsequently, EPR experiments with a nitroxide spin label conjugated to uracil within the DNA sequence demonstrated the feasibility of ET from both EndoIII and MutY to the oxidized spin label (*58*). The EPR-active, $S = ½$ nitroxide species can be oxidized with a mild Ir^{4+} oxidant to yield an EPR-silent species with a reduction potential sufficient to oxidize the $[4Fe4S]^{2+}$ cluster of BER proteins. The reappearance of the nitroxide signal upon the addition of

protein indicates iron-sulfur cluster oxidation to reduce the spin label. A DNA-mediated mechanism is suggested because of the dependence of spin probe reduction on the electronic coupling of the nitroxide spin label: when the spin label is well-coupled to the DNA via an unsaturated linkage, the nitroxide is efficiently reduced, whereas the yield is significantly attenuated with a poorly coupled saturated linkage (*58*).

The iron-sulfur clusters of DNA repair proteins can be oxidized by guanine and modified bases, but could DNA CT be feasible under cellular conditions? In eukaryotic cells, genomic DNA is not freely accessible, but is instead wrapped around histones to form nucleosome core particles. To address the feasibility of DNA CT in nucleosome core particles, Núñez *et al.* investigated oxidative DNA damage induced by covalently tethered $[Rh(phi)_2(bpy')]^{3+}$ in DNA wrapped around histones (*59*). The level of damage to a distal guanine doublet was nearly identical between bare DNA and histone-wrapped DNA, indicating that DNA CT is not attenuated by packaging into nucleosome core particles. Furthermore, there is significant protein traffic on DNA in living cells, including transcription factors and DNA processing enzymes. While DNA CT is attenuated by protein binding events that distort DNA π-stacking by significantly bending the DNA (i.e., TATA binding protein) or flipping out a DNA base, DNA CT is preserved amidst protein traffic that maintains DNA π-stacking (*10,60*). In fact, DNA CT can even be slightly enhanced by protein binding, potentially due to the rigidifying effect of protein binding on base stacking (*60*). Hence DNA CT can occur in nucleosome core particles and is tolerant of most protein traffic, making it feasible *in vivo*.

Subsequent work in the Barton group focused on garnering both *in vitro* and *in vivo* evidence for interprotein signaling via DNA CT. Our model predicts a redistribution of BER proteins from regions of undamaged DNA to the vicinity of a lesion. Using atomic force microscopy (AFM), we have shown that WT EndoIII does indeed redistribute from short well-matched DNA strands onto long strands containing a lesion (*53*). This lesion is a single C:A mismatch which inhibits DNA CT but is not itself a substrate for EndoIII. Redistribution is quantified as a binding density ratio, *r*, of the number of proteins on the long mismatched strands relative to those on short matched strands; a binding density ratio of 1 would indicate equal protein distribution. For WT EndoIII, a binding density ratio of 1.6 ± 0.09 is observed that is even more pronounced in the presence of increasing concentrations of hydrogen peroxide. According to the model, some level of protein oxidation is necessary for redistribution; this is enhanced under conditions that simulate oxidative stress in the cell. Redistribution is also dependent on the proficiency of the protein for DNA CT. Aromatic amino acid residues are known to mediate electron transfer in proteins, accelerating long-distance ET processes that would otherwise be kinetically infeasible (*61*). Y82 in *E. coli* EndoIII is a conserved, aromatic residue in close proximity to the DNA backbone. Mutating this aromatic tyrosine residue to an alanine (Y82A) results in a protein that is electrochemically deficient in DNA CT but proficient in enzymatic glycosylase activity (*53*). Likely because of poorer electronic coupling, less charge can be passed to the iron-sulfur cluster, resulting in a lower signal intensity in cyclic voltammetry experiments. Importantly, Y82A EndoIII is unable to redistribute onto mismatched strands

in the AFM assay because of its inability to perform effective DNA CT. Furthermore Boal *et al.* report an assay measuring the cooperativity of BER proteins *in vivo* (*53*). The "helper function" assay quantifies MutY activity in *E. coli*; thus, a gene of interest can be knocked out to investigate the resultant effects on MutY activity inside living cells. While the details of this assay will not be discussed here, given the strain that is utilized, colonies that are able to grow under specific conditions are "revertants" that result from decreased MutY activity. When the gene for EndoIII is knocked out, MutY activity is decreased even though MutY and EndoIII target different lesions within the cell, indicating that EndoIII contributes to MutY activity by some other mechanism. DNA-mediated signaling between EndoIII and MutY to assist the very low copy number MutY to localize to the vicinity of lesions is suggested by experiments with EndoIII mutants. Restoring CT-deficient Y82A EndoIII does not rescue MutY activity. Conversely, D138A EndoIII, while deficient in glycosylase activity, retains an intact 4Fe4S cluster, and is able to rescue MutY activity. Consequently, the important factor for EndoIII rescuing MutY activity is proficiency for DNA CT. Overall, this helper function assay was the first demonstration of interprotein DNA CT within cells.

Other DNA repair proteins outside the BER pathway have been found with similar DNA-bound $[4Fe4S]^{3+/2+}$ redox potentials. XPD is an ATP-dependent nucleotide excision repair (NER) helicase with a 4Fe4S cluster. On DNA-modified electrode, archaeal XPD from the thermophile *Sulfolobus acidocaldarius* (SaXPD), which shares approximately 22% sequence identity with the human homolog, was found to have a DNA-bound potential of

80 mV versus NHE that is sensitive to an intervening mismatch (*62*). Interestingly, an increase in the electrochemical signal intensity is observed upon the addition of ATP to SaXPD on the DNA-modified electrode surface, but is not observed in the presence of the slowly hydrolyzable analog ATP-γ-S. An ATPase and helicase deficient mutant, G34R XPD, also does not display this increase in current. The signal increase upon ATP addition was ascribed to conformational changes associated with ATP hydrolysis, demonstrating that DNA-mediated electrochemistry can report on enzymatic activity (*62*).

AFM studies combining EndoIII and XPD give direct *in vitro* evidence for interprotein DNA-mediated signaling (*63*). Initial AFM studies showed that WT XPD redistributes from short matched DNA strands to long mismatched strands with a binding density ratio (r = 1.54 ± 0.08) similar to that of WT EndoIII. In contrast, L325V XPD, an electrochemically CT-deficient XPD mutant, does not redistribute analogously to Y82A EndoIII. Equimolar mixtures of XPD and EndoIII were then assayed at concentrations where approximately 2 proteins are bound per DNA strand. Remarkably, mixtures of the *E. coli* BER protein EndoIII and archaeal NER protein XPD efficiently redistribute, localizing to the vicinity of a DNA lesion (*63*). However, this redistribution is not observed if either protein in the mixture is CT-deficient (i.e., WT XPD with Y82A EndoIII, WT EndoIII with L325V XPD, or WT XPD with L325V XPD), likely because at these protein loadings of approximately 2 proteins per strand, a CT-deficient protein results in no partner for the electron self-exchange reaction. When WT XPD is titrated into Y82A EndoIII at a ratio of 3:1, efficient redistribution is recovered because there is a significant population of partners

of CT-proficient proteins. Therefore, given similar DNA-bound redox potentials of their $[4Fe4S]^{3+/2+}$ clusters, proteins from different repair pathways, and even different organisms, can use DNA-mediated CT to cooperate in order to find lesions.

DinG is an *E. coli* DNA damage-inducible helicase with a 4Fe4S cluster and homology to XPD as well as other eukaryotic helicases. DinG performs the vital function of unwinding RNA-DNA hybrid structures, called R-loops, which result from stalled replication forks (*64*). When investigated on DNA-modified electrodes, DinG displays a DNA-bound redox potential of 80 mV versus NHE, the same DNA-bound $[4Fe4S]^{3+/2+}$ potential that had been observed for the BER proteins and SaXPD (*49*,*62*). Like the fellow ATP-dependent helicase XPD, the intensity of the DinG electrochemical signal increases upon the ATP addition. Utilization of the AFM assay demonstrated *in vitro* redistribution with WT DinG only as well as with equimolar mixtures of WT DinG and EndoIII proteins; conversely, redistribution does not occur in a 1:1 mixture of WT DinG with Y82A EndoIII. A modest decrease in MutY activity *in vivo* upon knocking out DinG is observed in the "helper function" assay. This effect can be rescued by complementing with D138A EndoIII but not Y82A EndoIII, suggesting DNA-mediated cross-talk between MutY, DinG, and EndoIII inside cells (*64*).

A much more dramatic *in vivo* result was found with the InvA strain of *E. coli*. By inverting the highly transcribed ribosomal RNA operon, this strain contains an increased frequency of collisions between the transcriptional and replication machinery, forming stalled replication forks (*65*). The resulting RNA-DNA hybrid structures must be unwound

by DinG to maintain cellular viability. Signaling between DinG and EndoIII was investigated *in vivo* by knocking out the gene for EndoIII within the InvA *E. coli* strain. Bacterial growth is severely impaired in this InvA EndoIII knockout strain. An R-loop phenotype was implicated by rescue with RNaseH, as this enzyme selectively degrades RNA in RNA-DNA hybrids. Bacterial growth could also be restored by complementation with WT or D138A EndoIII on a plasmid, but not Y82A EndoIII, implying a DNA CT mechanism (*64*). This is compelling *in vivo* evidence for DNA CT between DinG and EndoIII to assist DinG in maintaining cellular viability under the adverse conditions caused by increased collisions between the transcriptional and replication machinery.

Currently, the number of DNA processing enzymes that contain 4Fe4S clusters continues to increase. For example, in addition to glycosylase and helicase enzymes, 4Fe4S clusters have been found in RNA polymerase (*66*), all four yeast B-family DNA polymerases (*67*), as well as in primase (*68*). As more potential electron self-exchange partners are discovered, DNA-mediated signaling becomes an increasingly viable mechanism to coordinate diverse cellular processes.

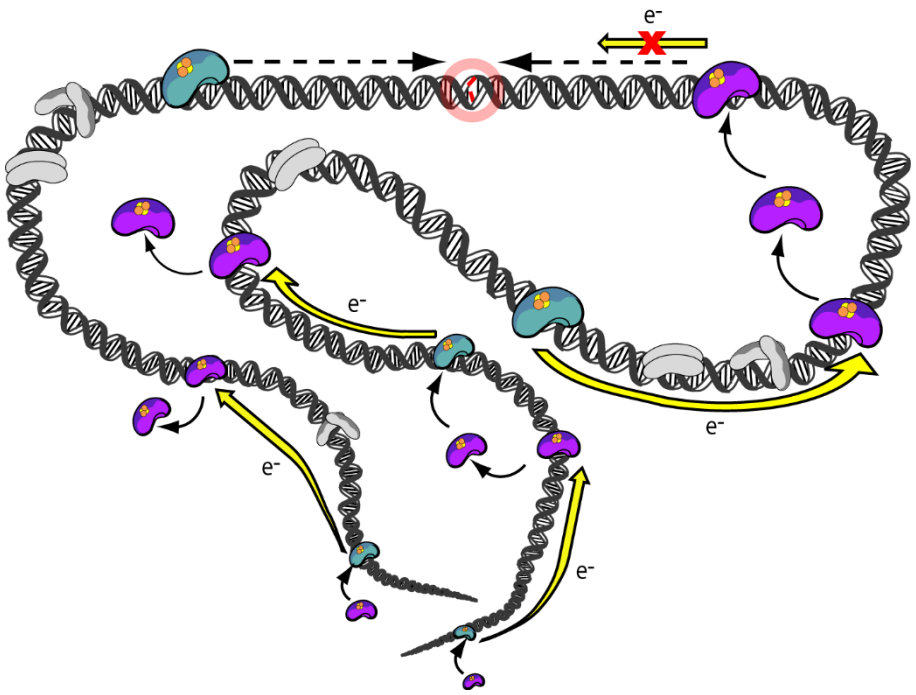

Figure 4. Model whereby 4Fe4S cluster-containing DNA processing enzymes proteins could use interprotein DNA charge transport to cooperate in order to efficiently find lesions inside the cell. This DNA-mediated electron transfer self-exchange reaction depends on similar DNA-bound $[4Fe4S]^{3+/2+}$ reduction potentials and a lower DNA affinity in the reduced, $[4Fe4S]^{2+}$, state compared to the oxidized $[4Fe4S]^{3+}$ state. When the DNA intervening between the two 4Fe4S cluster-containing proteins (shown in purple and teal) is undamaged, the self-exchange reaction can proceed efficiently, with the result that one of the DNA-bound proteins is reduced and its affinity for DNA lowered. This reduced protein can then diffuse to another region of the genome. However, in the case of an intervening mismatch or lesion that disrupts π-stacking and attenuates DNA CT, this self-exchange reaction is inhibited. Both proteins will remain bound to the DNA in the vicinity of the lesion, significantly reducing the range over which the slower process of diffusion must occur. This search process is not interrupted by protein traffic (gray) that does not disrupt DNA π-stacking. Taken from reference 4.

1.3.2 Long-range activation of redox-active transcription factors via DNA CT

DNA charge transport may also be used biologically for the long-range and selective activation of redox-active transcription factors (Figure 5). SoxR is a homodimeric bacterial transcription factor that responds to superoxide stress, containing a $[2Fe2]^{2+/+}$ cluster within each monomer (*69*). In *E. coli*, oxidation of the 2Fe2S cluster of SoxR causes a conformational change which improves an RNA polymerase binding site, stimulating transcription of SoxS, a secondary transcription factor, which in turn induces the transcription of about 100 genes to combat superoxide stress (*70*). Controversy remains regarding the direct oxidant of SoxR *in vivo*. While *in vitro* experiments support direct oxidation of the 2Fe2S cluster by superoxide (*71*), *in vivo* experiments observe weak induction by superoxide and instead suggest SoxR oxidation by redox cycling drugs (*72*) or the modulation of cellular NADPH content (*73*).

Adding to the confusion, the redox potential $[2Fe2]^{2+/+}$ in solution (-290 mV versus NHE) is such that SoxR could be oxidized by many cellular oxidants, even in the absence of oxidative stress. We have found that DNA binding shifts the redox potential of the 2Fe2S cluster of SoxR (*74*). The positive shift in potential by 0.5 V to 200 mV versus NHE upon DNA binding means that DNA-bound SoxR is primarily in its transcriptionally inactive, reduced form *in vivo*. Work by Paul Lee *et al.* then established the viability of SoxR transcriptional activation through long-range DNA-mediated oxidation (*75*). First, it was demonstrated that reduced SoxR with remaining dithionite, but not oxidized SoxR or dithionite alone, inhibits oxidative damage to a guanine doublet that had been generated via

the flash-quench technique. Moreover, SoxR can be activated *in vivo* using the photooxidant $[Rh(phi)_2bpy]^{3+}$, which specifically induces DNA damage rather than general production of reactive oxygen species such as would be expected by redox-cycling drugs. *E. coli* cells were treated with $[Rh(phi)_2bpy]^{3+}$, irradiated, and the resulting level of *soxS* mRNA transcript quantified by reverse transcription PCR (RT-PCR) (*75*). Under these conditions, but not in a dark control that contained Rh but was not irradiated, or a light control that was irradiated but lacked Rh, the *soxS* transcript is significantly induced, indicating the feasibility of SoxR activation by DNA oxidation in cells. Finally, an abortive transcription assay was used to directly observe transcriptional activation from a distance through DNA-mediated oxidation of SoxR. Here, $[Rh(phi)_2(bpy')]^{3+}$ was tethered to the 5′ end of the DNA, 80 base-pairs from the SoxR binding site. The DNA sequence also contained the promoter binding regions of *soxS*, where upon SoxR oxidation, RNA polymerase will bind and initiate *soxS* transcription. Starting with reduced, transcriptionally inactive SoxR, samples were irradiated, and then incubated with RNA polymerase and ribonucleotides. Remarkably, a 4-mer radiolabeled mRNA corresponding to *soxS* could be detected at significant levels. This activation was triggered simply by irradiation that results in DNA oxidation; furthermore, long-distance electron transfer is ensured by the physical separation of the photooxidant and SoxR. These results suggested a model for transcriptional activation of SoxR: reactive oxygen species can abstract electrons from DNA; electron holes thus produced will localize to low potential sites within the DNA, i.e., guanine multiplets; SoxR can then become rapidly oxidized via DNA CT, filling the guanine radical hole and thus becoming

transcriptionally active (*75*). Transcriptional activation from a distance via DNA CT could be a unifying mechanism for SoxR stimulation *in vivo*.

p53 is a tetrameric transcription factor that has vital roles as a tumor suppressor in humans (*76*). p53 decides cellular fates by selective binding to different promoter sites within the genome, for instance, favoring DNA repair and survival or, instead, apoptotic cell death. While p53 does not contain a 4Fe4S cluster, there is a network of redox-active cysteine residues whose oxidation state modulates p53 DNA binding. Specifically, p53 oxidation promotes dissociation from the DNA. Given the close proximity of some of these redox-active cysteine residues to the DNA (*77*) and the demonstrated feasibility of disulfide bond formation from a distance via DNA CT (*78*), Augustyn *et al.* investigated whether p53 could be oxidized in a DNA-mediated fashion (*79*). In constructs with the photooxidant anthraquinone tethered to the DNA distally from the p53 consensus sequence, irradiation induced p53 dissociation in an artificial consensus sequence as measured in gel-shift assays. However, this p53 dissociation was not observed with an intervening C:A mismatch, implying a DNA-mediated process. Intriguingly, in natural p53 consensus sequences, this p53 oxidation via DNA CT is sequence-specific. Promoter sequences for the p21 gene, encoding a protein involved in cell cycle arrest, and that for Gadd45, encoding a protein more involved in DNA repair, were compared using anthraquinone constructs. Dissociation of p53 from the Gadd45 consensus sequence was observed upon irradiation, which would serve to downregulate the gene inside cells, while little dissociation was observed from the p21 sequence (*79*). Under overwhelming conditions of oxidative stress within the cell, genes

encoding proteins stimulating DNA repair, such as Gadd45, would be downregulated in favor of those promoting cell cycle arrest and apoptotic pathways, such as p21. The sequence-specific DNA-mediated oxidation and dissociation of p53 provides a mechanism for how this could occur selectively. Finally, preliminary mass spectrometry studies suggested chemical evidence for p53 oxidation.

Further work by Schaefer and Barton elucidated the important factors for the sequence selectivity of p53 dissociation (*80*). Again using anthraquinone constructs, artificial p53 consensus sequences were created where the guanine content of a purine region within the consensus sequence was successively increased, essentially titrating the oxidation potential. Upon irradiation, a consensus sequence containing AAA displayed the lowest level of p53 dissociation, while a sequence with GGG showed the highest level of dissociation. Natural consensus sequences with similar guanine content behaved in the same way: S100A2 with GGG in its consensus sequence dissociated more upon irradiation than the caspase sequence with AGA. Thus p53 is preferentially dissociated when low potential guanine multiplets are located within the consensus sequence. The relative importance of particular cysteine residues in the DNA-mediated oxidation of p53 was subsequently investigated by serine mutagenesis (*81*). The ability to dissociate from the Gadd45 promoter upon DNA-mediated oxidation was assayed for six cysteine to serine p53 mutants. The C275S and C277S mutations, located nearby the DNA interface, most significantly impaired protein dissociation. Mass spectrometry experiments utilized differential thiol labeling with iodoacetamide to directly observe cysteine oxidation. After irradiation of WT and mutant

p53 with anthraquinone constructs, reduced cysteines are labeled with standard iodoacetamide, while cysteines that were participating in a disulfide bond are labeled with isotopically heavy $^{13}C_2D_2$-iodoacetamide. In the WT protein, there is clearly a shift towards isotopically heaving iodoacetamide labeling in the irradiated anthraquinone samples. Because this is a direct indictor of more disulfide bond formation, this experiment definitively shows p53 oxidation via DNA CT (*81*). The WT protein shows an increase in oxidation upon irradiation for all of the observable cysteine residues: C124, C135, C141, C182, C275, and C277. However, the C275S mutant shows a significantly smaller increase in oxidation upon irradiation. Thus, after an electron hole localizes to low potential guanine sites within the p53 consensus sequence, C275 and nearby C277, close to the DNA interface, seem to form an initial disulfide bond that inhibits DNA binding. Disulfide bond exchange could then occur with nearby cysteines in the protein. Overall, the important molecular mechanisms for DNA-mediated oxidation of p53 have been revealed; this is a compelling way for p53 to selectively dissociate from different consensus sequences within the cell.

As evidenced with p53, proteins that contain redox-active cofactors other than iron-sulfur clusters can yet participate in DNA-mediated processes. Of particular interest is the bacterial ferritin Dps, which protects DNA from oxidative stress and is implicated in bacterial survival and virulence (*82*). Some of these Dps proteins non-specifically bind DNA; could there be a DNA-mediated component to their protection?

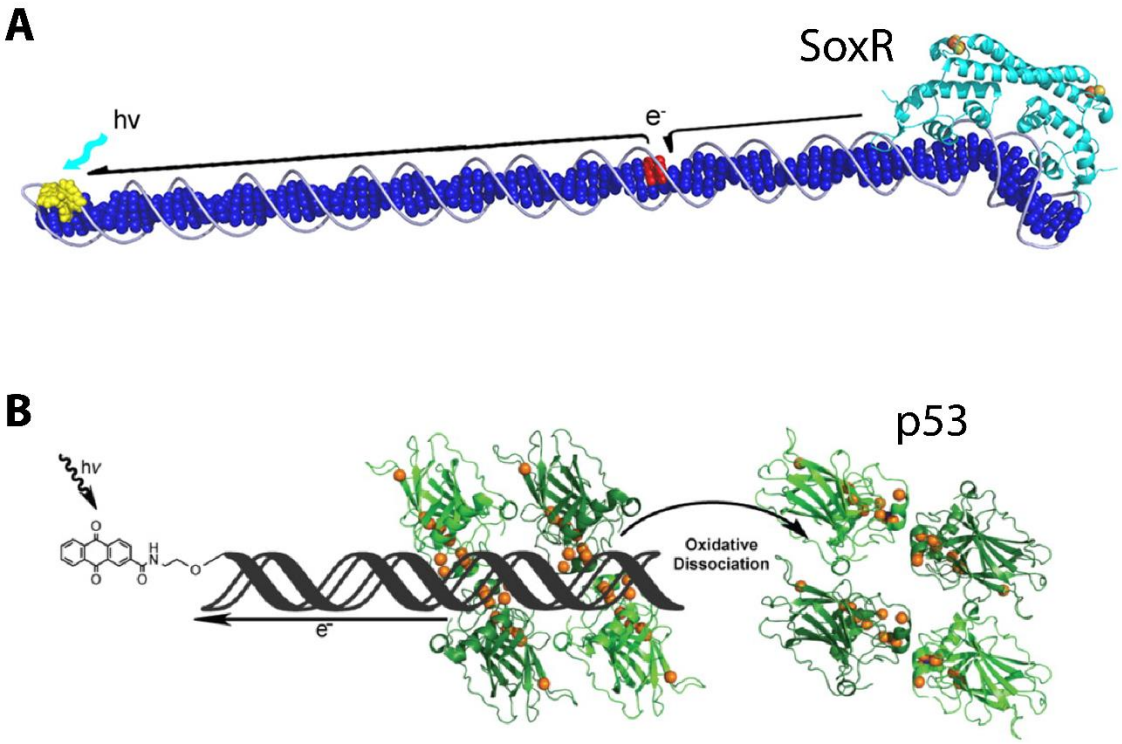

Figure 5. Long-range and selective activation of redox-active transcription factors via DNA charge transport. (*A*) Oxidation and transcriptional activation of the 2Fe2S-cluster containing SoxR, a bacterial superoxide response transcription factor, via long-distance DNA CT to fill guanine radical holes (red). (*B*) Sequence selective oxidation and dissociation of the tumor suppressor p53, which contains a network of redox-active cysteine residues (gold spheres) via DNA CT as a mechanism to decide cellular fates by selective binding to different promoter sites within the genome. Taken from references 75 (copyright © National Academy of Sciences) and 81, respectively.

1.4 Conclusions

DNA charge transport involves the efficient transport of electrons or electron holes through the DNA π-stack over long molecular distances of at least 100 base-pairs. Despite this shallow distance dependence, DNA CT is sensitive to mismatches or lesions that disrupt π stacking and is critically dependent on proper electronic coupling of the donor and acceptor moieties into the base stack. Favorable DNA CT is very rapid, occurring on the picosecond timescale. Because of this speed, electron holes equilibrate along the DNA π-stack, forming a characteristic pattern of DNA damage to low potential guanine multiplets. Furthermore, DNA CT may be used in a biological context. DNA processing enzymes with 4Fe4S clusters can perform DNA-mediated ET self-exchange reactions with other 4Fe4S cluster proteins, even if the proteins are quite dissimilar, as long as the DNA-bound $[4Fe4S]^{3+/2+}$ redox potentials are conserved. For instance, this mechanism would allow low copy number DNA repair proteins to efficiently find their lesions within the cell. DNA CT may also be used biologically for the long-range, selective activation of redox-active transcription factors. The search continues for more proteins that may utilize DNA CT within the cell.

References

1. Lodish, H.; Berk, A.; Zipursky, S.L.; Matsudaira, P.; Baltimore, D.; Darnell, J. *Molecular Cell Biology*, 4th Edition; W. H. Freeman: New York, 2000.

2. Saito, Y.; Yoshikawa, T.; Bandow, S.; Tomita, M.; Hayashi, T. Interlayer spacings in carbon nanotubes. *Phys. Rev. B.* **1993**, *48*, 1907-1909.

3. Chaban, Y.; Boekema E.J.; Dudkina, N.V. Structures of mitochondrial oxidative phosphorylation supercomplexes and mechanisms for their stabilisation. *Biochim. Biophys. Acta* **2014**, *1837*, 418-426.

4. Grodick, M.A.; Muren, N.B.; Barton, J.K. DNA charge transport within the cell. *Biochemistry* **2015**, *54*, 962-973.

5. Elias, B.; Shao, F.; Barton, J.K. Charge migration along the DNA duplex: Hole versus electron transport. *J. Am. Chem. Soc.* **2008**, *130*, 1152-1153.

6. Kelley, S.O.; Holmlin, R.E.; Stemp, E.D.A.; Barton, J.K. Photoinduced electron transfer in ethidium-modified DNA duplexes: Dependence on distance and base stacking. J. Am. Chem. Soc. **1997**, *119*, 9861-9870.

7. Kelley, S.O.; Boon, E.M.; Barton, J.K.; Jackson, N.M; Hill, M.G. Single-base mismatch detection based on charge transduction through DNA. *Nucleic Acids Res.* **1999**, *27*, 4830-4837.

8. Boal, A.K.; Barton, J.K. Electrochemical detection of lesions in DNA. *Bioconjugate Chem.* **2005**, *16*, 312-321.

9. Hall, D.B.; Barton, J.K. Sensitivity of DNA-mediated electron transfer to the intervening π-stack: A probe for the integrity of the DNA base stack. *J. Am. Chem. Soc.* **1997**, *119*, 5045-5046.

10. Gorodetsky, A.A.; Ebrahim, A.; Barton, J.K. Electrical detection of TATA binding protein at DNA-modified microelectrodes. *J. Am. Chem. Soc.* **2008**, *130*, 2924-2925.

11. Liu, T.; Barton, J.K. DNA electrochemistry through the base pairs not the sugar-phosphate backbone. *J. Am. Chem. Soc.* **2005**, *127*, 10160-10161.

12. Li, S.; Cooper, V.R.; Thonhauser, T.; Lundqvist, B.I.; Langreth, D.C. Stacking interactions and DNA intercalation. *J. Phys. Chem. B* **2009**, *113*, 11166-11172.

13. Williams, T.T.; Dohno, C.; Stemp, E.D.A.; Barton, J.K. Effects of the photooxidant on DNA-mediated charge transport. *J. Am. Chem. Soc.* **2004**, *126*, 8148-8158.

14. Shao, F.; Barton, J.K. Long-range electron and hole transport through DNA with tethered cyclometalated Iridium(III) complexes. *J. Am. Chem. Soc.* **2007**, *129*, 14733-14738.

15. Olmon, E.D.O.; Hill, M.G.; Barton, J.K. Using metal complex reduced states to monitor the oxidation of DNA. *Inorg. Chem.* **2011**, *50*, 12034-12044.

16. Holmlin, R.E.; Dandliker, P.J.; Barton, J.K. Synthesis of metallointercalator-DNA conjugates on a solid support. *Bioconjugate Chem.* **1999**, *10*, 1122-1130.

17. Murphy, C.J.; Arkin, M.R.; Jenkins, Y.; Ghatlia, N.D.; Bossmann, S.; Turro, N.J.; Barton, J.K. Long range photoinduced electron transfer through a DNA helix. *Science* **1993**, *262*, 1025-129.

18. Friedman, A.E.; Chambron, J.-C.; Sauvage, J.-P.; Turro, N.J.; Barton, J.K. Molecular "light switch" for DNA $Ru(bpy)_2(dppz)^{2+}$. *J. Am. Chem. Soc.* **1990**, *112*, 4960-4962.

19. Arkin, M.R.; Stemp, E.D.A.; Holmlin, R.E.; Barton, J.K.; Hörmann, A.; Olson, E.J.C.; Barbara, P.F. Rates of DNA-mediated electron transfer between metallointercalators. *Science* **1996**, *273*, 475-480.

20. Wan, C.; Fiebig, T.; Kelley, S.O.; Treadway, C.R.; Barton, J.K.; Zewail, A.H. Femtosecond dynamics of DNA-mediated electron transfer. *Proc. Natl. Acad. Sci. USA* **1999**, *96*, 6014-6019.

21. Genereux, J.C.; Barton, J.K. Mechanisms for DNA charge transport. *Chem. Rev.* **2010**, *110*, 1642-1662.

22. O'Neill, M.A.; Becker, H.-C.; Wan, C.; Barton, J.K.; Zewail, A.H. Ultrafast dynamics in DNA-mediated electron transfer: base gating and the role of temperature. *Angew. Chem. Int. Ed.* **2003**, *42*, 5896-5900.

23. O'Neill, M.A.; Barton, J.K. DNA charge transport: Conformationally gated hopping through stacked domains. *J. Am. Chem. Soc.* **2004**, *126*, 11471-11483.

24. Genereux, J.C.; Augustyn, K.E.; Davis, M.L.; Shao, F.; Barton, J.K. Back-electron transfer suppresses the periodic length dependence of DNA-mediated charge transport across adenine tracts. *J. Am. Chem. Soc.* **2008**, *130*, 15150-15156.

25. Xiang, L.; Palma, J.L.; Bruot, C.; Mujica, V.; Ratner, M.A.; Tao, N. Intermediate tunnelling–hopping regime in DNA charge transport. *Nat. Chem.* **2015**, *7*, 221-226.

26. Fukuzumi, S.; Miyao, H.; Ohkubo, K.; Suenobu, T. Electron-transfer oxidation properties of DNA bases and DNA oligomers. *J. Phys. Chem. A* **2005**, *109*, 3285-3294.

27. Sugiyama, H.; Saito, I. Theoretical studies of GG-specific photocleavage of DNA via electron transfer: Significant lowering of ionization potential and 5′-localization of HOMO of stacked GG bases in B-Form DNA. *J. Am. Chem. Soc.* **1996**, *118*, 7063-7068.

28. Saito, I.; Nakamura, T.; Nakatani, K.; Yoshioka, Y.; Yamaguchi, K.; Sugiyama, H. Mapping of the hot spots for DNA damage by one-electron oxidation: Efficacy of GG doublets and GGG triplets as a trap in long-range hole migration. *J. Am. Chem. Soc.* **1998**, *120*, 12686-12687.

29. Burrows, C. J.; Muller, J. G. Oxidative nucleobase modifications leading to strand scission *Chem. Rev.* **1998**, *98*, 1109-1151.

30. Hall, D.B.; Holmlin, R.E.; Barton, J.K. Oxidative DNA damage through long-range electron transfer. *Nature* **1996**, *382*, 731-735.

31. Arkin, M.R.; Stemp, E.D.A.; Pulver, S.C.; Barton, J.K. Long-range oxidation of guanine by Ru(III) in duplex DNA. *Chem. Biol.* **1997**, *4*, 389-400.

32. Stemp, E.D.A.; Arkin, M.R.; Barton, J.K. Oxidation of guanine in DNA by $Ru(phen)_2(dppz)^{3+}$ using the flash-quench technique. *J. Am. Chem. Soc.* **1997**, *119*, 2921-2925.

33. Delaney, S.; Pascaly, M.; Bhattacharya, P. K.; Han, K.; Barton, J.K. Oxidative damage by ruthenium complexes containing the dipyridophenazine ligand or its derivatives: A focus on intercalation. *Inorg. Chem.* **2002**, *41*, 1966-1974.

34. Schiemann, O.; Turro, N.J.; Barton, J.K. EPR detection of guanine radicals in a DNA duplex under biological conditions: Selective base oxidation by $Ru(phen)_2dppz^{3+}$ using the flash-quench technique. *J. Phys. Chem. B* **2000**, *104*, 7214-7220.

35. Kelley, S.O.; Barton, J.K.; Jackson, N.M.; Hill, M.G. Electrochemistry of methylene blue bound to a DNA-modified electrode. *Bioconjugate Chem.* **1997**, *8*, 31-37.

36. Pheeney, C.G.; Barton, J.K. DNA electrochemistry with tethered methylene blue. *Langmuir* **2012**, *28*, 7063-7070.

37. Furst, A.L.; Hill, M.G.; Barton, J.K. DNA-modified electrodes fabricated using copper-free click chemistry for enhanced protein detection. *Langmuir*, **2013**, *29*, 16141-16149.

38. Gorodetsky, A.A.; Barton, J.K. Electrochemistry using self-assembled DNA monolayers on highly oriented pyrolytic graphite. *Langmuir* **2006**, *22*, 7917-7922.

39. Boon, E.M.; Jackson, N.M.; Wightman, M.D.; Kelley, S.O.; Hill, M.G.; Barton, J.K. Intercalative stacking: A critical feature of DNA charge-transport electrochemistry. *J. Phys. Chem. B* **2003**, *107*, 11805-11812.

40. Gorodetsky, A.A.; Green, O.; Yavin, E.; Barton, J.K. Coupling into the base pair stack is necessary for DNA-mediated electrochemistry. *Bioconjugate Chem.* **2007**, *18*, 1434-1441.

41. Slinker, J.D.; Muren, N.B.; Renfrew, S.E.; Barton, J.K. DNA charge transport over 34 nm. *Nat. Chem.* **2011**, *3*, 228-233.

42. Boon, E.M.; Livingston, A.L.; Chmiel, N.H.; David, S.S.; Barton, J.K. DNA-mediated charge transport for DNA repair. *Proc. Nat. Acad. Sci. USA* **2003**, *100*, 12543-12547.

43. Slinker, J.D.; Muren, N.B.; Gorodetsky, A.A.; Barton, J.K. Multiplexed DNA-modified electrodes. *J. Am. Chem. Soc.*, **2010**, *132*, 2769-2774.

44. Drummond, T. G.; Hill, M.G.; Barton, J.K. Electron transfer rates in DNA films as a function of tether length. *J. Am. Chem. Soc.* **2004**, *126*, 15010-15011.

45. Gray, H.B.; Winkler, J.R. Electron flow through proteins. *Chem Phys Lett.* **2009**, *483*, 1-9.

46. Wagenknecht, H.-A.; Stemp, E.D.A.; Barton, J.K. Evidence of electron transfer from peptides to DNA: Oxidation of DNA-bound tryptophan using the flash-quench technique. *J. Am. Chem. Soc.* **2000**, *122*, 1-7.

47. Wagenknecht, H.-A.; Stemp, E.D.A.; Barton, J.K. DNA-bound peptide radicals generated through DNA-mediated electron transport. *Biochemistry* **2000**, *39*, 5483-5491.

48. Wagenknecht, H.-A.; Rajski, S.R.; Pascaly, M.; Stemp, E.D.A.; Barton, J.K. Direct observation of radical intermediates in protein-dependent DNA charge transport. *J. Am. Chem. Soc.* **2001**, *123*, 4400-4407.

49. Boal, A.K.; Yavin, E.; Lukianova, O.A.; O'Shea, V.L.; David, S.S.; Barton, J.K. DNA-bound redox activity of DNA repair glycosylases containing [4Fe-4S] clusters. *Biochemistry* **2005**, *44*, 8397-8407.

50. Kim, Y.J.; Wilson, D.M. 3rd. Overview of base excision repair biochemistry. *Curr. Mol. Pharmacol.* **2012**, *5*, 3-13.

51. David, S.S.; O'Shea, V.L.; Kundu, S. Base-excision repair of oxidative DNA damage. *Nature*, **2007**, *447*, 941-950.

52. Demple, B.; Harrison, L. Repair of oxidative damage to DNA: Enzymology and biology. *Annu Rev Biochem.* **1994**, *63*, 915-948.

53. Boal, A.K.; Genereux, J.C.; Sontz, P.A.; Gralnick, J.A.; Newman, D.K.; Barton, J.K. Redox signaling between DNA repair proteins for efficient lesion detection *Proc. Natl. Acad. Sci. USA* **2009**, *106*, 15237-15242.

54. Cunningham, R.P., Asahara, H., Bank, J.F., Scholes, C.P., Salerno, J.C., Surerus, K., Münck, E., McCracken, J., Peisach, J., and Emptage, M.H. Endonuclease III is an iron-sulfur protein. *Biochemistry* **1989**, *28*, 4450-4455.

55. Porello, S.L.; Cannon, M.J.; David, S.S. A substrate recognition role for the $[4Fe\text{-}4S]^{2+}$ cluster of the DNA repair glycosylase MutY. *Biochemistry* **1998**, *37*, 6465-6475.

56. Gorodetsky, A.A.; Boal, A.K.; Barton, J.K. Direct electrochemistry of Endonuclease III in the presence and absence of DNA *J. Am. Chem. Soc.* **2006**, *128*, 12082-12083.

57. Yavin, E.; Boal, A.K.; Stemp, E.D.A.; Boon, E.M.; Livingston, A.L.; O'Shea, V.L.; David, S.S.; Barton, J.K. Protein-DNA charge transport: Redox activation of a DNA repair protein by guanine radical. *Proc. Nat. Acad. Sci. USA* **2005**, *102*, 3546-3551.

58. Yavin, E.; Stemp, E.D.A.; O'Shea, V.L.; David, S.S.; Barton, J.K. Electron trap for DNA-bound repair enzymes: A strategy for DNA-mediated signaling. *Proc. Nat. Acad. Sci. USA* **2006**, *103*, 3610-3614.

59. Núñez, M.E.; Noyes, K.T.; Barton, J.K. Oxidative charge transport through DNA in nucleosome core particles. *Chem. Biol.* **2002**, *9*, 403-415.

60. Rajski, S.R.; Barton, J.K. How different DNA-binding proteins affect long-range oxidative damage to DNA. *Biochemistry* **2001**, *40*, 5556-5564.

61. Shih, C.; Museth, A.K.; Abrahamsson, M.; Blanco-Rodriguez, A.M.; Di Bilio, A.J.; Sudhamsu, J.; Crane, B.R.; Ronayne, K.L.; Towrie, M.; Vlček, A. Jr.; Richards, J.H.; Winkler, J.R.; Gray, H.B. Tryptophan-accelerated electron flow through proteins. *Science* **2008**, *320*, 1760-1762.

62. Mui, T.P.; Fuss, J.O.; Ishida, J.P.; Tainer, J.A.; Barton, J.K. ATP-stimulated, DNA-mediated redox signaling by XPD, a DNA repair and transcription helicase. *J. Am. Chem. Soc.* **2011**, *133*, 16378-16381.

63. Sontz, P.A.; Mui, T.P.; Fuss, J.O.; Tainer, J.A.; Barton, J.K. DNA charge transport as a first step in coordinating the detection of lesions by repair proteins. *Proc. Natl. Acad. Sci. USA* **2012***, 109*, 1856-1861.

64. Grodick, M.A.; Segal, H.M.; Zwang, T.J.; Barton, J.K. DNA-mediated signaling by proteins with 4Fe-4S clusters is necessary for genomic integrity. *J. Am. Chem. Soc.* **2014**, *136*, 6470-6478.

65. Boubakri, H.; de Septenville, A.L.; Viguera, E.; Michel, B. The helicases DinG, Rep and UvrD cooperate to promote replication across transcription units *in vivo*. *EMBO J.* **2010**, *29*, 145-157.

66. Hirata, A.; Klein, B.J.; Murakami, K.S. The X-ray crystal structure of RNA polymerase from Archaea. *Nature* **2008**, *451*, 851-854.

67. Netz, D.J.A.; Stith, C.M.; Stümpfeg, M.; Köpf, G.; Vogel, D.; Genau, H.M.; Stodoloa, J.L.; Lill, R.; Burgers, P.M.J.; Pierik, A.J. Eukaryotic DNA polymerases require an iron-sulfur cluster for the formation of active complexes. *Nat. Chem. Biol.* **2011**, *8*, 125-132.

68. Weiner, B.E.; Huang, H.; Dattilo, B.M.; Milges, M.J.; Fanning, E.; Chazin, W.J. An iron-sulfur cluster in the C-terminal domain of the p58 subunit of human DNA primase. *J. Biol. Chem*. **2007**, *46*, 33444–33451.

69. Watanabe, S.; Kita, A.; Kobayashi, K.; Miki, K. Crystal structure of the [2Fe-2S] oxidative-stress sensor SoxR bound to DNA. *Proc. Natl. Acad. Sci. USA* **2008**, *105*, 4121-4126.

70. Imlay, J.A. Cellular defenses against superoxide and hydrogen peroxide. *Annu. Rev. Biochem.* **2008**, 77, 755-776.

71. Fujikawa, M.; Kobayashi, K.; Kozawa, T. Direct oxidation of the [2Fe-2S] cluster in SoxR protein by superoxide. *J. Biol. Chem*. **2012**, *287*, 35702-35708.

72. Gu, M.; Imlay, J.A. The SoxRS response of *Escherichia coli* is directly activated by redox-cycling drugs rather than by superoxide. *Mol. Microbiol.* **2011**, *79*, 1136-1150.

73. Krapp, A.R.; Humbert, M.V.; Carrillo, N. The soxRS response of *Escherichia coli* can be

induced in the absence of oxidative stress and oxygen by modulation of NADPH content. *Microbiology* **2011**, *157*, 957-965.

74. Gorodetsky, A.A.; Dietrich, L.E.P.; Lee, P.E.; Demple, B.; Newman, D.K.; Barton, J.K. DNA binding shifts the redox potential of the transcription factor SoxR. *Proc. Natl. Acad. Sci. USA* **2008**, *105*, 3684-3689.

75. Lee, P.E.; Demple, B.; Barton, J.K. DNA-mediated redox signaling for transcriptional activation of SoxR. *Proc. Natl. Acad. Sci. USA* **2009**, *106*, 13164-13168.

76. Vousden, K.H.; Lu, X. Live or let die: the cell's response to p53. *Nat. Rev. Cancer* **2002**, *2*, 594-604.

77. Cho, Y.; Gorina, S.; Jeffrey, P.D.; Pavletich, N.P. Crystal structure of a p53 tumor suppressor-DNA complex: understanding tumorigenic mutations. *Science* **1994**, *265*, 346-355.

78. Takada T.; Barton, J.K. DNA charge transport leading to disulfide bond formation. *J. Am. Chem. Soc.* **2005**, *127*, 12204-12205.

79. Augustyn, K.E.; Merino, E.J.; Barton, J.K. A role for DNA-mediated charge transport in regulating p53: Oxidation of the DNA-bound protein from a distance. *Proc. Natl. Acad. Sci. USA* **2007**, *104*, 18907-18912.

80. Schaefer, K.N.; Barton, J.K. DNA-mediated oxidation of p53. *Biochemistry* **2014**, *53*, 3467-3475.

81. Schaefer, K.N.; Geil, W.M.; Sweredoski, M.J.; Moradian, A.; Hess, S.; Barton, J.K. Oxidation of p53 through DNA charge transport involves a network of disulfides within the DNA-binding domain. *Biochemistry* **2015**, 54, 932-941.

82. Chiancone, E.; Ceci, P. The multifaceted capacity of Dps proteins to combat bacterial stress conditions: Detoxification of iron and hydrogen peroxide and DNA binding. *Biochim. Biophys. Acta* **2010**, *1800*, 798-805.

Chapter 2

DNA Protection by the Bacterial Ferritin Dps via DNA Charge Transport*

*Adapted from Arnold, A.R. and Barton, J.K. *J. Am. Chem. Soc.* **2013**, *135*, 15726-15729.

2.1 Introduction

Dps proteins are bacterial mini-ferritins that protect DNA under stress conditions. Dps (DNA-binding protein from starved cells) proteins are thought to protect DNA from oxidative stress by utilizing their ferroxidase activity to deplete ferrous iron and hydrogen peroxide, which can otherwise produce damaging hydroxyl radicals via Fenton chemistry (*1*). Some Dps proteins also nonspecifically bind DNA, such as that from *E. coli*, which utilizes N-terminal lysine residues for DNA binding (*2*). Within cells, Dps is upregulated by the transcriptional regulator OxyR in response to oxidative stress (*3*), and is also upregulated in stationary phase when an additional physical component of Dps protection is biocrystallization with DNA (*4*).

Like other ferritins, Dps monomers assemble to form a spherical structure with a hollow core where oxidized iron can be stored reversibly (*5*) (Figure 1). However, unlike other ferritins which are 24-mer proteins, Dps proteins are dodecameric (12-mer) mini-ferritins. Furthermore, whereas in 24-mer ferritins the iron-binding ferroxidase sites are located within individual monomers (intrasubunit), in Dps proteins the ferroxidase sites are located at the intersection of two monomers (intersubunit), with ligands being supplied from both monomers (*1*).

The Dps protein family is involved in the survival of pathogenic bacteria in the oxidizing host environment. Macrophage cells in the human immune system produce reactive oxygen species (ROS) in order to kill invading bacteria. Dps is implicated in the survival and virulence of pathogenic bacteria such as *Bacteroides fragilis*, the most common

anaerobic species isolated from clinical infections which is both highly aerotolerant and resistant to oxidative stress (*6*), and *Borrelia burgdorferi*, the causative agent of Lyme's disease (*7*), among others (*8-12*). Dps has also been shown to protect *Salmonella enterica* serotype Enteritidis from the Fenton-mediated killing mechanism of bactericidal antibiotics (*13*). Moreover, Dps and Dps-like proteins have been investigated as vaccines in the treatment of *H. pylori* infection in humans (*14*), and *C. jejuni* infection in chickens (*11*). Thus, in the struggle between host and pathogen, oxidative stress is a key factor, and Dps is implicated in bacterial survival when confronted with either the host immune system or antibiotics. As the worldwide burden of antibiotic resistant bacteria continues to increase, new approaches are required to treat bacterial infections. Fully elucidating the mechanism by which Dps proteins protect pathogenic bacteria could inform the development of new antibiotics.

What is known about the mechanism by which Dps is protecting the bacterial genome? Previous experimentation toward revealing this protection mechanism has shown that Dps protects DNA from DNase cleavage (*15*), traps hydroxyl radicals, and inhibits DNA nicking by the Fenton reagents Fe^{2+} and H_2O_2 (*16*). We seek to determine more specifically the mechanism of *E. coli* Dps protection of DNA.

DNA has been shown to conduct charge efficiently through the π-stack of its nucleobases over long molecular distances in a diverse range of systems (*17*). DNA charge transport (CT) is proposed to be utilized within the cell, both in the long-range activation of redox-sensitive transcription factors and in facilitating scanning of the genome for damage by DNA-repair enzymes (*18,19*). Could ferritins similarly utilize DNA CT to exert their

protective effects from a distance? That is, must oxidizing equivalents diffuse specifically to the ferroxidase site of Dps, or can Dps become oxidized from a distance through DNA CT, thus protecting the surrounding DNA for potentially hundreds of base pairs?

The question of DNA-mediated long distance protection can be answered by generating guanine radicals using ruthenium flash-quench chemistry (*20*) and investigating if Dps protects the DNA from this oxidative damage (*21-22*). The flash-quench technique utilizes dipyridophenazine (dppz) complexes of ruthenium(II) that bind to DNA by intercalation (*23*). Here, racemic $[Ru(phen)(dppz)(bpy')]^{2+}$, where phen is 1,10-phenanthroline and bpy′ is 4-butyric acid-4′-methyl-2,2′-bipyridine, was covalently tethered to amine-modified DNA via the carboxylic acid moiety of the bpy′ ligand (*24*). In the first step, visible light promotes a $t_{2g} \rightarrow \pi^*$ metal-to-ligand CT transition of the Ru(II) complex (*25*). This Ru(II) excited state is then oxidatively quenched by a diffusing electron acceptor (Q), here $[Co(NH_3)_5Cl]^{2+}$, to form a highly oxidizing intercalated Ru(III) complex (1.6 V versus NHE, *26*). The *in situ* generated Ru(III) is competent to abstract an electron from DNA; the hole equilibrates along the DNA π-stack and localizes on guanine, the base with lowest oxidation potential (1.3 V versus NHE, *27*). The presence of adjacent guanines can further lower the guanine reduction potential, making the 5′-G of guanine doublets and triplets most readily oxidized (*28,29*). In this fashion, damage at the 5′-G of guanine repeats is considered a hallmark of one electron oxidative damage created through DNA CT. Further reaction of the guanine radical ($G^{\bullet}$) with H_2O or O_2 can form a mixture of irreversible oxidative products (*30*). These products are analogous to the DNA damage

products that can form in vivo as a result of oxidative stress. However, because the lifetime of the guanine radical is long (milliseconds, *23*) relative to the time scale of DNA CT (picoseconds, *31*), the guanine radical can also interact with DNA-bound, redox-active proteins. Thus electron transfer from Dps through the DNA π-stack could fill the hole on the guanine radical, restoring the integrity of the DNA (Figure 2). Guanine radicals can be monitored by cleaving irreversible guanine oxidation products on radiolabeled oligonucleotides and visualizing them through gel electrophoresis (*24*). In the presence of *E. coli* Dps, decreased guanine damage should be observed if Dps is protecting the DNA in this manner.

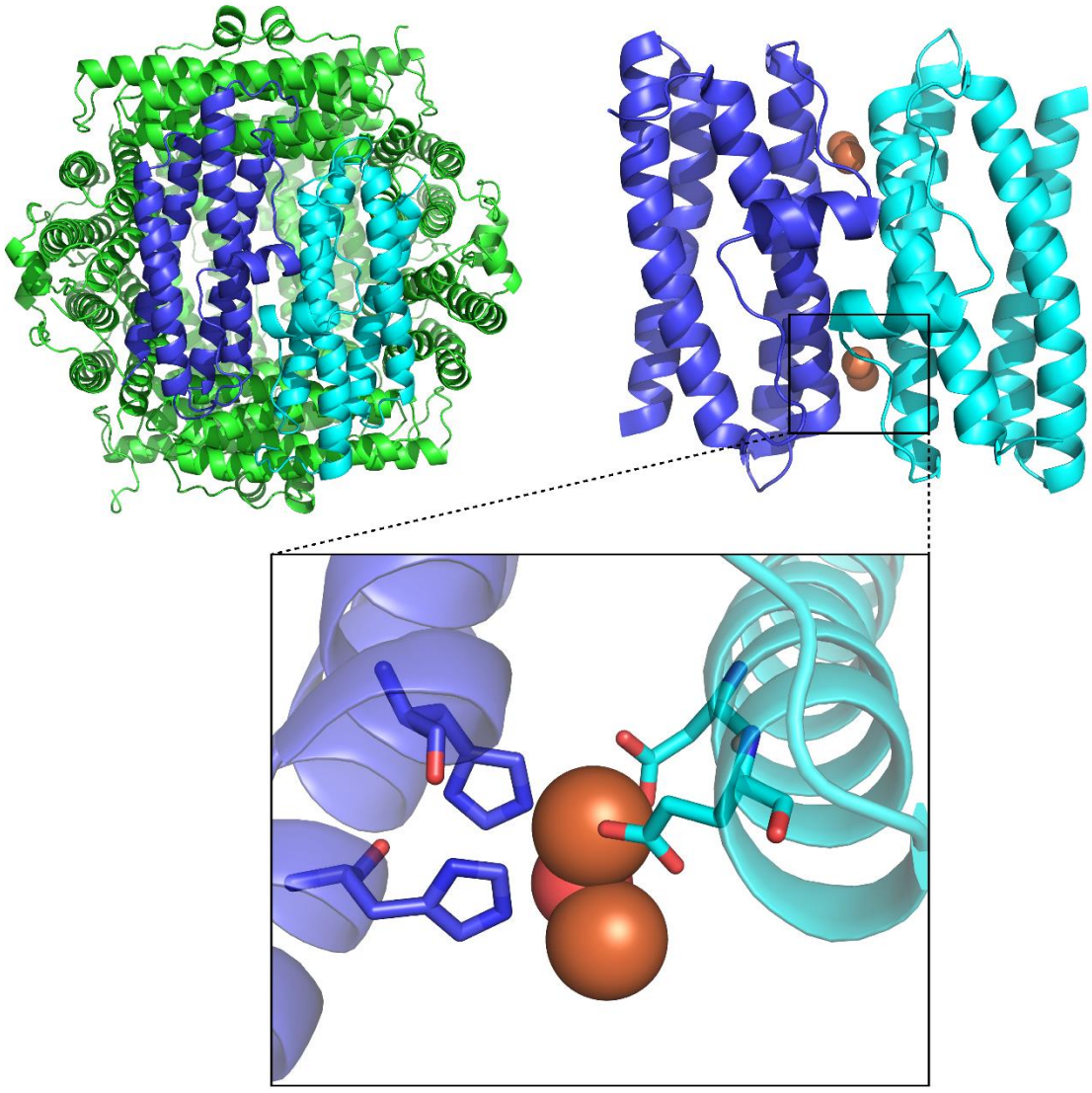

Figure 1. Structure of Dps. *Top Left*: *E. coli* Dps dodecamer, with two monomers highlighted in varying shades of blue (PDB: 1DPS). *Top Right*: *B. brevis* dimer, with irons bound at intersubunit ferroxidase site (PDB: 1N1Q). *Bottom*: Ferroxidase site of Dps proteins, showing iron atoms in brown, μ-oxo in red between the iron atoms, and the conserved ligating residues from each monomer: two histidines, one aspartate, and one glutamate residue.

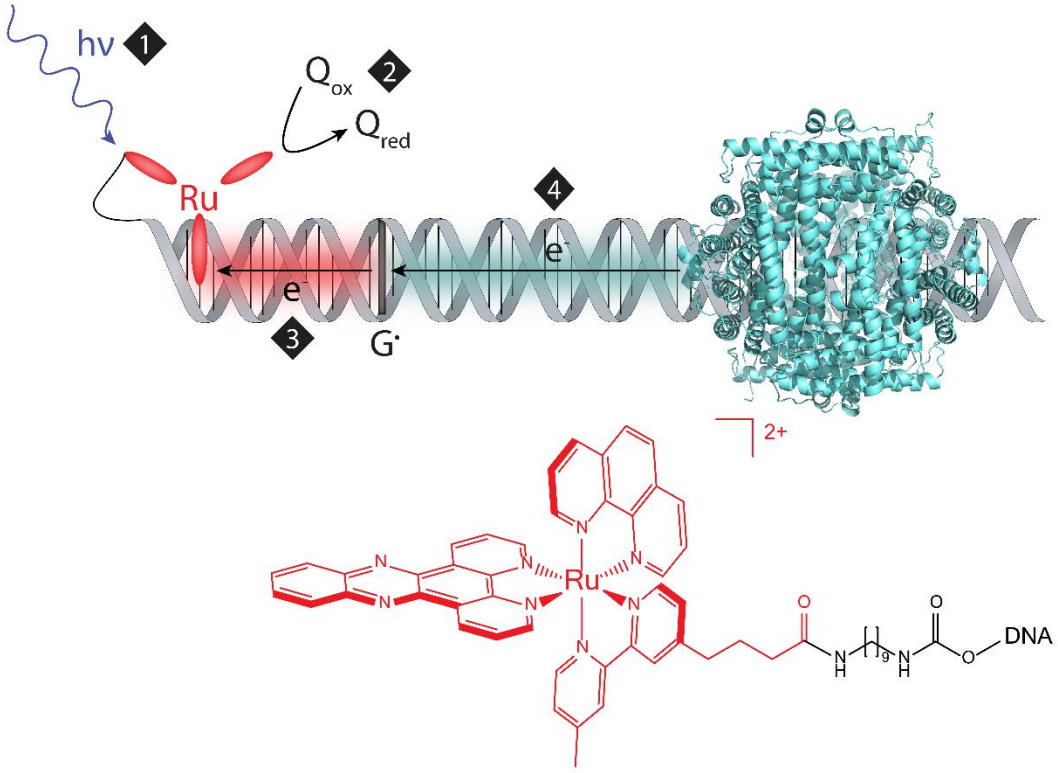

Figure 2. Schematic depicting DNA-mediated oxidation of Dps to fill the guanine radical hole generated by flash-quench chemistry. *Top*: Visible light excites an intercalated ruthenium(II) photooxidant (1), which is then oxidatively quenched (2) to a highly oxidizing Ru(III) species by a diffusing quencher (Q). This Ru(III) species is competent to abstract an electron from DNA (3); the hole equilibrates along the π-stack and localizes to the 5′-G of guanine repeats, the most easily oxidized base (G•). DNA CT from Dps to the guanine radical (4) could be a long distance protection mechanism. Note: the location and precise geometry for DNA binding of Dps are unknown. *E. coli* Dps PDB: 1DPS. *Bottom*: Structure of $[Ru(phen)(dppz)(bpy')]^{2+}$ covalently tethered to DNA via diaminononane linkage.

2.2 Experimental Section

2.2.1 Materials

All chemicals and starting materials were purchased from commercial sources and used as received. [Ru(phen)(dppz)(bpy′)]Cl_2, where phen = 1,10-phenanthroline, dppz = dipyrido[3,2-a:2′,3′-c]phenazine, and bpy′ = 4-butyric acid-4′-methyl-2,2′-bipyridine, was synthesized according to published methods (*32*), purified by reversed-phase chromatography, and characterized by NMR and ESI mass spectrometry (expected for the +2 ion: 409.62 m/z, observed: 410.2 m/z).

2.2.2 DNA synthesis and purification

Oligonucleotides were synthesized using standard phosphoramidite chemistry on an Applied Biosystems 3400 DNA synthesizer or purchased from Integrated DNA Technologies (Coralville, IA), purified using reversed-phase HPLC with a gradient of increasing acetonitrile, and characterized by MALDI-TOF mass spectrometry. The DNA sequences included a 70-mer: 5′-CTCTCGTCGTCAGTTGTCAAGTGTGCATGAAAGT AGAGTCTCGCTAAGCTCGGGA GAACAGAGAGATGCT-3′, and complementary 55-mer: 5′-TCCCGAGCTTAGCGAGACTCTACTTTCATGCACACTTGACAACTGACG ACGAGAG-3′, and 15-mer sequences: 5′-AGCATCTCTCTGTTC-3′. In order to covalently couple racemic [Ru(phen)(dppz)(bpy′)]Cl_2 to the 5′ end of the 15-mer, the DNA was modified (while on the solid support after DNA synthesis) with a 9-carbon saturated hydrocarbon tether terminating in an amine group to allow for amide coupling to the carboxylic acid moiety of the bpy′ ligand (*24*). Significant changes from published

methodology include the following: after tether addition, the samples were lyophilized to ensure dryness; *2-(1H-Benzotriazol-1-yl)-1,1,3,3-tetramethyluronium hexafluorophosphate (HBTU,* 11.6 μmol) was used in addition to previously described reagents in the ruthenium coupling step; metal coupling was allowed to proceed for 24 hours; and the final conjugates were cleaved from the solid support by incubating in NH_4OH for 4 hours at room temperature, followed by 3 hours at 60°C. The Ru-DNA conjugates were then purified by reversed-phase HPLC, characterized by MALDI-TOF mass spectrometry (expected: 5479 g/mol, observed: 5487.59, 5487.47, 5488.39, and 5487.80, for the 4 eluting isomers, respectively), and quantified based on their absorbance at 440 nm ($\varepsilon_{440} = 2.1 \times 10^4\ M^{-1}cm^{-1}$).

2.2.3 Site-directed mutagenesis

The H51G/H63G Dps double mutant was made with a Quikchange II-E Site-Directed Mutagenesis Kit (Stratagene) using the pBAD18-dps plasmid (containing the WT *E. coli dps* gene and an ampicillin resistance cassette) donated by Dr. Roberto Kolter (*33*) as a template. The H51G mutation was made first, and this mutagenized plasmid was used as a template to make the H63G mutation. Primers were purchased from Integrated DNA Technologies. All mutagenized plasmids were sequenced (Laragen) to confirm the desired sequences. After successfully creating the mutant pBAD18-dps plasmid, the *E. coli* cell line ZK2471 (dps::kan ΔrecA-(Cam) Δ*ara*714, leu::Tn10) donated by Dr. Roberto Kolter (*33*) was made electrocompetent and the plasmid was transformed via electroporation into these cells. Primer sequences were as follows, with mutagenized codon underlined:

H51G-forward: 5′-GATCTTTCTTTGATTACCAAACAAGCGGGCTGGAACATGC-3′

H51G-reverse: 5′-GCATGTTCCAGCCCGCTTGTTTGGTAATCAAAGAAAGATC-3′

H63G-forward: 5′-GCTAACTTCATTGCCGTAGGTGAAATGCTGGATGGCTTC-3′

H63G-reverse: 5′-GAAGCCATCCAGCATTTCACCTACGGCAATGAAGTTAGC-3′

2.2.4 Dps overexpression and purification

WT and H51G/H63G *E. coli* Dps were purified according to published procedures with a number of modifications (*15,16*). A single colony of *E. coli* cell line ZK2473, which consists of ZK2471 (detailed above) with the pBAD18-dps plasmid, was used to inoculate 50 mL of LB media containing 100 μg/mL ampicillin and 50 μg/mL kanamycin and was grown overnight at 37°C with 200 rpm shaking. The subsequent day, 5 mL of the overnight culture was used to inoculate 1 L cultures of LB containing the same concentrations of antibiotics, which were grown at 37°C with 150 rpm shaking until OD_{600} = 1. Overexpression of Dps was then induced with 0.3% w/v L-arabinose. After 4 hours of incubation at 37°C with continued shaking, the cells were harvested by centrifugation for 10 minutes at 7,000 *g*.

Cells were resuspended in Buffer A (50 mM Tris, pH 8, 500 mM NaCl, 0.1 mM EDTA) containing a protease inhibitor cocktail (Roche) and lysed via microfluidization. The cell lysate was clarified by centrifugation at 15,000 *g* for 15 minutes, followed by a second round of centrifugation of the supernatant at 27,000 *g* for 20 minutes. The resulting supernatant was fractionated by ammonium sulfate (AS) precipitation by slow addition of solid AS up to 60% saturated AS, centrifugation for 15 minutes at 10,000 *g*, and collection of the supernatant. Next, more solid AS was added to the supernatant up to 90% saturated

AS in order to precipitate Dps. The Dps protein was recovered by centrifugation for 20 minutes at 27,000 *g*, and the pellet resuspended in approximately 5 mL of Buffer A. The partially-purified Dps was then dialyzed against a low ionic strength buffer (20 mM Tris, pH 8), where it precipitated while colored contaminants remained in solution. Precipitated protein was isolated by centrifugation at 26,000 *g* for 10 minutes, and resuspended in Buffer B (50 mM Tris, pH 8, 2 M NaCl, 0.1 mM EDTA). The high salt concentration results in Dps dissociation from endogenous DNA.

Dps was separated from DNA and other contaminants by loading onto a HiLoad 16/600 Superdex 200 pg size exclusion column (GE Healthcare), and running with Buffer B. Fractions were pooled that had an A_{260}:A_{280} ratio of 0.57, indicating no nucleic acid contamination. Excess salt was removed by loading pooled fractions onto a HiPrep 26/10 desalting column (GE Healthcare) equilibrated with Buffer C (50 mM Tris, pH 7, 150 mM NaCl). Next, the partially purified Dps solution was loaded onto a HiTrap Heparin HP column (5 mL, GE Healthcare) using a peristaltic pump that had previously been equilibrated with Buffer C. The column was then washed with 3 column volumes (CV) of Buffer C, and Dps eluted with an increasing gradient of Buffer D (50 mM Tris, pH 7, 1 M NaCl) over 10 CV. Dps elutes at approximately 200 mM NaCl. Finally, purified Dps was exchanged into storage buffer (50 mM Tris, pH 7, 150 mM NaCl, 20% glycerol) using a HiPrep 26/10 desalting column (GE Healthcare). From 4 L of cell culture, the yield of purified Dps is approximately 130 mg. Protein purity was confirmed by SDS-PAGE (data not shown).

2.2.5 Iron loading and oxidation of Dps

Buffer (50 mM Tris, pH 7.00, 150 mM NaCl) was placed in a Schlenk flask and deoxygenated with at least 4 cycles of freeze-pump-thaw. Dps solutions were placed in a 5 mL Schlenk tube and deoxygenated by 4 sets of 10 cycles each of rapid dynamic vacuum followed by argon filling while constantly stirring, letting the protein stir under argon for 15 minutes between sets. Solid ferrous iron (as iron sulfate heptahydrate) was placed in a separate Schlenk tube and put under vacuum overnight. Solid sodium dithionite was dispensed under an anaerobic atmosphere into a sealed vial. All deoxygenated components were then brought into an anaerobic chamber (Coy); subsequent steps were accomplished within the anaerobic chamber. Dithionite was used to scavenge residual dioxygen.

First, buffer was prepared with sufficient dithionite such that when the dithionite-containing iron solution is added to the Dps solutions, the final dithionite concentration was approximately in 5-fold excess over the protein concentration. This dithionite-containing buffer was used to dissolve the solid ferrous iron. To load Dps with ferrous iron, Dps solutions were incubated with 2-fold excess ferrous iron (48 Fe^{2+}/Dps) for 2 hours. Excess iron and dithionite were then removed with small size exclusion columns (Micro Bio-Spin 6, Biorad) that had been exchanged into deoxygenated buffer. While as-purified Dps was considered to be Apo-Dps (with reliably ≤ 1 Fe/Dps), in order to control for the possibility of residual dithionite in the ferrous iron-loaded protein, Apo-Dps was treated with dithionite in the same manner as ferrous iron-loaded Dps. Specifically, Apo-Dps was incubated with dithionite buffer for 2 hours and subsequently passed through size exclusion columns in the

same manner as above. The UV-Visible absorbance spectrum of the ferrous iron-loaded protein was measured (Figure 3); no change is expected for ferrous iron binding.

A sample of iron-loaded Dps was removed from the anaerobic chamber in order to determine the Fe/Dps dodecamer. Protein concentrations were measured using the Bradford assay (Sigma). The iron concentration was determined based on the absorbance of $[Fe(bpy)_3]^{2+}$ (*34*). Protein (50 µL) was first denatured by addition of 2 M HCl (125 µL), and then precipitated with addition of 20% w/v trichloroacetic acid (125 µL). Precipitated protein was removed by centrifugation at 16,000 *g* for 20 minutes, and saturated sodium acetate (250 µL) was added to buffer the resulting supernatant. Iron was reduced with thioglycolic acid (6 µL) and chelated with 2,2′-bipyridine (50 µL of 0.4% w/v solution in 5% acetic acid). The absorbance of the resulting $[Fe(bpy)_3]^{2+}$ solution was measured at 522 nm and concentrations calculated using a molar absorptivity value of 8,790 $M^{-1}cm^{-1}$ derived from a standard curve of ferrous sulfate heptahydrate solutions. This derived value is comparable to the reported molar absorptivity for $[Fe(bpy)_3]^{2+}$ of 8,650 $M^{-1}cm^{-1}$ (*35*).

Ferrous-iron loaded Dps was chemically oxidized within the anaerobic chamber. Solid sodium ferricyanide was brought into the anaerobic chamber and resuspeded with deoxygenated buffer. 4-fold excess ferricyanide (based on 12 Fe^{2+}/Dps) was added to the ferrous-iron loaded Dps solutions and incubated for approximately 10 minutes. Ferricyanide was then removed by spin columns as described above. The UV-Visible spectrum of the iron-loaded protein was measured to confirm iron oxidation, characterized by increased absorbance at 310 nm (*16*).

2.2.6 Anaerobic Fe(II) fluorescence titration of Dps

Dps solutions, solid iron sulfate heptahydrate, and buffer solutions were deoxygenated as described above. MOPS buffer was used to allow comparison with iron loading results in Tris buffer, confirming similar results in different buffers. Samples were prepared in an anaerobic chamber (Coy), and measured in sealed cuvettes. Each sample contained 1 μM Apo-Dps with either buffer alone (50 mM MOPS, pH 7.00, 150 mM NaCl) or additionally 6, 12, 18, 24, or 36 Fe^{2+}/Dps. Dps solutions were incubated with ferrous iron for 10 minutes before spectra were taken. As a control, the spectra of 36 Fe^{2+}/Dps was retaken after an additional 2 hours of incubation, and was found to be almost identical (data not shown). Using an ISS-K2 spectrofluorometer, the solutions were excited at 280 nm, and emission measured from 300 to 400 nm. A spectrum of buffer alone has been subtracted from all traces.

2.2.7 Circular dichroism

Protein concentrations (5 μM) were determined using ε_{280} value calculated using the ExPASy ProtPram tool (http://web.expasy.org/protparam/). The calculated molar absorptivity values for both WT and H51G/H63G *E. coli* Dps dodecamers was ε_{280} = 185,640 $M^{-1}cm^{-1}$. Spectra were recorded at 25°C on a Model 430 circular dichroism spectrometer (AVIV) in a buffer consisting of 50 mM Tris, pH 7.0, 150 mM NaCl. The spectra shown are the average of three individual scans, with a buffer alone spectrum subtracted.

2.2.8 Guanine oxidation experiment

69-mer single-stranded DNA, with the same sequence as the 70-mer listed above but lacking the 3′-thymine, was radiolabeled with α-^{32}P-dTTP (Perkin Elmer) using standard protocols, treated with 10% piperidine for 30 minutes at 90°C to cleave any abasic sites, and purified by 20% denaturing PAGE as previously described (*36*). The radiolabeled 70-mer strand was then annealed with unlabeled 70-mer and complementary 55-mer DNA by heating at 90°C for 5 minutes, followed by slow cooling to room temperature, to result in an approximately 10% statistical radiolabel with roughly 1,000,000 cpm in each sample. After this first annealing step, the Ru-15-mer conjugate was added to the solution, heated to 65°C for 5 minutes, and again slowly cooled to room temperature. The annealed Ru-DNA samples were dried, brought into the anaerobic chamber, and resuspended with deoxygenated buffer (50 mM Tris, pH 7.00, 150 mM NaCl). Solid $[Co(NH_3)_5Cl]^{2+}$ was brought into the anaerobic chamber and also resuspended in deoxygenated buffer. Samples were prepared within the anaerobic chamber and transferred to septa-sealed NMR tubes. Protein-containing samples were incubated with DNA for 30 minutes prior to irradiation. In order to induce DNA damage via the flash-quench technique, the anaerobic samples were irradiated at 442 nm using a Hg/Xe arc lamp (Oriel) equipped with a monochromator and 320 nm long-pass filter, with total incident powers of approximately 3700 mJ/sample (2.4 – 3.2 mW, 20 – 25 minutes irradiation). Within each experiment, all samples were irradiated with identical lamp power. Samples containing both Dps and cobalt quencher precipitated upon irradiation; such precipitation was independent of Dps iron-loading. Following

irradiation, samples were aerobically treated with 10% piperidine for 30 minutes at 90°C to cleave the DNA at sites of oxidative guanine damage and subsequently dried on a centrifugal evaporator. Samples were resuspended with denaturing loading dye (80% formamide, 10 mM NaOH, 0.025% xylene cyanol, 0.025% bromophenol blue in 90 mM Tris-borate). After heating at 90°C for 2 minutes, identical scintillation counts were loaded for each sample onto a 20% denaturing polyacrylamide gel, and electrophoresed at 90 W for 2 hours.

DNA damage was quantified by phosphorimagery (ImageQuant TL). Specifically, oxidative DNA damage was quantified for each lane by the ratio of guanine triplet damage to the undamaged parent band. Each protein set (i.e., Apo-Dps 0, 2, 4, and 6 μM) was then normalized to the lane with no added protein. The fold damage attenuation was calculated by dividing the normalized level of DNA damage in the no protein lane by that in the lane with maximal protein concentration (i.e., "0 μM Apo-Dps" / "6 μM Apo-Dps"). Values given in the text are the average of three separate experiments; errors are given as standard deviation.

2.2.9 Gel-shift assays

In an anaerobic chamber (Coy), 10 nM of 100% 5′-^{32}P-radiolabeled 70-mer DNA with the complementary 70-mer strand was incubated with 0 – 600 nM Apo-Dps, ferrous iron-loaded Dps or ferric iron-loaded Dps for 25 minutes in 50 mM Tris, pH 7.00, 150 mM NaCl, 20% glycerol. Deoxygenation procedures for all components were the same as described above. Within the anaerobic chamber, samples were then loaded onto 10% TBE gels and electrophoresed for 1 hour at 50 V at room-temperature in 0.5 X TBE. The DNA

embedded in the gel matrix was aerobically transferred to an Amersham Hybond-N membrane (GE Healthcare) via electroblotting and quantified by phosphorimagery (ImageQuant TL). Dps-DNA complexes did not enter the gel matrix; thus, gels were quantified by the disappearance of the free DNA band with increasing titration of Dps. The fraction of free DNA, relative to the amount of DNA with no added protein, was plotted versus protein concentration for each iron loading condition of Dps (data not shown). These data were fit sigmoidally, and the fit used to solve for the protein concentration where the fraction of free DNA was 0.5. The K_d values extracted in this manner are 260 nM for Apo-Dps, 230 nM for ferrous iron-loaded Dps, and 310 nM for ferric iron-loaded Dps.

2.2.10 Ruthenium luminescence

Samples were prepared in an anaerobic chamber (Coy), and measured in sealed cuvettes. Steady-state experiments were performed with an ISS-K2 spectrofluorometer. Solutions were excited at 440 nm, and emission measured from 500 to 800 nm. A spectrum of buffer alone has been subtracted from all traces. For studies with non-covalent ruthenium, samples contained various combinations of 8 μM non-covalent $[Ru(phen)(dppz)(bpy')]^{2+}$, 8 μM unmodified duplexed 70mer DNA, 8 μM ferrous iron-loaded Dps (11.4 ± 0.2 Fe/Dps dodecamer) in 50 mM Tris, pH 7.0, 150 mM NaCl. For studies with covalent ruthenium, each sample contained 8 μM duplexed Ru-DNA (70-mer DNA with complementary Ru-15-mer and 55-mer strands) with either buffer alone (50 mM Tris, pH 7.0, 150 mM NaCl) or additionally 8 μM Dps solutions with varying iron loading (Apo-Dps and Dps loaded with either ferrous (11.8 ± 0.2 Fe/Dps dodecamer) or ferric iron).

Slight precipitation occurred for the sample containing Ru-DNA and ferric iron-loaded Dps, resulting in a raised baseline.

Time-resolved emission measurements were carried out at the Beckman Institute Laser Resource Center using the third harmonic (355 nm) of a 10 Hz, Q-switched Nd:YAG laser (Spectra-Physics Quanta-Ray PRO-Series) with a pump pulse duration of 8 nanoseconds. The third harmonic used to pump an optical parametric oscillator (OPO, Spectra-Physics Quanta-Ray MOPO-700) in order to achieve laser excitation at 470 nm. Samples were held in sealed 1 cm path length cuvettes equipped with stir bars and irradiated at 470 nm with laser powers of 3.3 mJ/pulse. Samples contained 20 μM non-covalent $[Ru(phen)(dppz)(bpy')]^{2+}$, 1 mM basepairs of the alternating copolymer $poly(dGdC)_2$, and either 6 μM of ferrous iron-loaded Dps (12.0 ± 0.1 Fe/Dps dodecamer) or 400 μM of $[Ru(NH_3)_6]^{3+}$ in a buffer of 50 mM Tris, pH 7.0, 150 mM NaCl. Samples with $poly(dGdC)_2$ and Ru alone, as well as in the presence of ferrous-iron loaded Dps, contained residual 3.3% glycerol, whereas the $[Ru(NH_3)_6]^{3+}$ sample contained no glycerol. Emission decays were fit to a bi-exponential function and the following kinetic parameters obtained: $poly(dGdC)_2$ + Ru: lifetimes of 31 ns and 132 ns with 25% and 75% contributions, respectively; $poly(dGdC)_2$ + Ru + $[Ru(NH_3)_6]^{3+}$: lifetimes of 36 ns and 102 ns with 42% and 58% contributions; $poly(dGdC)_2$ + Ru + Fe(II)-Dps: lifetimes of 34 ns and 133 ns with 25% and 75% contributions.

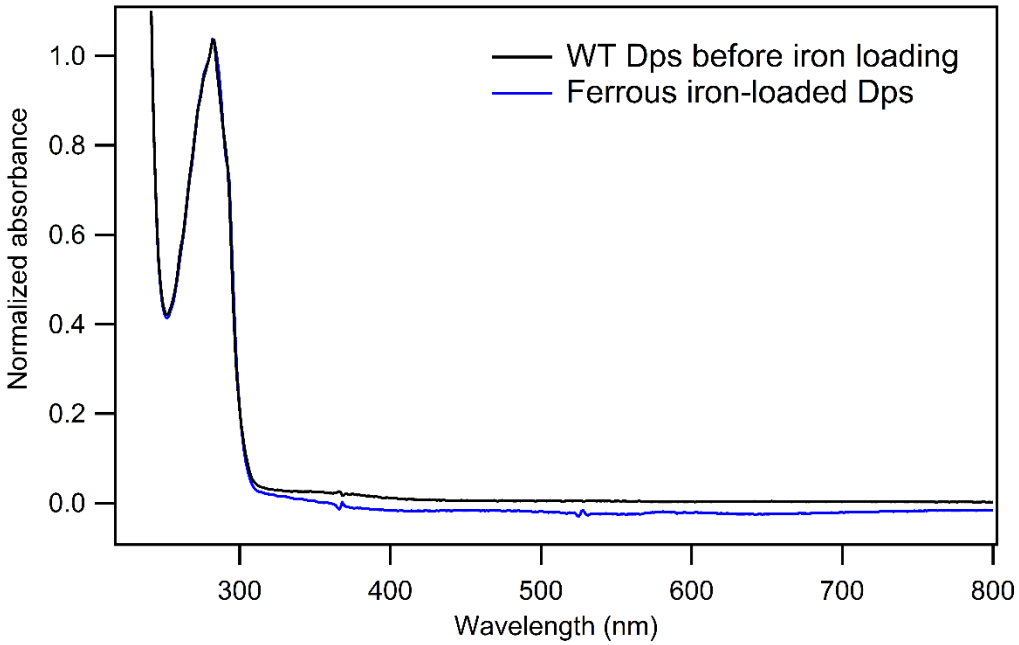

Figure 3. Comparison of UV-Visible absorption spectra of Dps before (black) and after (blue) anaerobically loading with ferrous iron; no change in the UV-Visible spectra of Dps is expected upon binding of ferrous iron. Protein spectra were normalized to A_{280}. Buffer: 50 mM Tris, pH 7.0, 150 mM NaCl.

2.3 Results and Discussion

2.3.1 Ferrous iron loading and chemical oxidation of Dps

At the intersubunit ferroxidase sites of Dps, ferrous iron is bound, oxidized, and then shuttled to the protein core where it is stored (*1*). Two conserved histidines together with glutamate and aspartate residues ligate two iron atoms (Figure 1), creating one relatively high affinity iron site and another with much lower affinity. It seemed reasonable to consider that any protective effects of Dps would vary as a function of the iron content of the protein. We sought to compare the protective effects of Apo-Dps with Dps in which the ferroxidase site was loaded with either ferrous or ferric iron.

If all of the di-iron sites of dodecameric Dps are fully occupied, this would correspond to 24 Fe/Dps. As-purified Dps was considered to be Apo-Dps, with reliably ≤1 Fe/Dps (based on the absorbance of $[Fe(bpy)_3]^{2+}$, see experimental section for details). The ferroxidase sites of Dps were anaerobically loaded with ferrous iron by incubating the protein with excess ferrous iron and dithionite for 2 hours and subsequently removing the dithionite and unbound iron using small size-exclusion columns. Despite using excess ferrous iron and long incubation times, reliably only 12 Fe^{2+}/Dps were bound under anaerobic conditions. A linear increase in the quenching of intrinsic protein fluorescence upon anaerobic titration of ferrous iron to Apo-Dps from 0 to 12 Fe/Dps, coupled with minimal quenching past this stoichiometry, supports the observed 12 Fe^{2+}/Dps (Figure 4). In *Bacillus anthracis* Dps, only one iron per ferroxidase site binds appreciably under anaerobic conditions because of the

difference in affinity between the iron sites; a bridging oxidant seems to be required to form the di-iron site (*21*). Similar results were observed with *Listeria innocua* Dps (*22*).

To then confirm specific iron binding to the ferroxidase site of *E. coli* Dps, a double mutant was prepared where both ligating histidines were changed to glycines: H51G/H63G Dps. Similar secondary structure to the wild-type protein was established by circular dichroism spectroscopy (Figure 5). Under identical conditions, the wild-type protein bound 11.8 ± 0.2 Fe^{2+}/Dps, whereas the H51G/H63G mutant bound only 1.0 ± 0.3 Fe^{2+}/Dps, demonstrating that these mutations did indeed abolish iron binding (Figure 6). Therefore we observe specific iron binding only to the higher affinity iron site under these anaerobic conditions for *E. coli* Dps. Ferrous iron-loaded Dps was then oxidized anaerobically using potassium ferricyanide (Figure 7), which was removed in the same fashion as above. While evidence suggests that the preferred oxidant for Dps is hydrogen peroxide (*16*), compared to dioxygen for maxi-ferritins, addition of even sub-stoichiometric quantities of hydrogen peroxide led to Dps precipitation. Regardless of the oxidant (hydrogen peroxide or ferricyanide), the important factor is that with oxidized iron, electrons are not available from Dps to fill guanine radical holes. Iron oxidation was evidenced by a characteristic increase in absorbance at 310 nm (*16*).

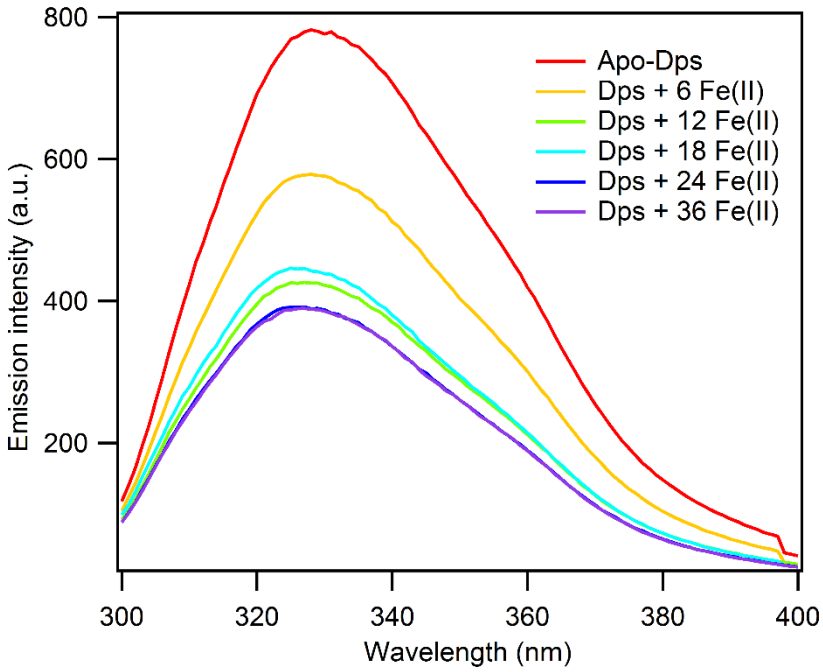
Apo-Dps
Dps + 6 Fe(II)
Dps + 12 Fe(II)
Dps + 18 Fe(II)
Dps + 24 Fe(II)
Dps + 36 Fe(II)
Emission intensity (a.u.)
800
600
400
200
300
320
340
360
380
400
Wavelength (nm)

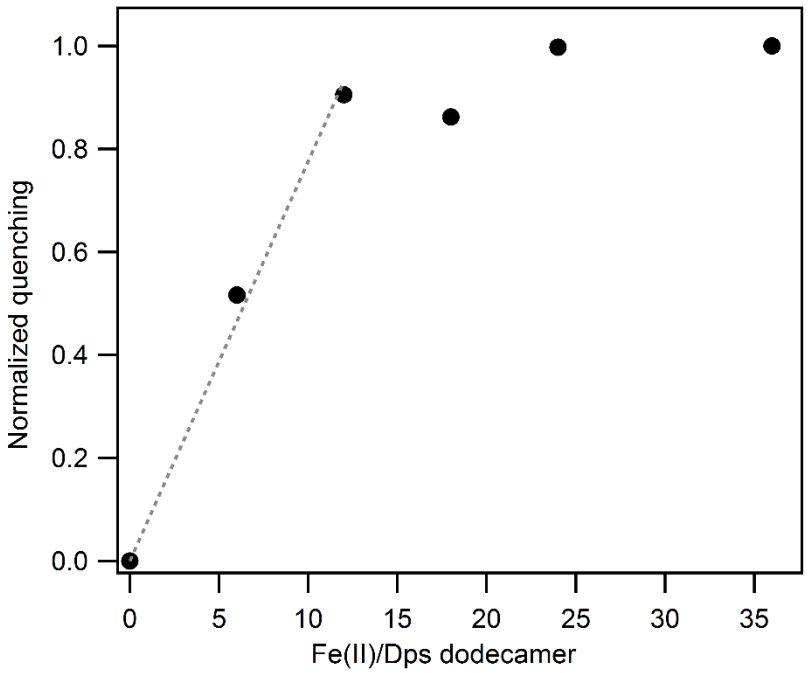
Normalized quenching
1.0
0.8
0.6
0.4
0.2
0.0
0
5
10
15
20
25
30
35
Fe(II)/Dps dodecamer

Figure 4. Anaerobic titration of *E. coli* Dps with ferrous iron, which quenches the intrinsic protein fluorescence. *Top*: Emission spectra of Apo-Dps compared to Dps that has been incubated with 6, 12, 18, 24 or 36 Fe(II)/Dps dodecamer (excitation wavelength = 280 nm). Protein concentration was 1 μM in a buffer of 50 mM MOPS, pH 7.00, 150 mM NaCl. *Bottom*: Plot of fluorescence quenching, normalized to quenching observed with 36 Fe(II)/Dps, versus the number of Fe(II)/Dps. A linear fit to the 0 to 12 Fe(II)/Dps data yields a line with the equation $y = 0.0776x$, with an R^2 value of 0.99.

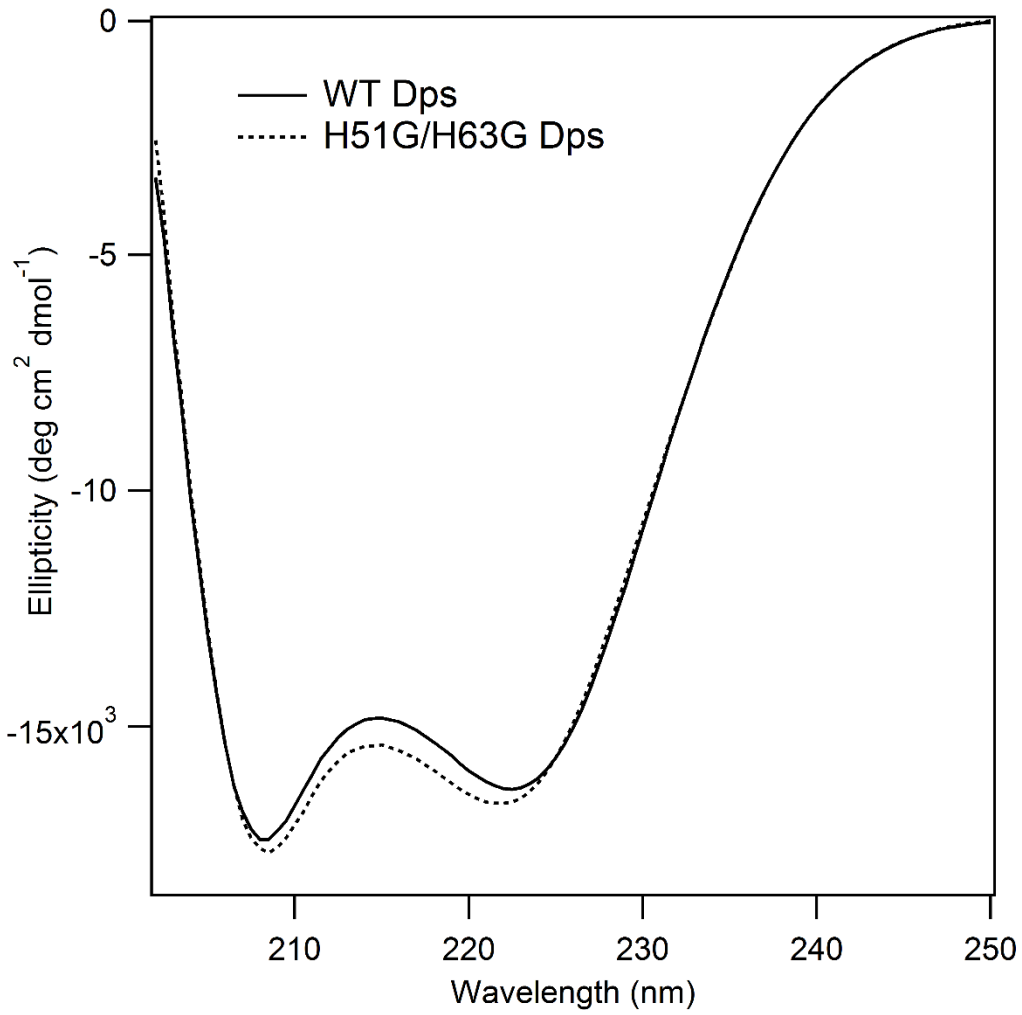

Figure 5. Circular dichroism spectra of wild-type (WT) (solid line) and H51G/H63G *E. coli* Dps (dashed line). Protein concentration was 5 μM in a buffer of 50 mM Tris, pH 7.00, 150 mM NaCl.

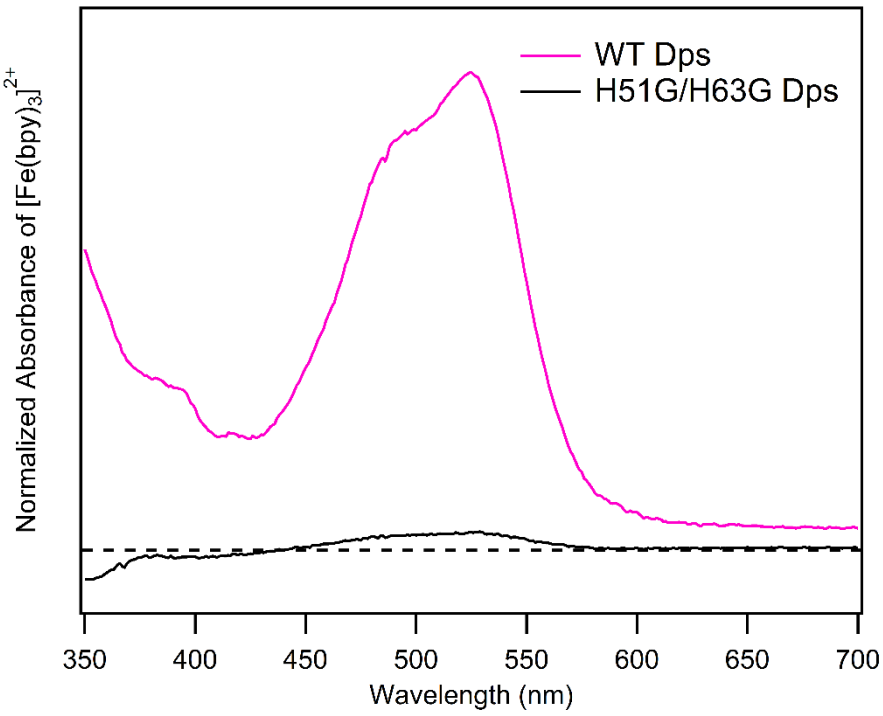

Figure 6. Ferrous iron loading of Dps ferroxidase mutant H51G/H63G compared to WT *E. coli* protein. Normalized UV-Visible spectra of $[Fe(bpy)_3]^{2+}$ produced from either WT Dps (pink) or H51G/H63G Dps (black). For normalization, the absorbance values were divided by protein concentration. The calculated number of iron atoms per Dps dodecamer is 11.8 ± 0.2 for WT Dps and 1.0 ± 0.3 for H51G/H63G Dps. Protein concentrations were determined via the Bradford assay; the concentration of $[Fe(bpy)_3]^{2+}$ was determined by A_{522} using a derived extinction coefficient of 8,790 $M^{-1}cm^{-1}$.

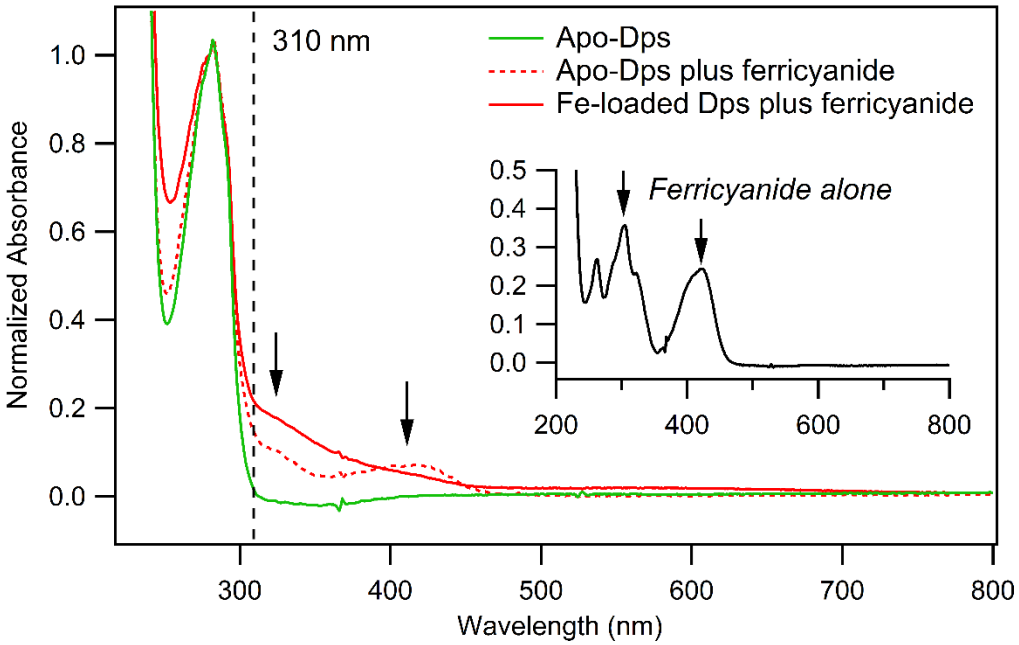

Figure 7. Oxidation of ferrous iron-loaded *E. coli* Dps by stoichiometric potassium ferricyanide. All protein spectra were normalized to A_{280}. Apo-Dps (4 μM), shown in green, has minimal spectral features other than the characteristic protein absorbance at 280 nm. Apo-Dps with ferricyanide (4 μM each), shown as dashed red line, additionally shows characteristic spectral features of ferricyanide (inset, arrows). Ferrous-iron loaded Dps (4 μM), shown as solid red line, that has been incubated with stoichiometric ferricyanide displays a distinct increase in absorbance at 310 nm (dashed black vertical line), as expected for iron oxidation. Note that ferrocyanide is spectroscopically silent. A similar A_{310} increase was observed for oxidation by dioxygen (data not shown).

2.3.2 Inhibition of guanine damage by Dps

To compare the level of DNA protection by Dps as a function of protein iron loading, samples containing 3′-^{32}P labeled 70-mer duplex DNA appended with 5′-covalently tethered $[Ru(phen)(dppz)(bpy')]^{2+}$ (6 μM), the diffusing quencher $[Co(NH_3)_5Cl]^{2+}$ (600 μM), and 0–6 μM of ApoDps, ferrous iron-loaded Dps, or ferric iron-loaded Dps were irradiated anaerobically at 442 nm to avoid dioxygen oxidation of ferrous iron-loaded Dps. The locations of DNA damage thus generated via flash-quench chemistry were then revealed by treatment with hot piperidine, which cleaves the DNA backbone at sites of oxidative guanine lesions (*30*) and subsequent visualization by denaturing gel electrophoresis. Figure 8 shows a representative gel featuring the differential effects of Dps with varying iron content.

In the absence of Dps, damage is evident predominantly at the 5′-G of the guanine triplet, as expected with one electron DNA oxidation through long-range DNA CT. Hydroxyl radical damage leads instead to damage at all guanines. When any component is missing, such as in the dark control (DC), which is the full sample (containing DNA, photooxidant, and quencher) but not irradiated, or light control 1 (LC1), which is the sample irradiated but in the absence of quencher, no damage is observed. In order to compare the differential effects of iron loading, experiments were performed in triplicate, and oxidative DNA damage was quantified for each lane by the ratio of guanine triplet damage to the undamaged parent band. Ferrous iron-loaded Dps (6 μM) attenuates oxidative DNA damage at the guanine triplet by an average of almost 5-fold (4.9 ± 1.5), whereas equivalent concentrations of Apo-Dps and ferric iron-loaded Dps have relatively

little effect (1.1 ± 0.5 and 1.3 ± 0.7 fold attenuation, respectively). One-way analysis of variance (ANOVA) was performed on the fold decrease data of triplicate experiments with Apo-Dps, ferric iron-loaded Dps, and ferrous iron-loaded Dps. Using the null hypothesis that the three average fold decrease values are the same, an F value of 13.272 was obtained, corresponding to a p value of 0.0062. Thus because $p < 0.01$, we can state at a 99% confidence level that these average fold decrease values are different.

Thus increasing equivalents of Dps loaded with ferrous iron, in contrast to Apo-Dps and ferric iron-loaded Dps which lack available reducing equivalents, significantly decrease the level of DNA damage at guanine repeats, as can be clearly seen in the lane profile comparisons in Figure 8, indicating the importance of both the presence and oxidation state of iron in Dps. It is noteworthy that iron-loaded Dps binds DNA similarly to Apo-Dps (K_d values of approximately 300 nM), as determined via gel-shift assays (see experimental section for details), negating the possibility of a differential binding effect.

Free ferrous iron diminishes damage, as shown by a control which is the full sample in the absence of protein with the addition of free ferrous iron at a concentration equivalent to that in ferrous iron-loaded Dps ("free Fe^{2+}" in Figure 8). To determine if free iron is generated by the irradiation of ferrous iron-loaded Dps, the iron content of a sample was measured before and after irradiation, while ensuring removal of any unbound iron from the irradiated sample by size-exclusion chromatography. The iron content before and after irradiation (12.2 ± 0.3 and 11.8 ± 0.1 Fe/Dps, respectively) was found to be identical, indicating no iron labilization. In view of these controls, the difference in damage

attenuation for ferrous iron-loaded Dps compared to Apo-Dps and ferric iron-loaded Dps indicates that Dps containing ferrous iron can become oxidized, perhaps via DNA CT, to fill the hole on guanine radicals.

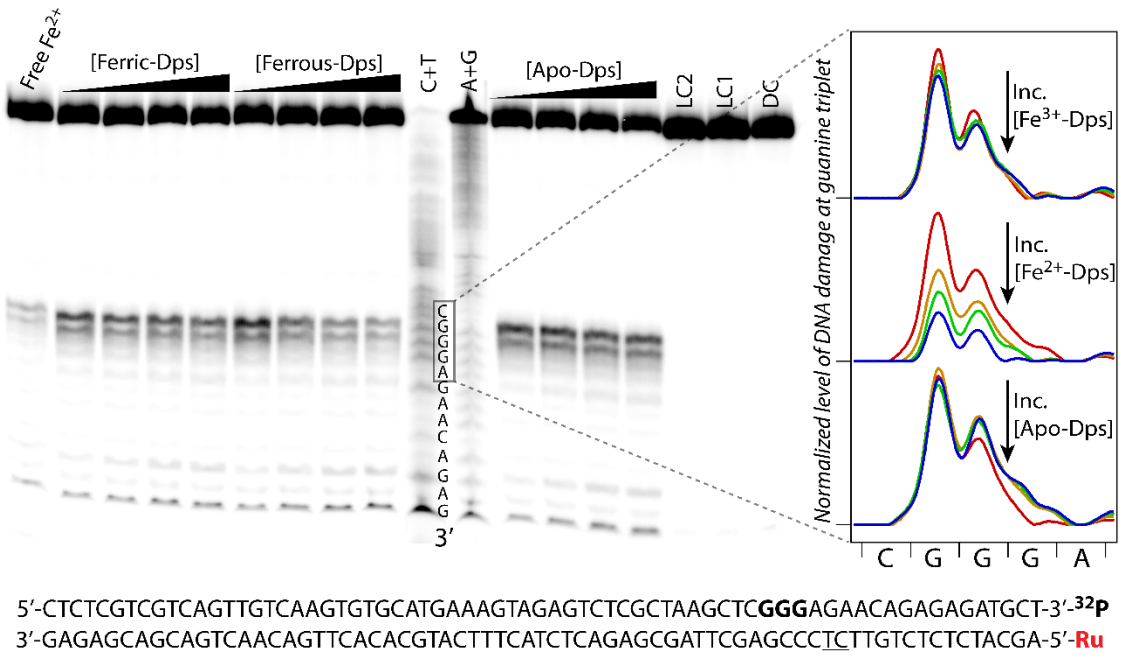

Figure 8. Representative gel comparing ability of Apo-Dps, ferrous iron-loaded Dps, and ferric iron-loaded Dps to protect DNA from damage created via flash-quench chemistry. *Left*: Autoradiogram of gel showing effect of increasing Dps with varying iron loading. Conditions: 6 μM statistically 3′-^{32}P-labeled 70 mer Ru-DNA, 600 μM $[Co(NH_3)_5Cl]^{2+}$, Dps concentrations from 0 to 6 μM, buffer: 50 mM Tris, pH 7.0, 150 mM NaCl. A+G and C+T are Maxam–Gilbert sequencing lanes. Controls: DC contains all components (DNA, photooxidant, and quencher) but is not irradiated; light control 1 (LC1) is irradiated but lacks quencher; LC2 is irradiated, lacking quencher, but contains 6 μM Dps loaded with ferric iron; free Fe^{2+} is irradiated, containing all components but protein, with the addition of free ferrous iron at a concentration equivalent to that in ferrous iron-loaded Dps. The number of Fe/Dps in ferrous iron-loaded Dps was 10.8 ± 0.1. *Right*: Lane profiles comparing normalized level of DNA damage at the guanine triplet upon titration of ferric iron-loaded Dps (upper), ferrous iron-loaded Dps (middle), or Apo-Dps (lower) from 0 μM protein (red), 2 μM protein (orange), 4 μM protein (green), to 6 μM protein (blue). *Lower*: DNA sequence, with guanine triplet shown bolded, and the location of a nick in the DNA backbone underlined. For higher synthetic yield, the DNA was made in two pieces (55-mer and Ru-15-mer); breaks in the sugar-phosphate backbone do not affect long-range CT.

2.3.3 Ru-DNA luminescence with Dps

In order to definitively establish long-range oxidation of ferrous iron-loaded Dps via DNA charge transport, ideally a mismatch experiment would be performed. Mismatches and DNA lesions attenuate DNA CT because they disrupt π-stacking of the nucleobases (*39,40*). If a mismatch can be engineered between the site of protein binding on the DNA and the location of the guanine multiplet, a decreased level of damage inhibition would be expected compared to intervening well-matched DNA. A similar experiment was performed with the transcription factor p53 which binds to a defined consensus sequence (*41*).

However, Dps binds DNA non-specifically using N-terminal lysine residues (*2*), so the exact location of Dps binding along the DNA is unknown. Nevertheless, mismatch experiments were attempted where either a C:A mismatch or abasic site was engineered 21 bases from the 5′ end of the 70-mer duplex where the ruthenium photooxidant is tethered (2 base-pairs intervening between mismatch and guanine triplet). Little difference was observed in damage inhibition by ferrous iron-loaded Dps between the well-matched, mismatched, and abasic sequences because of the non-specific DNA binding of Dps. Additionally, these experiments are performed under conditions of a large excess of sacrificial Co^{3+} quencher and relatively long irradiation times (20 minutes); until the Co^{3+} quencher has been exhausted, electron holes will be repeatedly injected into the DNA π-stack. Therefore, even if some DNA-binding locations do not facilitate protein oxidation via DNA-mediated CT, Dps may diffuse to other regions of the DNA during the time of this experiment.

Instead we use luminescence experiments to determine if there is any direct interaction between the Ru photooxidant and Dps. If our hypothesis is correct that DNA is a necessary intermediate in the oxidation of ferrous iron-loaded Dps, there should be no direct interaction between the Ru photooxidant and Dps. Interaction with the ruthenium (II) excited state can be probed by measuring the luminescence of the Ru-DNA alone, and then in the presence of Dps. If the protein is interacting with the ruthenium (II) excited state, quenching would be expected both in steady-state and time-resolved experiments.

Figure 9A shows the results of non-covalent steady-state ruthenium luminescence experiments. $[Ru(phen)(dppz)(bpy')]^{2+}$ is a DNA light-switch complex: whereas its luminescence is quenched in aqueous solution, upon the addition of DNA the ruthenium complex luminesces intensely (*42*). Accordingly, while no luminescence is apparent in a solution of $[Ru(phen)(dppz)(bpy')]^{2+}$ alone, luminescence is restored upon the addition of un-modified 70mer DNA. Importantly, the further addition of ferrous-iron loaded Dps has no effect on the DNA-bound ruthenium luminescence, indicating no quenching of the ruthenium (II) excited state by Dps. Also, no luminescence is observed in a sample that contains ruthenium and ferrous-iron loaded Dps, but lacks DNA, indicating that the ruthenium complex does not intercalate into the protein fold. Moreover, the steady-state luminescence of covalently tethered Ru-DNA is not quenched in the presence of Apo-Dps, ferrous iron-loaded Dps, or ferric iron-loaded Dps (Figure 9B).

Time-resolved emission experiments probed the behavior of the ruthenium (II) excited state on a nanosecond timescale (Figure 9C). In the absence of additional reagents,

non-covalent $[Ru(phen)(dppz)(bpy')]^{2+}$ bound to poly(dGdC)$_2$ DNA decays in less than a microsecond. In the presence of a known oxidative quencher, $[Ru(NH_3)_6]^{3+}$, the ruthenium (II) excited state decays more quickly as a result of this quenching process. However, upon the addition of ferrous iron-loaded Dps to a sample of Ru photooxidant and poly(dGdC)$_2$ DNA, identical decay kinetics were observed as in the absence of Dps. Therefore, both steady-state and time-resolved emission experiments show no quenching of the ruthenium (II) excited state with Dps, confirming no direct interaction and suggesting that the DNA a necessary intermediate in the oxidation of ferrous iron-loaded Dps.

Further controls for this interaction are samples in the guanine oxidation assay which were irradiated and lack quencher but contain 6 μM Dps loaded with ferric iron or ferrous iron (LC2 in Figure 8 and LC3 in Figure 10, respectively). If iron-loaded Dps oxidatively quenched Ru(II)* to form Ru(III), guanine damage would be apparent in these samples. The lack of guanine damage in these controls again confirms the absence of direct interaction between the ruthenium (II) excited state and Dps.

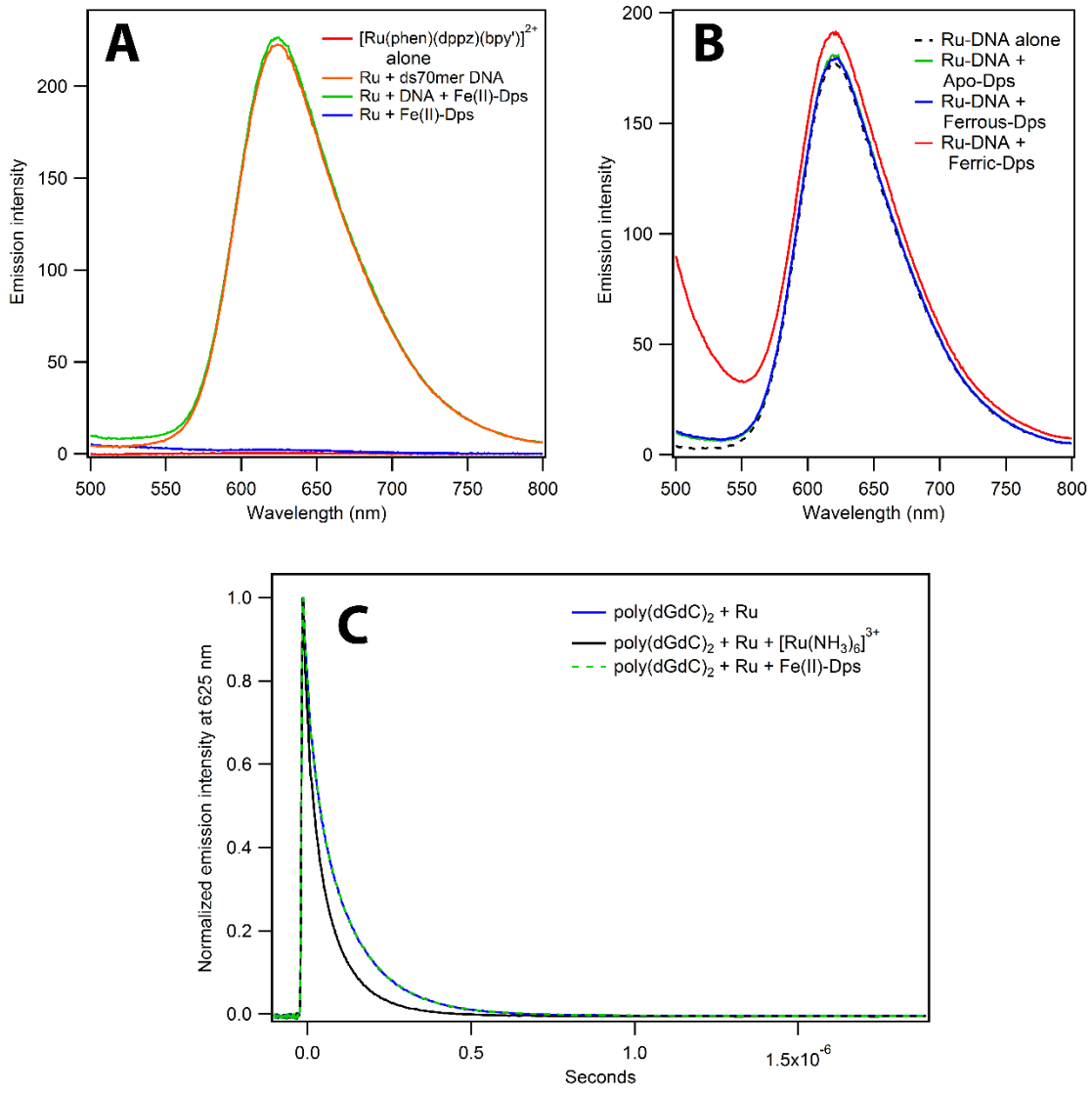

Figure 9. DNA-bound ruthenium luminescence in absence and presence of Dps. All samples prepared and measured anaerobically. Steady-state emission spectra with non-covalent (*A*) and covalent $[Ru(phen)(dppz)(bpy')]^{2+}$ (*B*) utilized an excitation wavelength of 440 nm. In *9A*, samples contained various combinations of 8 μM non-covalent $[Ru(phen)(dppz)(bpy')]^{2+}$, 8 μM unmodified duplexed 70mer DNA, 8 μM ferrous iron-loaded Dps (11.4 ± 0.2 Fe/Dps dodecamer). In *9B*, samples contained 8 μM duplexed 70-mer DNA with covalently tethered $[Ru(phen)(dppz)(bpy')]^{2+}$ alone or with 8 μM Apo-Dps, ferrous iron-loaded Dps (11.8 ± 0.2 Fe/Dps dodecamer) or ferric iron-loaded Dps. Slight precipitation occurs for the sample containing Ru-DNA and ferric iron-loaded Dps,

resulting in a raised baseline. For the nanosecond time-resolved emission spectra in *9C*, samples were excited at 470 nm and contained 20 μM non-covalent $[Ru(phen)(dppz)(bpy')]^{2+}$, 1 mM basepairs of the alternating copolymer $poly(dGdC)_2$, and either 6 μM of ferrous iron-loaded Dps (12.0 ± 0.1 Fe/Dps dodecamer) or 400 μM of $[Ru(NH_3)_6]^{3+}$. Samples with $poly(dGdC)_2$ and Ru alone, as well as in the presence of ferrous-iron loaded Dps, contained residual 3.3% glycerol, whereas the $[Ru(NH_3)_6]^{3+}$ sample contained no glycerol. For all, buffer was 50 mM Tris, pH 7.0, 150 mM NaCl.

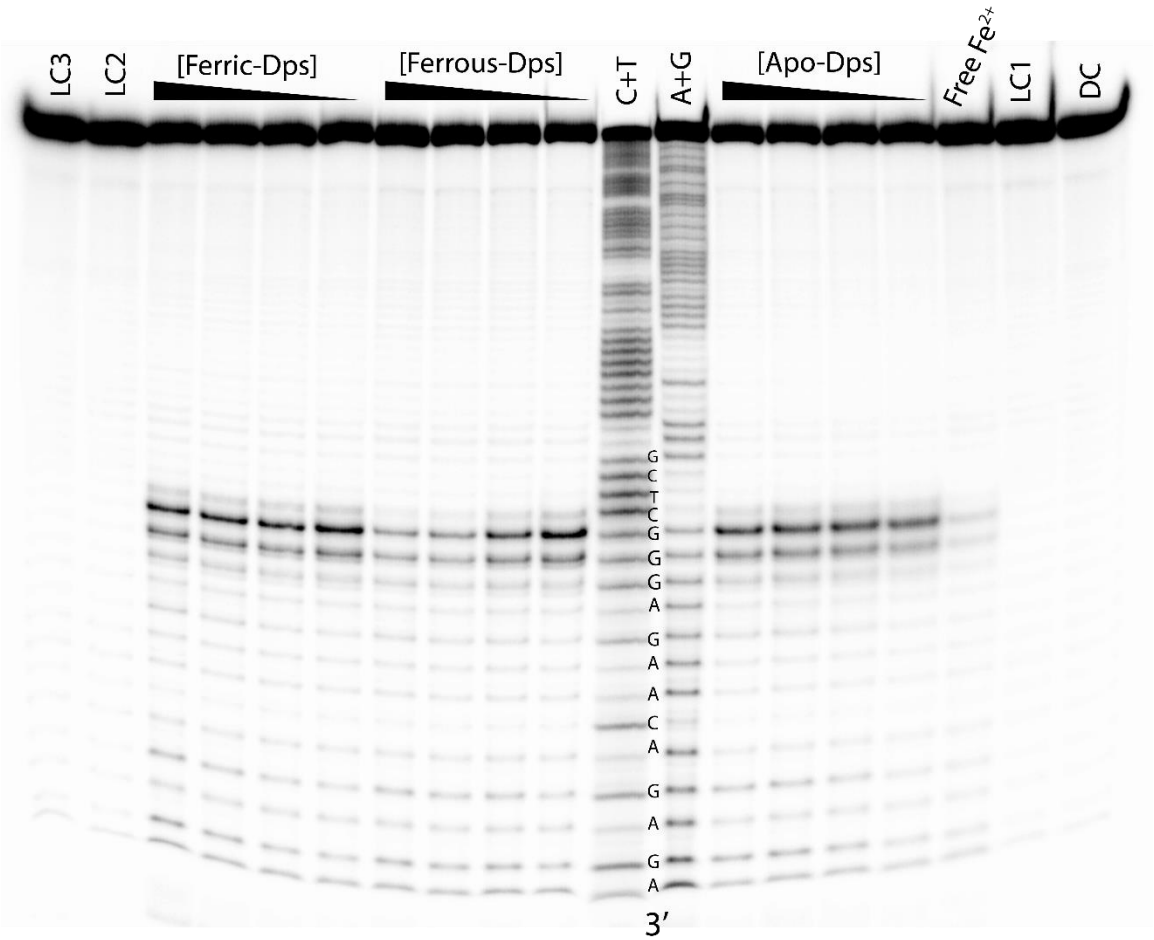

Figure 10. Autoradiogram of gel comparing ability of Apo-Dps, ferrous iron-loaded Dps, and ferric iron-loaded Dps to protect DNA from damage created via flash-quench chemistry, showing reproducibility of result as well as additional control (LC3). A+G and C+T are Maxam-Gilbert sequencing lanes. Controls: Dark control (DC) contains all components (DNA, photooxidant, and quencher) but is not irradiated; Light control 1 (LC1) is irradiated but lacks quencher; LC2 is irradiated, lacking quencher, but contains 6 μM Dps loaded with ferric iron; LC3 is irradiated, lacking quencher, but contains 6 μM Dps loaded with ferrous iron; "Free Fe2+" is irradiated, containing all components, but additionally free ferrous iron at a concentration equivalent to that in ferrous iron-loaded Dps. The number of Fe/Dps in ferrous iron-loaded Dps was 13.6 ± 0.6.

2.4 Conclusions

Thus it appears that ferrous iron-loaded Dps, but not Apo-Dps or ferric iron-loaded Dps which lack reducing equivalents, can protect DNA from oxidative damage by becoming oxidized to fill guanine radical holes. Coupled with evidence indicating no direct interaction between the photooxidant and Dps, these results support a long-distance protection mechanism for Dps utilizing DNA CT. While Dps is highly upregulated in stationary phase, in exponential phase there are approximately 6000 copies of Dps per *E. coli* cell (*43*). Given the size of the *E. coli* genome (roughly 4,600,000 base pairs), this corresponds to 760 base pairs per Dps, a reasonable distance for DNA CT to occur (*44,45*). We would suggest that in the cell, if there was continued availability of ferrous iron, Dps could funnel electrons from the ferrous iron bound to its ferroxidase sites to guanine radical holes until the oxidized iron core of the protein reached capacity, thereby evincing a potentially greater ability to protect DNA from oxidative damage than the 12 Fe^{2+}/Dps used in this study. This possible DNA-mediated protection mechanism of Dps does not obviate direct oxidation by diffusing oxidants but offers a powerful means whereby Dps could effectively protect DNA from a distance. Such a mechanism could contribute to the oxidative stress resistance and virulence of pathogenic bacteria.

References

1. Zeth, K. Dps biomineralizing proteins: multifunctional architects of nature *Biochem. J.* **2012**, *445*, 297-311.

2. Ceci, P.; Cellai, S.; Falvo, E.; Rivetti, C.; Rossi, G.L.; Chiancone, E. DNA condensation and self-aggregation of *Escherichia coli* Dps are coupled phenomena related to the properties of the N-terminus. *Nucleic Acids Res.* **2004**, *32*, 5935-5944.

3. Altuvia, S.; Almiron, M.; Huisman, G.; Kolter, R.; Storz, G. The *dps* promoter is activated by OxyR during growth and by IHF and σ^S in stationary phase. *Mol. Microbiol.* **1994**, *13*, 265-272.

4. Wolf, S.G.; Frenkiel, D.; Arad, T.; Finkel, S.E.; Kolter, R.; Minsky, A. DNA protection by stress-induced biocrystallization. *Nature* **1999**, *400*, 83-85.

5. Grant, R.A.; Filman, D.J.; Finkel, S.E.; Kolter, R.; Hogle, J.M. The crystal structure of Dps, a ferritin homolog that binds and protects DNA. *Nat. Struct. Biol.* **1998**, *5*, 294-303.

6. Sund, C.J.; Rocha, E.R.; Tzinabos, A.O.; Wells, W.G.; Gee, J.M.; Reott, M.A.; O'Rourke, D.P.; Smith, C.J. The *Bacteroides fragilis* transcriptome response to oxygen and H_2O_2: the role of OxyR and its effect on survival and virulence. *Mol. Microbiol.* **2008**, *67*, 129-142.

7. Li, X.; Pal, U.; Ramamoorthi, N.; Liu, X.; Desrosiers, D.C.; Eggers, C.H.; Anderson, J. F.; Radolf, J.D.; Fikrig, E. The Lyme disease agent *Borrelia burgdorferi* requires BB0690, a Dps homologue, to persist within ticks. *Mol. Microbiol.* **2007**, *63*, 694-710.

8. Satin, B.; Del Giudice, G.; Bianca, V.D.; Dusi, S.; Laudanna, C.; Tonello, F.; Kelleher, D.; Rappuoli, R.; Montecucco, C.; Rossi, F. The neutrophil-activating protein (HP-NAP) of *Helicobacter pylori* is a protective antigen and a major virulence factor. *J. Exp. Med.* **2000**, *191*, 1467-1476.

9. Halsey, T.A.; Vazquez-Torres, A.; Gravdahl, D.J.; Fang, F.C.; Libby, S.J. The ferritin-like Dps protein is required for *Salmonella enterica* serovar Typhimurium oxidative stress resistance and virulence. *Infect. Immun.* **2004**, *72*, 1155-1158.

10. Pang, B.; Hong, W.; Kock, N.D.; Swords, W.E. Dps promotes survival of nontypeable *Haemophilus influenza* in biofilm communities *in vitro* and resistance to clearance *in vivo*. *Front. Cell. Infect. Microbiol.* **2012**, *2*, Article 58.

11. Theoret, J.R.; Cooper, K.K.; Zekarias, B.; Roland, K.L.; Law, B.F.; Curtiss, R. 3rd; Joens, L.A. The *Campylobacter jejuni* Dps homologue is important for *in vitro* biofilm formation and cecal colonization of poultry and may serve as a protective antigen for vaccination. *Clin. Vaccine Immunol.* **2012**, *19*, 1426-1431.

12. Olsen, K.N.; Larsen, M.H.; Gahan, C.G.M.; Kallipolitis, B.; Wolf, X.A.; Rea, R.; Hill, C.; Ingmer, H. The Dps-like protein Fri of *Listeria monocytogenes* promotes stress tolerance and intracellular multiplication in macrophage-like cells. *Microbiology* **2005**, *151*, 925-933.

13. Calhoun, L.M.; Kwon, Y.M. The ferritin-like protein Dps protects *Salmonella enterica* serotype Enteritidis from the Fenton-mediated killing mechanism of bactericidal antibiotics. *Int. J. Antimicrob. Agents* **2011**, *37*, 261-265.

14. Fu, H.-W. *Helicobacter pylori* neutrophil-activating protein: From molecular pathogenesis to clinical applications. *World J. Gastroenterol.* **2014** *20*, 5294-5301.

15. Almiron, M.; Link, A.J.; Furlong, D.; Kolter, R. A novel DNA-binding protein with regulatory and protective roles in starved *Escherichia coli*. *Genes Dev.* **1992**, *6*, 2646-2654.

16. Zhao, G.; Ceci, P.; Ilari, A.; Giangiacomo, L.; Laue, T. M.; Chiancone, E.; Chasteen, N.D. Iron and hydrogen peroxide detoxification properties of DNA-binding protein from starved cells. *J. Biol. Chem.* **2002**, *277*, 27689-27696.

17. Muren, N.B.; Olmon, E.D.; Barton, J.K. Solution, surface, and single molecule platforms for the study of DNA-mediated charge transport. *Phys. Chem. Chem. Phys.* **2012**, *14*, 13754-13771.

18. Genereux, J.C.; Boal, A.K.; Barton, J.K. DNA-mediated charge transport in redox sensing and signaling. *J. Am. Chem. Soc.* **2010**, *132*, 891-905.

19. Sontz, P.A.; Muren, N.B.; Barton, J. K. DNA charge transport for sensing and signaling. *Acc. Chem. Res.* **2012**, *45*, 1792-1800.

20. Chang, I.-J.; Gray, H.B.; Winkler, J.R. High-driving-force electron transfer in metalloproteins: Intramolecular oxidation of ferrocytochrome *c* by $Ru(2,2'\text{-bpy})_2(im)(His\text{-}33)^{3+}$. *J. Am. Chem. Soc.* **1991**, *113*, 7056-7057.

21. Lee, P.E.; Demple, B.; Barton, J.K. DNA-mediated redox signaling for transcriptional activation of SoxR. *Proc. Natl. Acad. Sci. USA* **2009**, *106*, 13164-13168.

22. Yavin, E.; Boal, A.K.; Stemp, E.D.A.; Boon, E.M.; Livingston, A.L.; O'Shea, V.L.; David, S.S.; Barton, J.K. Protein-DNA charge transport: Redox activation of a DNA repair protein by guanine radical. *Proc. Nat. Acad. Sci. USA* **2005**, *102*, 3546-3551.

23. Stemp, E.D.A.; Arkin, M.R.; Barton, J.K. Oxidation of guanine in DNA by $Ru(phen)_2(dppz)^{3+}$ using the flash-quench technique. *J. Am. Chem. Soc.* **1997**, *119*, 2921-2925.

24. Arkin, M.R.; Stemp, E.D.A.; Pulver, S.C.; Barton, J.K. Long-range oxidation of guanine by Ru(III) in duplex DNA. *Chem. Biol.* **1997**, *4*, 389-400.

25. Creutz, C.; Chou, M.; Netzel, T.L.; Okumura, M.; Sutin, N. Lifetimes, spectra, and quenching of the excited States of polypyridine complexes of iron(II), ruthenium(II), and osmium(II). *J. Am. Chem. Soc.* **1980**, *102*, 1309-1319.

26. Delaney, S.; Pascaly, M.; Bhattacharya, P. K.; Han, K.; Barton, J.K. Oxidative damage by ruthenium complexes containing the dipyridophenazine ligand or its derivatives: A focus on intercalation. *Inorg. Chem.* **2002**, *41*, 1966-1974.

27. Fukuzumi, S.; Miyao, H.; Ohkubo, K.; Suenobu, T. Electron-transfer oxidation properties of DNA bases and DNA oligomers. *J. Phys. Chem. A* **2005**, *109*, 3285-3294.

28. Sugiyama, H.; Saito, I. Theoretical studies of GG-specific photocleavage of DNA via electron transfer: Significant lowering of ionization potential and 5′-localization of HOMO of stacked GG bases in B-Form DNA. *J. Am. Chem. Soc.* **1996**, *118*, 7063-7068.

29. Saito, I.; Nakamura, T.; Nakatani, K.; Yoshioka, Y.; Yamaguchi, K.; Sugiyama, H. Mapping of the hot spots for DNA damage by one-electron oxidation: Efficacy of GG doublets and GGG triplets as a trap in long-range hole migration. *J. Am. Chem. Soc.* **1998**, *120*, 12686-12687.

30. Burrows, C.J.; Muller, J.G. Oxidative nucleobase modifications leading to strand scission. *Chem. Rev.* **1998**, *98*, 1109-1151.

31. Wan, C.; Fiebig, T.; Kelley, S.O.; Treadway, C.R.; Barton, J.K.; Zewail, A.H. Femtosecond dynamics of DNA-mediated electron transfer. *Proc. Natl. Acad. Sci. USA* **1999**, *96*, 6014-6019.

32. Anderson P.A.; Deacon, G.B.; Haarmann, K.H.; Keene, F.R.; Meyer, T.J.; Reitsma, D.A.; Skelton, B.W.; Strouse, G.F.; Thomas, N.C.; Treadway, J.A.; White, A.H. Designed synthesis of mononuclear tris(heteroleptic) ruthenium complexes containing bidentate polypyridyl ligands. *Inorg. Chem.* **1995**, *34*, 6145-6157.

33. Martinez, A.; Kolter, R. Protection of DNA during oxidative stress by the nonspecific DNA-binding protein Dps. *J. Bacteriol.* **1997**, *179*, 5188-5194.

34. Bothwell, T.H.; Mallett, B. The determination of iron in plasma or serum. *Biochem J.* **1955**, *59*, 599-602.

35. Ford-Smith, M.H.; Sutin, N. The kinetics of the reactions of substituted 1,10-phenanthroline, 2,2′-dipyridine and 2,2′,2″-tripyridine complexes of iron(III) with iron(II) ions. *J. Am. Chem. Soc.* **1961**, *83*, 1830-1834.

36. Zeglis, B.M.; Barton, J.K. DNA base mismatch detection with bulky rhodium intercalators: Synthesis and applications. *Nat. Protoc.* **2007**, *2*, 357-371.

37. Schwartz, J.K.; Liu, X.S.; Tosha, T.; Diebold, A.; Theil, E.C.; Solomon, E.I. CD and MCD spectroscopic studies of the two Dps miniferritin proteins from *Bacillus anthracis*: Role of O_2 and H_2O_2 substrates in reactivity of the diiron catalytic centers. *Biochemistry* **2010**, *49*, 10516-10525.

38. Su, M.; Cavallo, S.; Stefanini, S.; Chiancone, E.; Chasteen, N.D. The so-called *Listeria innocua* ferritin is a Dps protein. Iron incorporation, detoxification, and DNA protection properties. *Biochemistry* **2005**, *44*, 5572-5578.

39. Kelley, S.O.; Boon, E.M.; Barton, J.K.; Jackson, N.M; Hill, M.G. Single-base mismatch detection based on charge transduction through DNA. *Nucleic Acids Res.* **1999**, *27*, 4830-4837.

40. Boal, A.K.; Barton, J.K. Electrochemical detection of lesions in DNA. *Bioconjugate Chem.* **2005**, *16*, 312-321.

41. Augustyn, K.E.; Merino, E.J.; Barton, J.K. A role for DNA-mediated charge transport in regulating p53: Oxidation of the DNA-bound protein from a distance. *Proc. Natl. Acad. Sci. USA* **2007**, *104*, 18907-18912.

42. Friedman, A.E.; Chambron, J.-C.; Sauvage, J.-P.; Turro, N.J.; Barton, J.K. Molecular "light switch" for DNA $Ru(bpy)_2(dppz)^{2+}$. *J. Am. Chem. Soc.* **1990**, *112*, 4960-4962.

43. Azam, T.A.; Iwata, A.; Nishimura, A.; Ueda, S.; Ishihama, A. Growth phase-dependent variation in protein composition of the *Escherichia coli* nucleoid. *J. Bacteriol.* **1999**, *181*, 6361-6370.

44. Slinker, J.D.; Muren, N.B.; Renfrew, S.E.; Barton, J.K. DNA charge transport over 34 nm. *Nat. Chem.* **2011**, *3*, 228-233.

45. Boal, A.K.; Genereux, J.C.; Sontz, P.A.; Gralnick, J.A.; Newman, D.K.; Barton, J.K. Redox signaling between DNA repair proteins for efficient lesion detection *Proc. Natl. Acad. Sci. USA* **2009**, *106*, 15237-15242.

Chapter 3

Characterization of DNA-bound Dps

3.1 Introduction

Dps proteins are dodecameric (12-mer) bacterial ferritins that protect DNA from oxidative stress, and have been implicated in bacterial survival and virulence (*1*). This protection is thought to derive from ferroxidase activity, wherein Dps proteins simultaneously deplete ferrous iron and hydrogen peroxide, reactive species that can otherwise form damaging hydroxyl radicals via Fenton chemistry (*2*). Like other ferritins, Dps proteins are spherical, with a hollow core where oxidized iron is reversibly stored. Some Dps proteins also nonspecifically bind DNA, such as that from *E. coli* which utilizes N-terminal lysine residues for DNA binding (*3*). Within cells, Dps is upregulated by the transcriptional regulator OxyR in response to oxidative stress (*1*), and is also upregulated in stationary phase, when an additional physical component of Dps protection is biocrystallization with DNA (*4*).

DNA charge transport (CT), wherein both electrons and electron holes are efficiently transported through the base-pair π-stack, can be used biologically by proteins, both as a first step for 4Fe4S cluster-containing DNA repair proteins to localize to the vicinity of a lesion within the vast milieu of the genome, and for the selective activation of redox-active transcription factors from a distance (*5*). In addition to direct interaction with diffusing oxidants, could Dps proteins utilize DNA CT to protect DNA from a distance? Guanine is the most easily oxidized base within the DNA, and the presence of adjacent guanines further lowers the guanine oxidation potential (*6*); thus, radicals are characteristically formed at guanine multiplets upon DNA photooxidation (*7*,*8*). A long distance protection mechanism

via DNA CT would involve electron transfer from Dps through the DNA π-stack to fill the hole on guanine radicals, restoring the integrity of the DNA. In this way, Dps could respond to an oxidative affront to the DNA, even if the protein is bound, at the minimum, a hundred base-pairs away (*9*).

Indeed, we have previously shown that *E. coli* Dps loaded with ferrous iron can protect DNA from oxidative damage created through the flash-quench technique (*10*). The intercalating photooxidant $[Ru(phen)(dppz)(bpy')]^{2+}$, where phen is 1,10-phenanthroline and bpy′ is 4-butyric acid-4′-methyl-2,2′-bipyridine, was covalently tethered the 5′ end of mixed-sequence 70-mer DNA. Upon excitation with visible light ("flash"), the ruthenium(II) excited state can be oxidatively quenched ("quench") by a diffusing quencher, such as $[Co(NH_3)_5Cl]^{2+}$, to form a highly oxidizing intercalated Ru(III) complex (1.6 V versus NHE) (*11*). In the absence of protein, oxidative damage is observed preferentially at a guanine triplet within the 70-mer DNA duplex. Titrating in ferrous iron-loaded Dps significantly attenuates the level of oxidative damage at the guanine triplet, while Apo-Dps and ferric iron-loaded Dps, which lack available reducing equivalents, do not display this protection (*10*). Luminescence experiments rule out direct interaction between the ruthenium photooxidant excited state and Dps, suggesting a DNA-mediated oxidation mechanism. Long-distance, DNA-mediated oxidation of Dps could be an effective mechanism for bacteria to protect their genomes from oxidative insults, perhaps contributing to pathogenic survival and virulence.

The goal of this current work is to spectroscopically characterize the DNA-mediated oxidation of ferrous iron-loaded Dps. Electron paramagnetic resonance (EPR) spectroscopy has previously been used to observe protein oxidation following flash-quench DNA photooxidation. Specifically, EPR studies with MutY, a base excision repair glycosylase with a $[4Fe4S]^{2+}$ cluster as-isolated, compared the homopolymeric DNAs poly(dG-dC) and poly(dA-dT) (*12*). When a sample containing MutY, poly(dG-dC) DNA, $[Ru(phen)_2(dppz)]^{2+}$ and diffusing quencher was irradiated, a mixture of the oxidized $[4Fe4S]^{3+}$ cluster and its decomposition product, $[3Fe4S]^{+}$, was detected with low temperature EPR. When poly(dG-dC) was substituted with poly(dA-dT), a significantly lower intensity EPR signal was observed. Combined with transient absorption experiments, these data directly demonstrated MutY 4Fe4S cluster oxidation by guanine radicals through DNA CT. While MutY can be oxidized to some degree without guanine radical as an intermediate, the thermodynamically favorable oxidation of the MutY $[4Fe4S]^{2+}$ cluster by guanine radical enables more efficient MutY oxidation (*12*).

What type of EPR signal might we expect for Dps? At the inter-subunit ferroxidase sites of Dps, two irons ions are bound by two conserved histidine ligands and two conserved carboxylate ligands, glutamate and aspartate (*1*). This ligand coordination sphere creates two binding sites with very different iron affinities: while one site has a relatively high affinity, the other site binds iron weakly (*13*). After binding, ferrous iron is oxidized and shuttled to the core of the protein for storage. Whereas 24-mer ferritins react rapidly with dioxygen as an oxidant, Dps proteins react slowly with dioxygen and much more quickly with hydrogen

peroxide (*14*). We have previously found that ferricyanide also works well as a chemical oxidant of *E. coli* Dps in solution (*10*). Whereas full occupation of the twelve di-iron centers of the protein would correspond to 24 Fe(II)/Dps, we have found that under the anaerobic conditions used in our experiments (i.e. in the absence of oxidants), *E. coli* Dps binds only 12 Fe(II)/Dps (*10*). This agrees with studies on *Bacillus anthracis* and *Listeria innocua* Dps proteins, where a bridging oxidant seems to be required to tether the lower affinity iron and form the di-iron site (*13*,*15*). Coupled with the specificity of iron binding evidenced by its abrogation in the *E. coli* Dps ferroxidase site double mutant H51G/H63G, the 12 Fe(II)/Dps likely corresponds to binding at the higher affinity iron site of each ferroxidase center in the dodecameric protein. Therefore, in spectroscopic studies with Dps, we would expect to observe the oxidation of mononuclear non-heme iron sites.

Mononuclear high-spin Fe(III) sites of low symmetry (i.e., non-heme) typically display an EPR signal with an apparent *g*-value of 4.3 (*16*,*17*). The ground state of the high-spin d^5 Fe(III) $S = 5/2$ species is split into three Kramer's doublets according to the zero field splitting parameters D and E. In purely rhombic cases, the distortion parameter E/D is equal to 1/3, and the doublets are equally spaced. At low magnetic fields, the spin states mix and the $\Delta M_s = \pm 1$ selection rule no longer holds, allowing for transitions within, rather than between, the Kramer's doublets. The transition within the middle pair of Kramer's doublets ($M_s = \pm 3/2$) produces an isotropic signal at $g = 4.29$. Because of its isotropic nature, this transition produces a strong signal that is easily observed.

This mononuclear high-spin Fe(III) signal at $g = 4.3$ has been frequently reported in the EPR spectra of 24-mer ferritins. For instance, the EPR spectra of horse spleen ferritin oxidized by dioxygen has been described after rapid mixing of aerobic ferritin with an anaerobic solution of ferrous iron (*18*). After varying reaction times, the sample was freeze-quenched and measured at 7.2 K. EPR experiments with iron must typically must be performed at low temperature because of their rapid spin-lattice relaxation. In the early stages of ferrous iron oxidation, mononuclear Fe^{3+}-apoferritin with $g = 4.3$ is formed quantitatively. This signal is followed by the appearance of a mixed-valent Fe^{2+}-Fe^{3+} species with $g = 1.87$, derived from the mononuclear ferric iron sites within the first second of reaction. At later times, as the oxidized iron translocates to the core of the protein, polynuclear EPR-silent Fe^{3+} species are formed (*18*).

Conversely, the EPR spectra of iron-bound Dps proteins have not been previously reported. *Sulfolobus solfataricus* Dps selectively binds two Mn^{2+} as evidenced by EPR titrations (*19*). Spin trapping experiments have been performed with Dps proteins that measure the EPR-active adduct of hydroxyl radical with EMPO (5-ethoxycarbonyl-5-methyl-pyrroline-N-oxide). The presence of both *E. coli* and *Listeria innocua* Dps proteins have been shown to attenuate formation of the EMPO-OH adduct resulting from reaction of ferrous iron and hydrogen peroxide (*13*,*14*).

Here, we use X-band EPR to observe the oxidation of DNA-bound *E. coli* Dps loaded with 12 Fe(II)/Dps. Using the flash-quench technique with non-covalent racemic $[Ru(phen)(dppz)(bpy')]^{2+}$ and the diffusing quencher $[Co(NH_3)_5Cl]^{2+}$, we compare the

alternating copolymers poly(dGdC)$_2$ and poly(dAdT)$_2$ in order to investigate if guanine radical is an important intermediate in Dps oxidation. Thus our goals are to spectroscopically confirm the oxidation of ferrous iron-loaded Dps following DNA photooxidation, and investigate the DNA-mediated characteristics of this oxidation.

We also seek to explore possible electron transfer intermediates in the DNA-mediated oxidation of ferrous iron-loaded Dps. There is a highly conserved tryptophan residue in close proximity (approximately 5 Å) to the ferroxidase site in Dps proteins (Figure 1), W52 in *E. coli*. Because of the location of this aromatic tryptophan residue between the ferroxidase site and the outer protein shell, it is an attractive candidate as a hopping intermediate to facilitate electron transfer between the ferroxidase site of Dps and DNA. While the molecular characteristics of DNA binding are unknown, one proposal suggests that *D. radiodurans* Dps uses its N-terminal extensions to bind to consecutive DNA major grooves along the dimer interface of the dodecamer where the ferroxidase sites are located (*20*). Although *D. radiodurans* Dps has exceptionally long N-terminal extensions that bind Co^{2+}, *E. coli* Dps also has an N-terminal extension that contains three lysine residues as well as an arginine residue. An arginine residue protruding from center helix of *D. radiodurans* Dps (Arg132) is also implicated in DNA binding; in *E. coli*, there is a lysine residue in this position (Lys101). Thus this general DNA-binding mechanism may be conserved from *D. radiodurans* to *E. coli* Dps; if so, W52 would be ideally situated as an electron transfer hopping intermediate. Moreover, this work finds no evidence for DNA wrapping around an individual Dps dodecamer (*20*). As well as the conserved tryptophan residue in Dps

proteins, in 24-mer ferritins there is a conserved tyrosine residue in close proximity to the intrasubunit ferroxidase site.

Previous work has suggested important roles for these conserved aromatic residues in ferritins (*21-24*). Upon oxidation with hydrogen peroxide of Dps loaded with only 6 Fe(II)/Dps, UV-visible stopped flow experiments with *E. coli* Dps were able to observe spectra with maxima at 512 and 536 nm, consistent with a neutral tryptophan radical (*21*). Maximal intensity was reached after 50 ms, and the radical displayed a lifetime of approximately 1700 ms. *L. innocua* Dps proteins additionally contain a tyrosine residue (Y50) approximately 8 Å from the conserved tryptophan residue near the ferroxidase site (W32 in *L. innocua* numbering). Site-directed mutagenesis studies with *L. innocua* Dps were able to confirm the identity of the radicals: Y50R Dps exhibited only tryptophan radical spectra, W32L Dps exhibited only tyrosine radical spectra, and the Y50R/W32L double mutant displayed neither spectra. By comparison with these *L. innocua* Dps results, Bellapadrona *et al.* were able to ascribe the tryptophan radical in *E. coli* to W52 (*21*). Interestingly, the ability of the WT and mutant *L. innocua* Dps to protect plasmid DNA from degradation by ferrous iron and hydrogen peroxide was investigated. Whereas the single W32L mutation did not inhibit the protection capacity of *L. innocua* Dps and the Y50R mutation inhibited this protection only slightly, in the double mutant, Y50R/W32L, the protective capacity of *L. innocua* Dps was significantly attenuated. Bellapadrona *et al.* concluded that these conserved aromatic residues act as a trap for electron holes generated by the oxidation of insufficient ferrous iron by hydrogen peroxide (*21*). That is, the reduction

of hydrogen peroxide to water is a two electron process, but this study was conducted under iron loading conditions where the high affinity iron site is only partially occupied, precluding formation of the di-iron site that would provide two electrons. Thus these aromatic residues seem to provide the extra electron that may otherwise be abstracted from DNA, resulting in oxidative damage (*21*).

In 24-mer ferritins, a tyrosine radical has been observed with EPR upon aerobic incubation of the Apo-protein with ferrous iron in human H-chain ferritin (*22*,*23*), horse spleen ferritin (*18*), *E. coli* bacterial ferritin (24-mer) (*24*), and archaeal *Pyrococcus furiosus* ferritin (*23*). This radical has been ascribed to the conserved tyrosine residue near the ferroxidase site by site-directed mutagenesis studies (*22*,*24*). A study on human H-chain ferritin and *P. furiosus* ferritin proposed a universal mechanism for 24-mer ferritins, wherein the conserved tyrosine residue acts as a molecular capacitor, facilitating oxidation of ferrous iron at the ferroxidase sites by providing an extra electron for the reduction of dioxygen to water (*23*). When this tyrosine residue was mutated to phenylalanine in both proteins, key intermediates in iron oxidation (μ-peroxo-diferric intermediate) were absent and the rate of ferrous iron oxidation at the ferroxidase sites was significantly decreased (*23*). This proposal for tyrosine as a molecular capacitor in 24-mer ferritins is similar to the role proposed for W52 in *E. coli* Dps (*21*). However, other studies with 24-mer ferritins contend with a universal mechanism (*24*). Experiments with *E. coli* bacterial ferritin find that a tyrosine to phenylalanine mutant is able to form the μ-peroxo-diferric intermediate similarly to the WT protein, but that oxidation is slowed upon further addition of ferrous iron to the protein

(*24*). These researchers therefore suggest a possible redox or structural role for the conserved tyrosine residue in the assembly of the oxidized iron core. Overall, it is clear that the conserved aromatic residue in close proximity to the ferroxidase site may play an important role in ferritins.

Here, we investigate two *E. coli* Dps W52 mutants: W52Y, where an aromatic residue is maintained at this position, and W52A, which abolishes the aromatic residue adjacent to the ferroxidase site. We compare these mutants with the WT protein in EPR studies of the oxidation of ferrous iron-loaded Dps following DNA photooxidation. Because the intercalating ruthenium photooxidant is a one-electron oxidant, sending one electron hole at a time into the DNA π-stack, we will be examining the role of *E. coli* Dps W52 as an electron transfer hopping intermediate rather than a molecular capacitor. In addition to EPR, we also probe the role of W52 Dps in cells using a hydrogen peroxide survival assay. Previously, in a *dps* knockout *E. coli* strain (*dps*::*kan* Δ*recA* Δ*ara*), it was demonstrated that induction of WT Dps on a plasmid before exposure to hydrogen peroxide significantly increased bacterial survival compared to un-induced cells (*25*). Additionally, Dps specifically prevents guanine oxidation *in vivo*. Upon treatment with hydrogen peroxide, a CC104 *dps*::*kan* knockout strain displayed a 10-fold increase in GC to TA transversion mutations, caused by 8-oxoG:A mismatches, compared to the strain with WT *dps* (*25*). No increase in mutation frequency was observed for any of the other six possible base substitutions. Furthermore, WT Dps expression from an inducible plasmid was able to partially rescue the number of revertant-causing mutations in CC104 strains with *mutY* and *mutM* knockouts,

which encode DNA glycosylase enzymes (*25*). MutM recognizes 8-oxoG:C pairs and excises the 8-oxoG, while MutY removes adenine from 8-oxoG:A mismatches (*26*). Given these intriguing results, the role of Dps proteins, particularly with regard to a long-distance DNA-mediated protection mechanism, should be further explored *in vivo*.

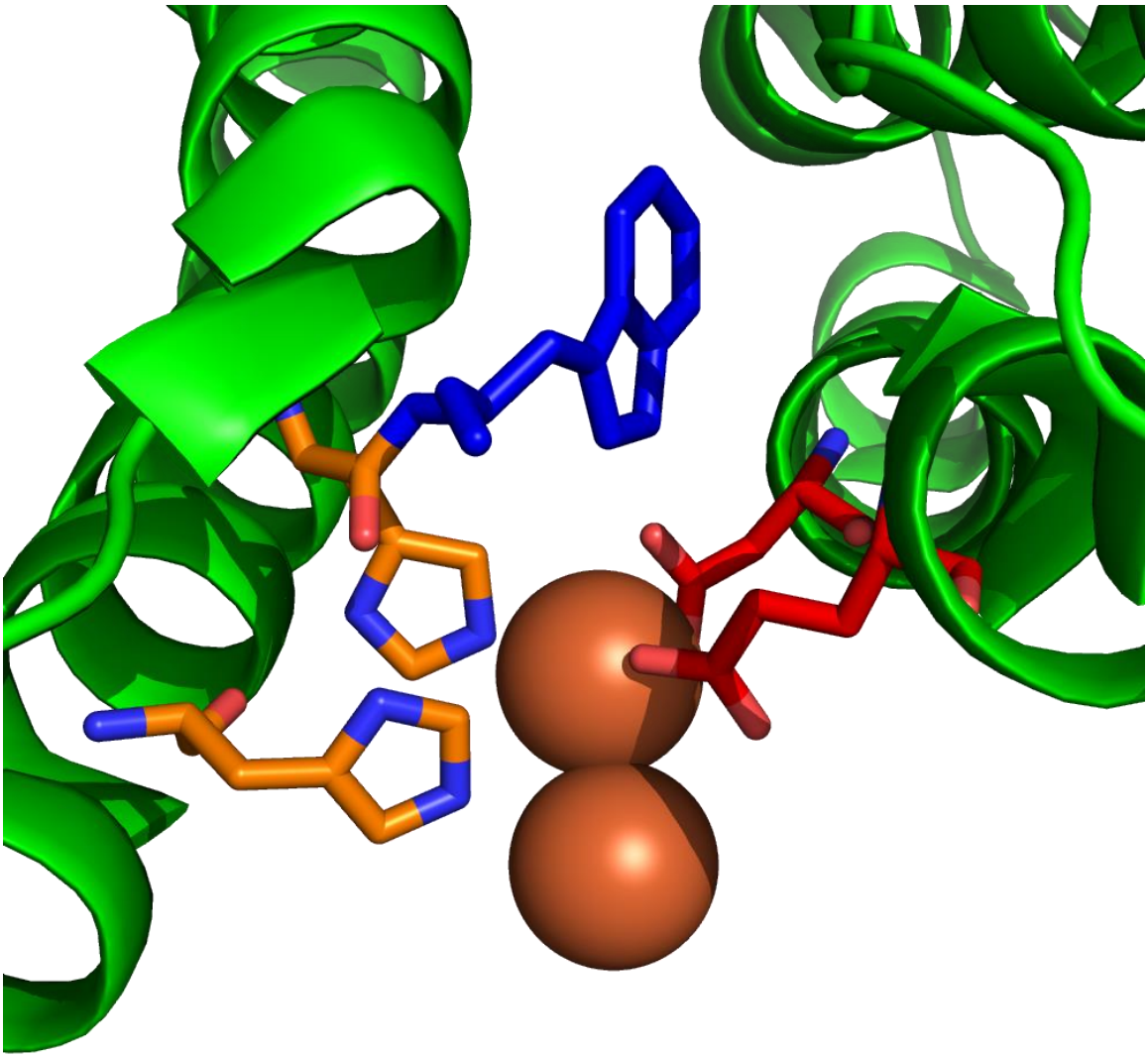

Figure 1. Crystal structure illustrating conserved residues of the ferroxidase site in Dps proteins. The iron ligands are shown in orange (histidines) and red (carboxylates); the conserved tryptophan residue in close proximity to the ferroxidase site is shown in blue. The *E. coli* protein has not been crystallized with bound iron; *Bacillus brevis* Dps shown (PDB: 1N1Q; reference: Ren, B. et al. *J. Mol. Biol.* **2003**, *329*, 467-477).

3.2 Experimental section

3.2.1 W52 mutagenesis

The W52A and W52Y *E. coli* Dps mutants were made with a Quikchange II-E Site-Directed Mutagenesis Kit (Stratagene) using the pBAD18-dps plasmid (containing the WT *E. coli* dps gene and an ampicillin resistance cassette) donated by Dr. Roberto Kolter (*25*) as a template. Primers were purchased from Integrated DNA Technologies. All mutagenized plasmids were sequenced (Laragen) to confirm the desired sequences. After successfully creating the mutant pBAD18-dps plasmids, the *E. coli* cell line ZK2471 (*dps*::*kan* Δ*recA* Δ*ara*) donated by Dr. Roberto Kolter was made electrocompetent and the plasmid was transformed via electroporation into these cells. Primer sequences were as follows, with mutagenized codon underlined:

W52A-forward: 5′-GATCTTTCTTTGATTACCAAACAAGCGCACGCGAACATGC-3′

W52A-reverse: 5′-GCATGTTCGCGTGCGCTTGTTTGGTAATCAAAGAAAGATC-3′

W52Y-forward: 5′-CAGTTTATTGATCTTTCTTTGATTACCAAACAAGCGCACTAC AACATGC-3′

W52Y-reverse: 5′- GCATGTTGTAGTGCGCTTGTTTGGTAATCAAAGAAAGATCAA TAAACTG-3′

3.2.2 CD of WT and mutants

Protein concentrations were determined using ε_{280} values calculated using the ExPASy ProtPram tool (http://web.expasy.org/protparam/). The calculated molar absorptivity values for WT, W52A and W52Y *E. coli* Dps dodecamers were ε_{280} = 185,640

$M^{-1}cm^{-1}$, 119,640 $M^{-1}cm^{-1}$, and 137,520 $M^{-1}cm^{-1}$, respectively. Spectra were recorded at 25°C on a Model 430 circular dichroism spectrometer (AVIV) in a buffer consisting of 50 mM Tris, pH 7.0, 150 mM NaCl. The spectra shown are the average of three individual scans, with a buffer alone spectrum subtracted.

3.2.3 Materials

The alternating co-polymer DNA duplexes poly(dGdC)$_2$ and poly(dAdT)$_2$ were purchased from Sigma. The DNA duplexes were passed through Bio-rad spin columns (6 K MWCO) before use and quantified based on their molar absorptivity values in terms of base-pairs (*27*), (poly(dGdC)$_2$: ε_{254} = 16,800 M^{-1} cm^{-1}, poly(dAdT)$_2$: ε_{262} = 13,200 M^{-1} cm^{-1}). Duplexes were then dried on a speed-vac, brought into an anaerobic chamber (Coy), and re-suspended in deoxygenated buffer.

$[Ru(phen)(dppz)(bpy')]^{2+}$ was synthesized according to published methods (*28*), purified by reversed-phase chromatography, and characterized by NMR and ESI mass spectrometry (expected for the +2 ion: 409.62 m/z, observed: 410.2 m/z). The ruthenium photooxidant was brought into the anaerobic chamber as a solid powder, re-suspended with deoxygenated buffer, and a sample removed for quantification based on UV-Vis absorption (ε_{440} = 21,000 M^{-1} cm^{-1}). $[Co(NH_3)_5Cl]Cl_2$ was purchased from Sigma (99.995% pure) and used as received. The Co quencher was brought into the anaerobic chamber as a solid powder, re-suspended with deoxygenated buffer, and a sample removed for quantification based on UV-Vis (ε_{550} = 47.5 M^{-1} cm^{-1}).

WT and W52 mutant *E. coli* Dps proteins were purified according to previous procedures (*10*). Proteins were deoxygenated in Schlenck tubes according to previous procedures (*10*), and brought into the anaerobic chamber. Proteins were then anaerobically loaded with ferrous iron also according to previous procedures (*10*). Buffers (50 mM Tris or 50 mM MOPS, pH 7.0, 150 mM NaCl, 5% glycerol) were deoxygenated in a Schlenk flask by at least 4 cycles of freeze-pump-thaw.

3.2.4 EPR sample preparation

EPR samples were prepared in an anaerobic chamber (Coy) using the anaerobic materials outlined above. Samples were loaded into EPR tubes within the anaerobic chamber, sealed with septa, and parafilmed around the septa seal. EPR tubes were then brought out of the anaerobic chamber, frozen in liquid nitrogen, and kept in the dark until measurement. Precipitated samples were thoroughly mixed before freezing in liquid nitrogen. For chemically oxidized samples, ferrous iron-loaded protein (approximately 120 μL) was added to the bottom of an EPR tube. Approximately 20 μL of ferricyanide solution was added to the top of the EPR tube, which was then sealed. Upon removal from the anaerobic chamber, the solutions were mixed together and immediately froze in liquid nitrogen within approximately 5-10 seconds of the initiation of mixing.

3.2.5 EPR experiments

EPR spectra were measured on an X-band Bruker EMX spectrometer equipped with an ER4119HS resonator and an Oxford ES9000 cryostat. Instrumental settings are detailed in figure captions, but were generally as follows: modulation amplitude = 10 G at 100 kHz,

frequency = 9.37 GHz, microwave power = 6.4 mW, temperature = 10 K. Samples in Suprasil quartz EPR tubes were irradiated while freezing in liquid nitrogen in an unsilvered Dewar. The excitation source was a xenon lamp equipped with a lens to focus the beam and a 320 nm long-pass filter to remove UV light. Each sample was irradiated for a total of approximately 10 seconds. For each sample, a dark control EPR spectrum was first measured at 10 K. The sample was then thawed, mixed, and irradiated while freezing with liquid nitrogen as described. The EPR spectrum of the irradiated sample was then measured under identical instrumental settings. For data analysis, the dark control spectrum was smoothed and subtracted from the irradiated sample.

3.2.6 Hydrogen peroxide survival experiments

This protocol is adapted from that reported by Martinez and Kolter (*25*). Hydrogen peroxide was purchased from Macron (30% solution) and confirmed to be 10.8 M by $KMnO_4$ titration (*29*). Lyophilized catalase from bovine liver (≥ 20000 units/mg protein) was purchased from Sigma and re-suspended in buffer (50 mM KPO_4, pH 7) to make a stock concentration of 0.4 mg/mL. Overnight cultures of the *E. coli* ZK2471 strain (*dps*::*kan* Δ*recA* Δ*ara*) containing WT, W52A, or W52Y pBAD18-*dps* plasmids were prepared by inoculating single colonies in 5 mL of LB media containing 100 μg/mL ampicillin and 50 μg/mL kanamycin. After overnight shaking at 37°C, the cultures were diluted 1:500 into 50 mL of fresh LB media also containing antibiotics. For each WT, W52A, and W52Y, both induced and un-induced 50 mL cultures were prepared: L-arabinose was added to induce Dps overexpression (0.2% w/v final concentration), and an equivalent volume of sterile

water was added to un-induced cells. Cultures were then incubated at 37°C with shaking (200 rpm) for 3 hours until OD_{600} = 0.3-0.4 (exponential phase). Next, cultures were poured into sterile trays and aliquoted with a multichannel pipette into a sterile 96-well plate (one culture type per row, 200 µL per well, 8 wells in each row). A second 96-well plate was prepared with a row of increasing hydrogen peroxide stock solutions. Hydrogen peroxide solutions were then added with a multichannel pipette (10 µL) and mixed by pipetting. After 15 minutes at RT, catalase solution was added to stop the reaction using a multichannel pipette (5 µL, working concentration: 10 µg/mL culture) and mixed by pipetting. Cultures were incubated for 15 minutes after catalase addition to ensure complete hydrogen peroxide reaction. Cultures were then serially diluted into minimal M63 media for a total of 12,800-fold dilution. Finally, cultures were plated (30 µL) onto LB agar plates containing ampicillin and kanamycin and incubated at 37°C overnight. The number of colonies on each plate were manually counted the subsequent day.

3.3 Results and Discussion

3.3.1 Structure and Fe binding of W52 Dps mutants

The Dps monomer is composed of a four helix bundle with two helix-turn-helix motifs (*30*). The far-UV circular dichroism (CD) spectra of WT Apo-Dps is consistent with this α-helical structure (Figure 2) (*31*). Comparison of the WT with W52A and W52Y Dps CD spectra shows that overall protein folding is relatively unaffected by these mutations. Next, iron binding at the ferroxidase site was investigated for both mutations. As previously described for WT Dps (*10*), the proteins were incubated anaerobically with excess ferrous iron and unbound iron was subsequently removed with size exclusion chromatography. The number of irons bound per Dps dodecamer was then quantified by the formation of $[Fe(bpy)_3]^{2+}$ after protein denaturation and addition of reductant and 2,2′-bipyridine. When Dps concentration is measured via the Bradford reagent or calculated ε_{280} values, the Fe(II)/Dps can be quantified. In one trial, the WT protein bound 14.6 ± 0.5 Fe(II)/Dps, whereas the W52A and W52Y mutants bound only 8.6 ± 0.4 and 10.6 ± 0.4 Fe(II)/Dps, respectively. Similar results were obtained in other trials. Note that small increases from 12 Fe(II)/Dps in the WT protein are likely due to a minor degree of oxidation due to trace oxygen, allowing for some di-iron site formation. Figure 3 shows the $[Fe(bpy)_3]^{2+}$ spectra normalized to protein concentration for WT, W52A, and W52Y Dps. W52A Dps binds iron on the order of 60% of WT, while W52Y is slightly better, binding 70% of the iron of WT Dps. Thus iron binding is somewhat attenuated, but not abrogated, for these mutations.

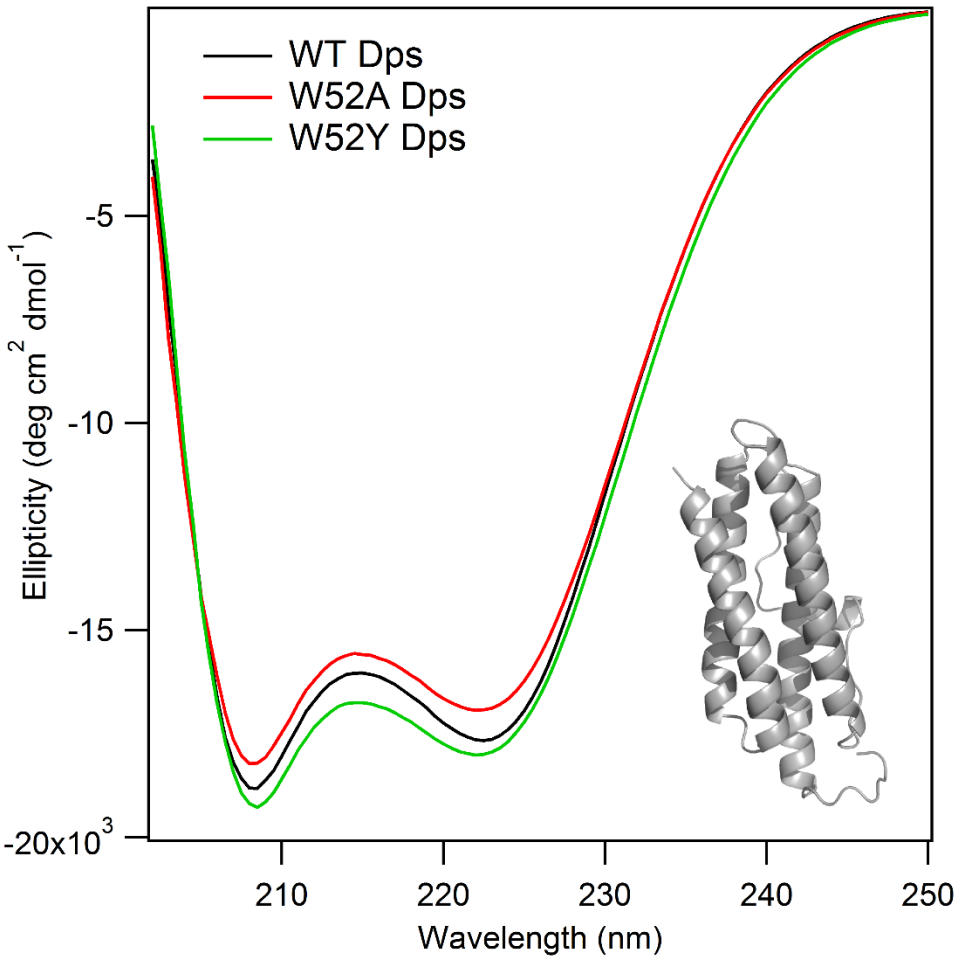

Figure 2. Circular dichroism spectra of wild-type (WT) (black), W52A (red), and W52Y (green) *E. coli* Apo-Dps. Dps monomer depicted in gray, showing α-helical structure. Protein concentration was 5 μM in a buffer of 50 mM Tris, pH 7.0, 150 mM NaCl.

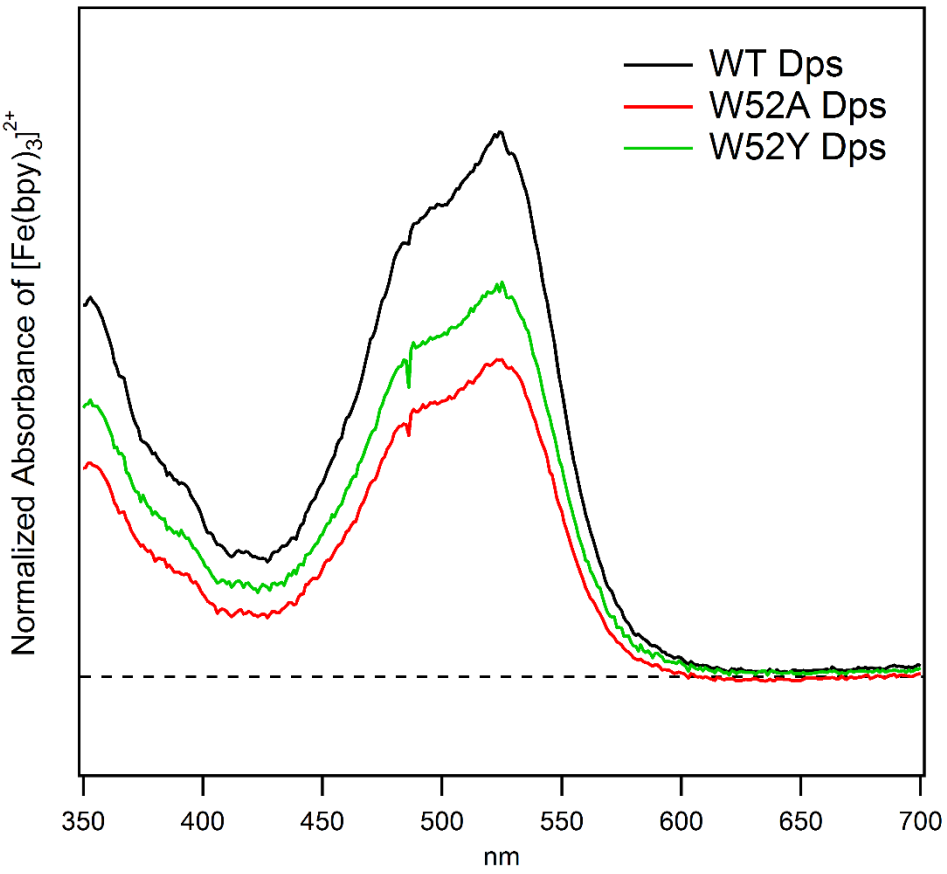

Figure 3. Ferrous iron loading of Dps W52 mutants compared to WT *E. coli* protein. Normalized UV-Visible spectra of $[Fe(bpy)_3]^{2+}$ produced from either WT Dps (black), W52A Dps (red), or W52Y Dps (green). For normalization, the absorbance values were divided by protein concentration. The calculated number of iron atoms per Dps dodecamer is 14.6 ± 0.5 for WT Dps, 8.6 ± 0.4 for W52A, and 10.6 ± 0.4 for W52Y. Protein concentrations were determined by A_{280} using calculated ε_{280} values (185,640 $M^{-1}cm^{-1}$ for WT, 119,640 $M^{-1}cm^{-1}$ for W52A, and 137,520 $M^{-1}cm^{-1}$ for W52Y); the concentration of $[Fe(bpy)_3]^{2+}$ was determined by A_{522} using a derived extinction coefficient of 8,790 $M^{-1}cm^{-1}$.

3.3.2 EPR results with WT *E. coli* Dps

Because the EPR spectrum of iron-bound Dps proteins has not been previously reported, we first used chemical oxidation to confirm the Dps oxidation products to expect in flash-quench studies. All EPR samples described in this study were prepared anaerobically in an anaerobic chamber in order to prevent dioxygen oxidation of ferrous iron loaded Dps. Samples were loaded into EPR tubes and sealed with septa before removal from the anaerobic chamber. As expected, Apo-Dps, which has not been loaded with iron, and Dps loaded with ferrous iron are EPR-silent (Figure 4). However, when WT Dps loaded with 12 Fe(II)/Dps is mixed anaerobically with stoichiometric ferricyanide and frozen in liquid nitrogen within 5-10 seconds, a split signal at g = 4.3 is observed at low temperature (10 K) (Figure 4). Given that ferricyanide has a different g-value and ferrocyanide is EPR-silent, and that the steady-state UV-Visible spectrum of ferrous iron-loaded Dps incubated with ferricyanide indicates the formation of oxidized iron species (*10*), this signal at g = 4.3 can be ascribed to oxidized ferric iron at the mononuclear ferroxidase site in Dps.

As described above, this is the expected EPR signal for mononuclear, non-heme, high-spin Fe(III) sites of low symmetry (*16*,*17*), and has previously been observed in EPR studies in 24-mer ferritins (*18*). No other EPR-active species are apparent in wide spectra from 500 to 4500 gauss. When instead the ferrous iron-loaded Dps was incubated with ferricyanide for much longer times, no EPR-active species were observed (data not shown), likely because the oxidized iron was translated to the core of the protein, forming EPR-silent polynuclear species.

Next, we investigated the oxidation of DNA-bound WT *E. coli* Dps via the flash-quench technique. Here, the sample is irradiated in an EPR tube while freezing in liquid nitrogen in a clear dewar in order to trap reactive intermediates. Under the conditions used in these experiments, all samples containing both Dps and DNA precipitated, consistent with earlier studies on *E. coli* Dps (*3*). For each sample, an individual dark control (DC) was measured at low temperature (10 K). The sample was then thawed, mixed, and irradiated while freezing to generate oxidative DNA damage via the flash-quench technique. Efforts were made to irradiate all samples under identical conditions for 10 seconds. The EPR spectrum of the irradiated sample was then re-measured under identical instrument settings. All spectra shown in Figure 5 have had an individual DC subtracted; thus, all features are a function of irradiation.

In a sample containing 20 μM Dps loaded with 12 Fe(II)/Dps, poly(dGdC)$_2$ at a concentration of 1 mM base-pairs, 20 μM non-covalent [Ru(phen)(dppz)(bpy′)]$^{2+}$ and 120 μM [Co(NH$_3$)$_5$Cl]$^{2+}$ in a buffer of 50 mM Tris, pH 7.0, 150 mM NaCl, 5% glycerol, a split nearly isotropic signal at g = 4.3 is observed upon irradiation (Figure 5). Comparison with the chemically oxidized sample indicates that this species corresponds to oxidized ferric iron at the mononuclear ferroxidase site in Dps. In contrast, no signal was observed in a sample lacking DNA (Minus DNA) and an attenuated signal was observed in an irradiated sample that contained ferrous iron-loaded Dps, poly(dGdC)$_2$, and [Ru(phen)(dppz)(bpy′)]$^{2+}$ but lacked quencher (Light control). Some signal was observed in the Light control sample, even though steady-state room temperature luminescence experiments with mixed-sequence 70-

mer duplex DNA containing covalently tethered $[Ru(phen)(dppz)(bpy')]^{2+}$ indicated that Dps does not quench the ruthenium(II) excited state (*10*). When Apo-Dps is substituted for Dps loaded with ferrous iron, no signal at $g = 4.3$ is observed, confirming protein-bound iron as the origin of this signal. Importantly, when $poly(dAdT)_2$ is substituted for $poly(dGdC)_2$, the observed signal is significantly attenuated, suggesting that guanine radical plays a role in Dps oxidation. When the dark control subtracted spectra are quantified by double integration over the range of 1400 to 1700 gauss, the signal is attenuated with $poly(dAdT)_2$ by 3-fold. Overall, similar results were obtained in four separate trials.

The wide EPR spectrum of the $poly(dGdC)_2$ with ferrous iron-loaded Dps sample from 500 to 4500 gauss shows that the only features evident upon irradiation are the $g = 4.3$ feature previously discussed and a small signal at $g = 2$ (Figure 6). The $g = 2$ signal is likely an organic radical, either guanine radical or tryptophan radical; however, we were unable to obtain reproducible results at $g = 2$. Despite investigating different temperatures and microwave powers to prevent power saturation, signals at $g = 2$ were too small for conclusions to be drawn. While the tryptophan radical (W52) has been previously observed in *E. coli* Dps with UV-Visible stopped flow experiments (*21*), it is unclear whether we have both the time resolution and sufficient yields to observe this radical with EPR.

In Tris buffer, there is a signal at $g = 4.3$ when a sample of ferrous iron only is mixed with ferricyanide (Figure 7). Therefore, it is important to control for oxidized iron remaining bound to Dps. One approach is to compare samples prepared in a MOPS buffer. In MOPS buffer, no signal is observed when a sample of ferrous iron only is mixed with

ferricyanide (Figure 8). However, a small, un-split signal is apparent at $g = 4.3$ in a sample of ferrous iron-loaded Dps, poly(dGdC)$_2$ DNA, ruthenium complex and diffusing quencher upon irradiation. While the significantly smaller signals in MOPS buffer makes comparisons between samples (i.e., different DNAs) difficult, this MOPS result suggests that at least some of the iron in Tris samples remains bound to the protein after oxidation.

Therefore, in these experiments we have used EPR to spectroscopically confirm the oxidation of WT ferrous iron-loaded *E. coli* Dps following DNA photooxidation with the flash-quench technique. Because Dps is loaded with one ferrous iron per ferroxidase site, this oxidation is evidenced by the appearance of mononuclear ferric iron species of low symmetry at an apparent *g*-value of 4.3. This signal is absent in a Minus DNA control, and attenuated in a Light control which lacks the diffusing quencher necessary for flash-quench. Additionally, guanine radical seems to facilitate Dps oxidation. When poly(dGdC)$_2$ is substituted with poly(dAdT)$_2$ DNA, the yield of Dps oxidation is decreased significantly. Back electron transfer (BET) processes continually decrease the observed yield of oxidized protein in the flash-quench technique. Adenine radicals would be expected to have short lifetimes compared to the neutral guanine radical, which persists for milliseconds (*11*). Thus, similarly to what was postulated with MutY (*12*), it appears likely that guanine radical formation allows more time for the oxidation of Dps by better competing with rapid BET to the intercalated ruthenium(III) photooxidant, resulting in higher yields of Dps oxidation with guanine radical as an intermediate. Additionally, poorly stacked ATAT tracts do not conduct charge efficiently (*32*); this may also be a factor in the lower yield of protein

oxidation with poly(dAdT)$_2$ DNA. Generally, the more favorable oxidation of Dps by guanine radicals also supports the feasibly of a sequential process, according to our hypothesis of DNA-mediated CT, where after guanine radicals are produced, Dps is oxidized to fill guanine radical holes.

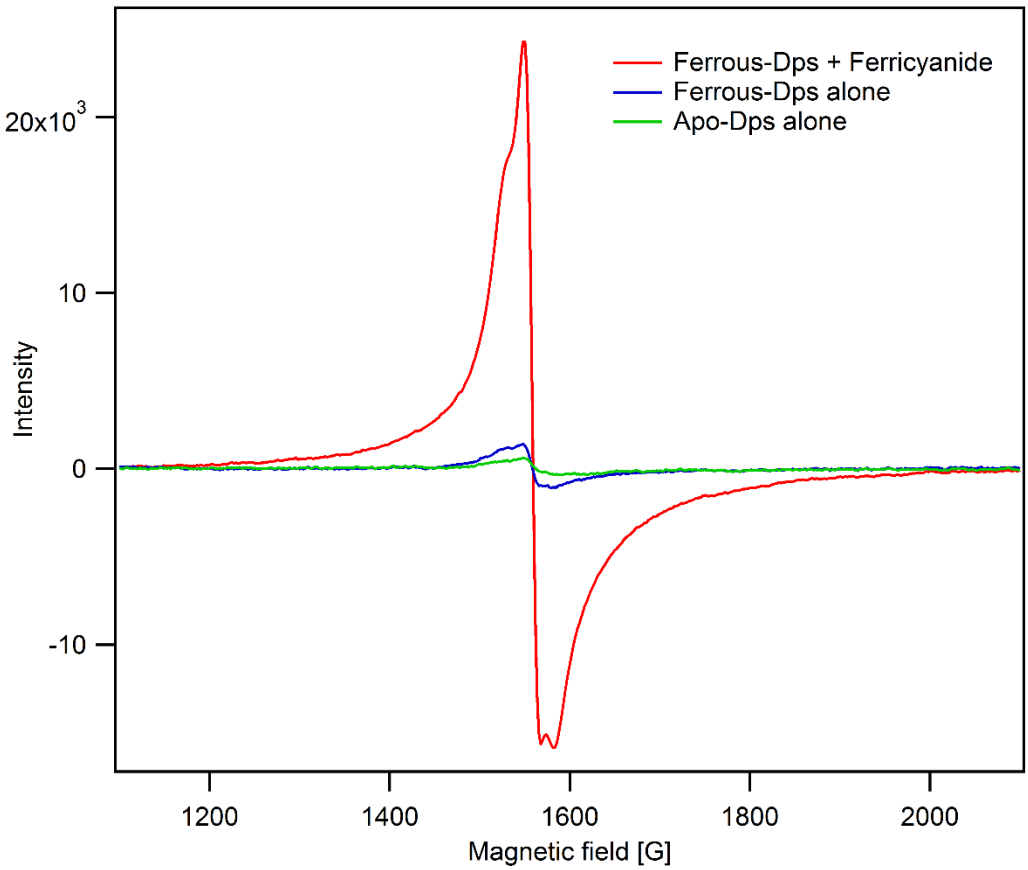

Figure 4. Chemical oxidation of WT *E. coli* Dps containing 12 Fe(II)/Dps with stoichiometric ferricyanide. Conditions: Dps concentration: 20 μM; Actual Fe/Dps: 11.9 ± 0.2; Buffer: 50 mM Tris, pH 7, 150 mM NaCl, 5% glycerol. Instrument settings: modulation amplitude = 10 G at 100 kHz; frequency = 9.373 GHz; microwave power = 6.4 mW; temperature = 10 K. All spectra have had a buffer blank subtracted.

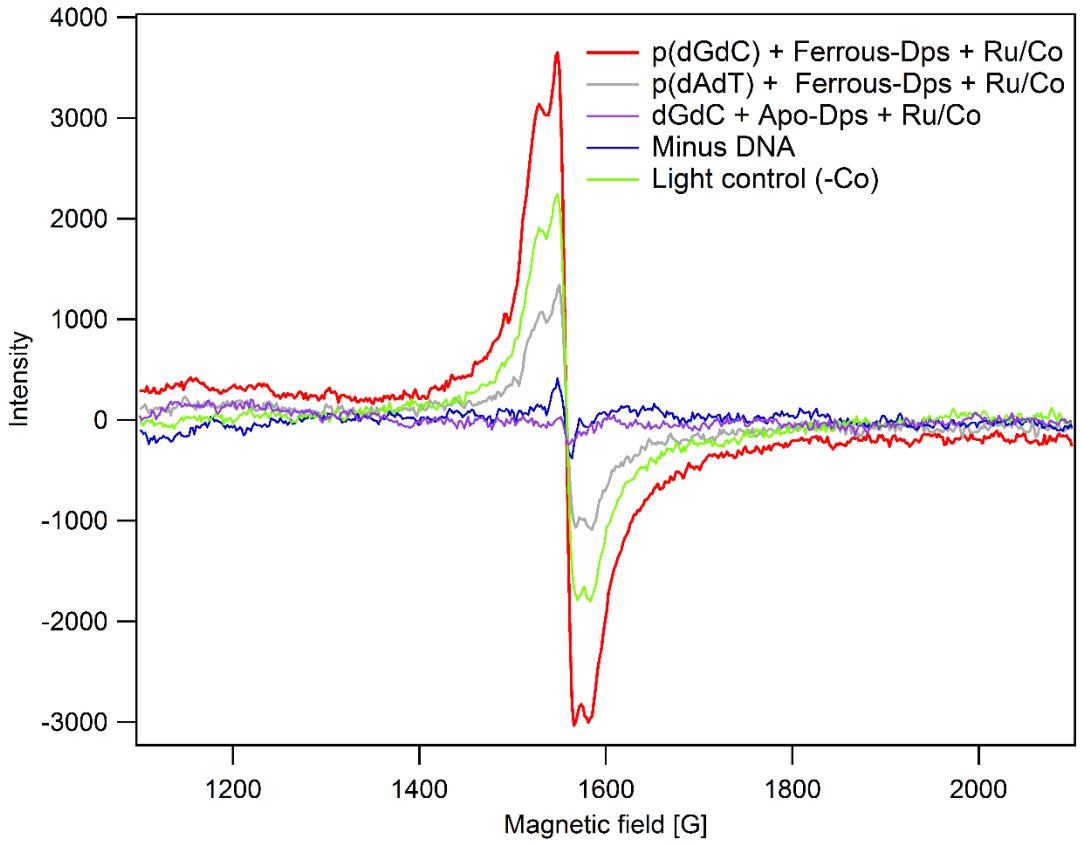

Figure 5. DNA-bound WT *E. coli* Dps oxidation via the flash-quench technique. All spectra have had an individual un-irradiated spectrum subtracted; thus all features are a function of irradiation. Concentrations: 20 μM Dps (Fe^{2+}/Dps: 11.9 ± 0.2), 1 mM base-pairs poly(dGdC)$_2$ or poly(dAdT)$_2$ DNA, 20 μM $[Ru(phen)(dppz)(bpy')]^{2+}$, 120 μM $[Co(NH_3)_5Cl]^{2+}$. Buffer: 50 mM Tris, pH 7.0, 150 mM NaCl, 5% glycerol. Minus DNA sample contains ferrous iron-loaded Dps, Ru, and Co, but lacks DNA; Light control contains ferrous iron-loaded Dps, poly(dGdC)$_2$ DNA, and Ru, but lacks Co quencher. Instrument settings: modulation amplitude = 10 G at 100 kHz; frequency = 9.37 GHz; microwave power = 6.4 mW; temperature = 10 K.

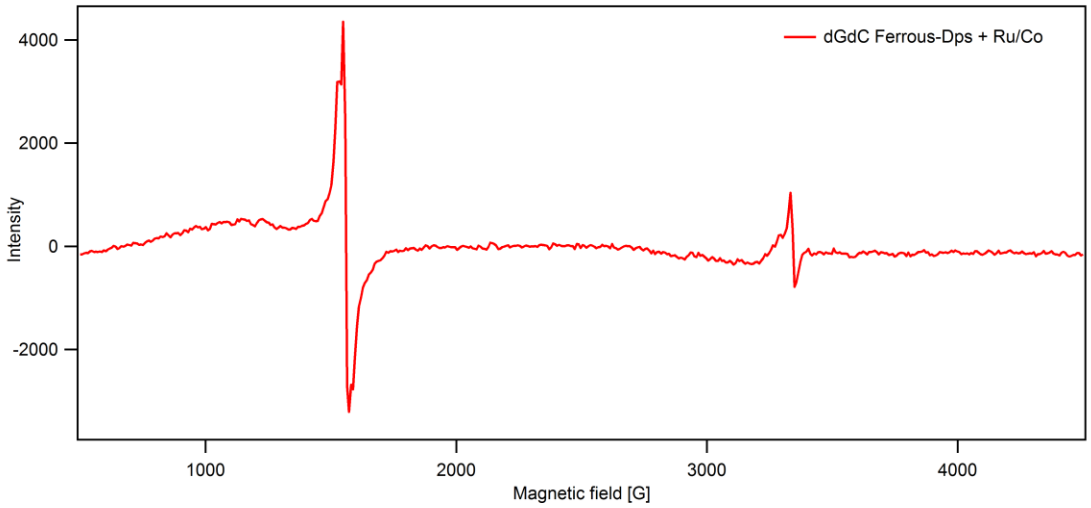

Figure 6. Wide EPR spectra of irradiated sample containing WT ferrous iron-loaded Dps, poly(dGdC)$_2$ DNA, Ru(phen)(dppz)(bpy′)]$^{2+}$, and [Co(NH$_3$)$_5$Cl]$^{2+}$ with dark control subtracted. All conditions and instrument settings identical to Figure 5.

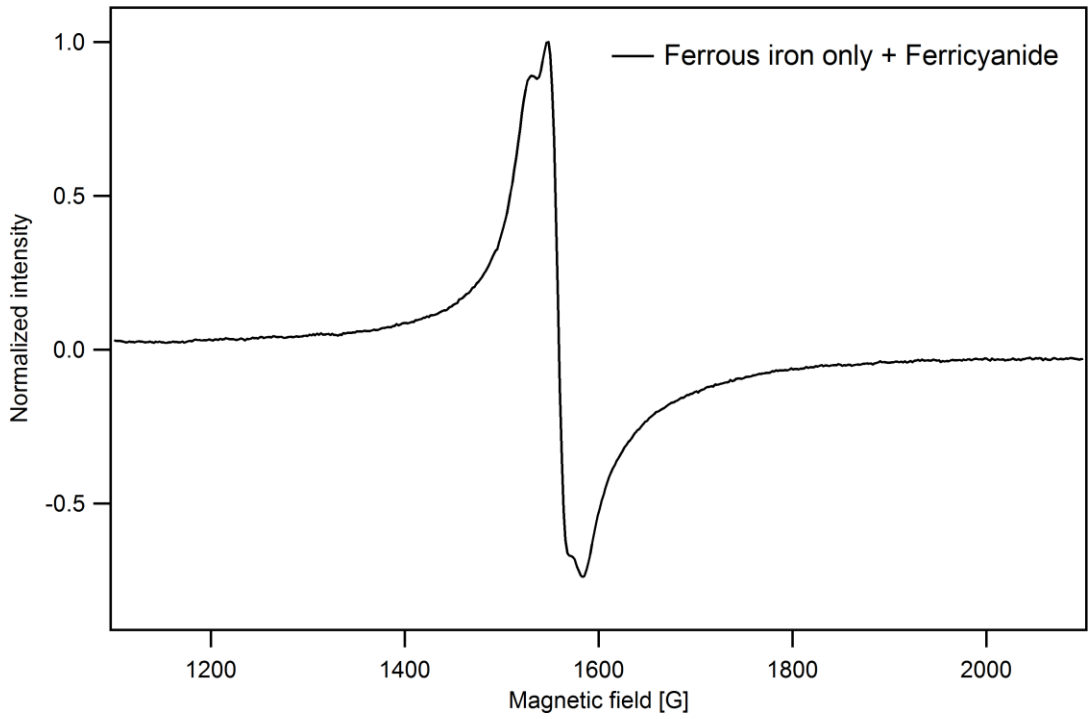

Figure 7. Ferrous iron only (no protein) mixed with stoichiometric ferricyanide in 50 mM Tris, pH 7.0, 150 mM NaCl, 5% glycerol. Concentration of iron was 240 μM, equivalent to that in 20 μM solution of Dps with 12 Fe/Dps. Instrument settings identical to Figure 5.

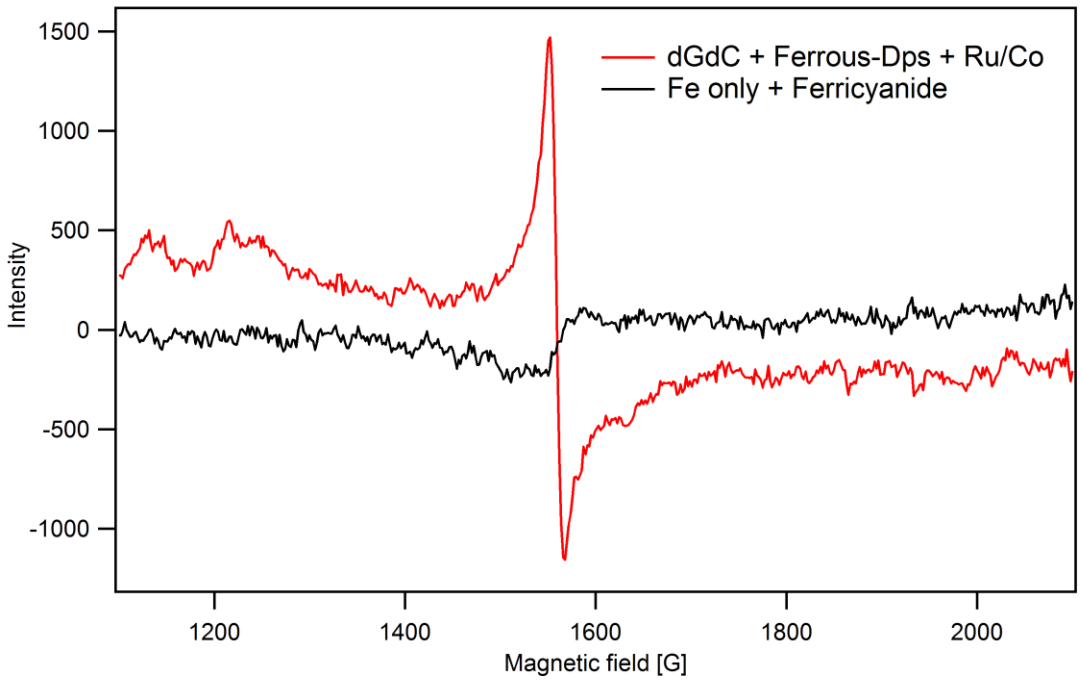

Figure 8. WT Dps EPR spectra compared to Fe only control in MOPS buffer. Concentrations: Fe only: 240 µM ferrous iron with 240 µM ferricyanide (black trace). Irradiated Dps sample: 20 µM Dps (Fe^{2+}/Dps: 11.7 ± 0.1), 1 mM base-pairs poly(dGdC)$_2$ DNA, 20 µM $[Ru(phen)(dppz)(bpy')]^{2+}$, 120 µM $[Co(NH_3)_5Cl]^{2+}$ (red trace). Buffer: 50 mM MOPS, pH 7.0, 150 mM NaCl, 5% glycerol. Dps spectrum has had DC subtracted. Instrument settings: modulation amplitude = 10 G at 100 kHz; frequency = 9.37 GHz; microwave power = 6.4 mW; temperature = 10 K.

3.3.3 EPR results comparing WT Dps with W52 mutants

The ability of ferrous iron-loaded W52A and W52Y Dps to be oxidized by ferricyanide, a diffusing oxidant, was first explored with EPR. Figure 9 shows oxidation of the W52 mutants compared to WT with equivalent moles of ferricyanide, with the EPR intensity adjusted for iron loading (i.e., Intensity / (Fe_{W52A}/Fe_{WT})). When the intensity of the EPR signal resulting from ferricyanide oxidation is adjusted for iron loading in this manner, the W52 mutants show similar yields of iron oxidation to WT Dps, with W52Y showing a slightly increased signal relative to WT. This result indicates that oxidation of the mononuclear iron site by a diffusing oxidant is not affected for W52A and W52Y Dps. Steady-state UV-Visible experiments with the W52 mutants upon oxidation with ferricyanide could be performed to confirm these EPR results.

Next, the X-band EPR spectra of ferrous iron-loaded WT *E. coli* Dps was compared to W52A and W52Y Dps upon DNA photooxidation with the flash-quench technique. Samples containing ferrous iron-loaded Dps, poly(dGdC)$_2$ DNA, non-covalent $[Ru(phen)(dppz)(bpy')]^{2+}$ and $[Co(NH_3)_5Cl]^{2+}$ were irradiated for identical lengths of time. The yield of iron oxidation at $g = 4.3$ was attenuated in the W52 mutants compared to the WT protein, even when adjusted for iron loading (Figure 10). Smaller signals are due to a lower modulation amplitude (5 G) compared to the WT spectra reported above (10 G). When the adjusted spectra are quantified by double integration from 1400 to 1600 gauss, the W52A iron signal is 3.4-fold less than WT, while the W52Y signal is 1.8-fold less than WT. The proficiency in oxidation of the iron sites in these W52 Dps mutants by a chemical

oxidant that directly diffuses to the iron site, combined with the deficiency in the yield of iron oxidation upon DNA photooxidation, suggests that W52 could play a role in mediating ET from the iron site to the DNA.

Because (*i*) the intercalating ruthenium photooxidant is a one-electron oxidant, and (*ii*) the mononuclear iron site has a much lower redox potential (as indicated by its oxidation by ferricyanide, 0.43 V versus NHE, *33*) than tryptophan or tyrosine, making it the thermodynamic sink, the deficiency in iron oxidation for these mutants suggests a role for W52 as an electron transfer hopping intermediate rather than a molecular capacitor. Furthermore, as with WT Dps, we do not have the time resolution and sufficient yields to directly observe the tryptophan or tyrosine radical with EPR.

Another important factor to consider is that the dark control EPR spectra (i.e. before irradiation) of the W52 mutants show evidence of Co^{2+} formation, whereas the WT protein does not (Figure 11). The cobalt quencher, $[Co(NH_3)_5Cl]^{2+}$, is a low-spin Co^{3+} d^6 species with $S = 0$. Upon reduction to Co^{2+}, the complex becomes labile, forming $[Co(H_2O)_6]^{2+}$, a high-spin d^7 species with $S = 3/2$ (EPR-active). Therefore, there may be some direct ET from the ferrous mononuclear iron site to the Co^{3+} quencher to yield EPR-active Co^{2+} in these mutants, perhaps because the ferroxidase site is more solvent-accessible. However, there is very little evidence of ferric iron formation in the DC spectrum of the W52A mutant, and in W52Y, a relatively small percentage of the total amount of iron in the sample is oxidized, allowing ample room for an increase upon irradiation. Thus the lower yield of iron oxidation that we observe upon DNA photooxidation with the W52 mutants is

significant, supporting our EPR results that suggest W52 as an electron transfer intermediate in Dps.

While it is readily rationalized how the W52A mutation would inhibit ET by deleting the aromatic residue, why might substitution of tryptophan for an aromatic tyrosine residue have such an effect? Work by Gray and co-workers has revealed that precise tuning of the reduction potential of hopping intermediates is essential for function (*34*,*35*). With tyrosine, the reduction potential can be modulated by adjacent basic amino acids such as His, Asp, or Glu that can hydrogen bond with the OH group of tyrosine (*35*). In *E. coli* Dps, no basic residues are in the vicinity of Y52 except for the ferroxidase site ligands, which are presumably coordinating iron. Therefore the Dps protein environment may support a tryptophan radical but not be as amenable to a tyrosine radical at the reduction potentials necessary for a hopping intermediate.

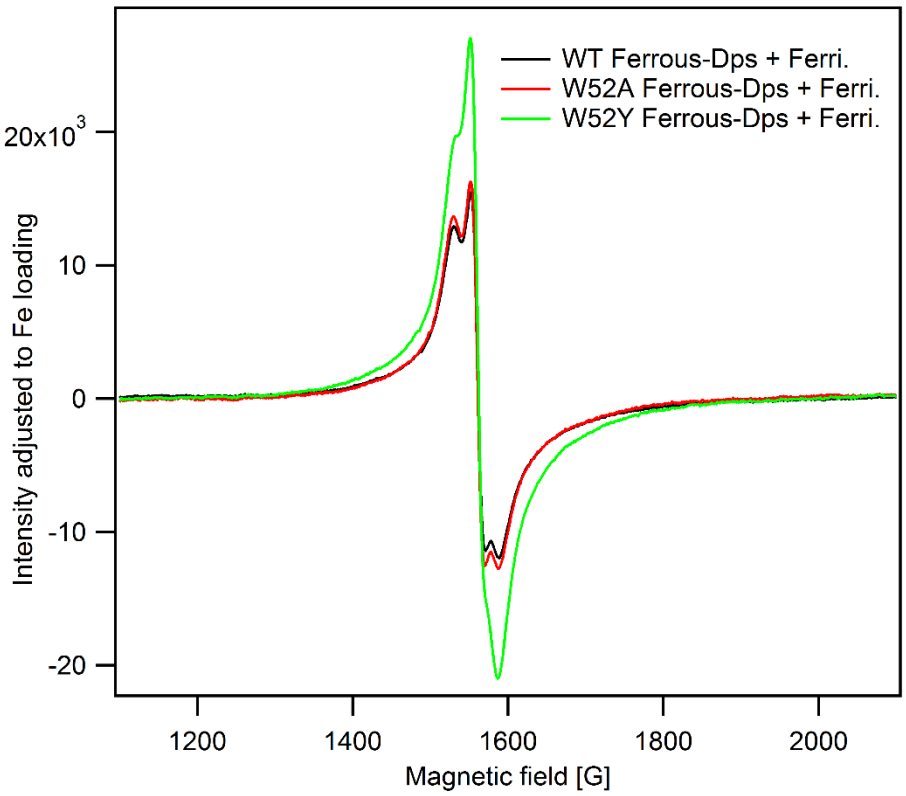

Figure 9. Chemical oxidation of ferrous iron-loaded WT, W52A and W52Y Dps upon mixing with equivalent moles of ferricyanide, with intensity adjusted for iron loading. Intensity was adjusted to that of the WT protein via dividing by the ratio Fe_{W52}/Fe_{WT}. Concentrations: 30 µM Dps (Fe^{2+}/Dps: WT: 13.0 ± 0.4, W52A: 8.9 ± 0.3; W52Y: 10.0 ± 0.1), 60 µM ferricyanide. Buffer: 50 mM Tris, pH 7.0, 150 mM NaCl. Instrument settings: modulation amplitude = 10 G at 100 kHz; frequency = 9.37 GHz; microwave power = 6.4 mW; temperature = 10 K.

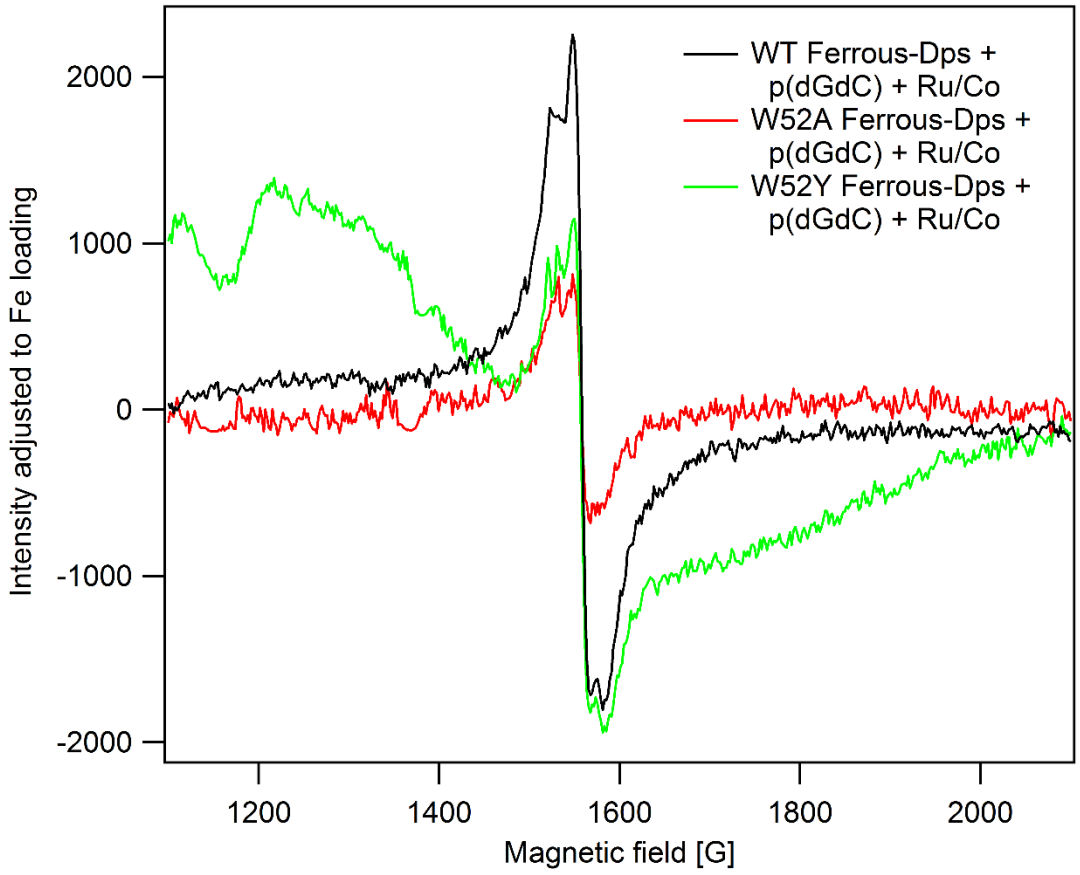

Figure 10. Comparison of ferrous iron-loaded WT Dps and W52A/Y mutant oxidation following DNA photooxidation via the flash-quench technique. All spectra have had an individual un-irradiated spectrum subtracted; thus all features are a function of irradiation. The intensity of the dark-control subtracted W52 spectra was then adjusted to iron loading of the WT protein via dividing by the ratio Fe_{W52}/Fe_{WT}. Concentrations: 20 μM Dps (Fe^{2+}/Dps: WT: 16.0 ± 0.5, W52A: 10.1 ± 0.2; W52Y: 11.5 ± 0.2), 1 mM base-pairs poly(dGdC)$_2$ DNA, 20 μM $[Ru(phen)(dppz)(bpy')]^{2+}$, 120 μM $[Co(NH_3)_5Cl]^{2+}$. Buffer: 50 mM Tris, pH 7.0, 150 mM NaCl, 5% glycerol. Instrument settings: modulation amplitude = 5 G at 100 kHz; frequency = 9.37 GHz; microwave power = 6.4 mW; temperature = 10 K.

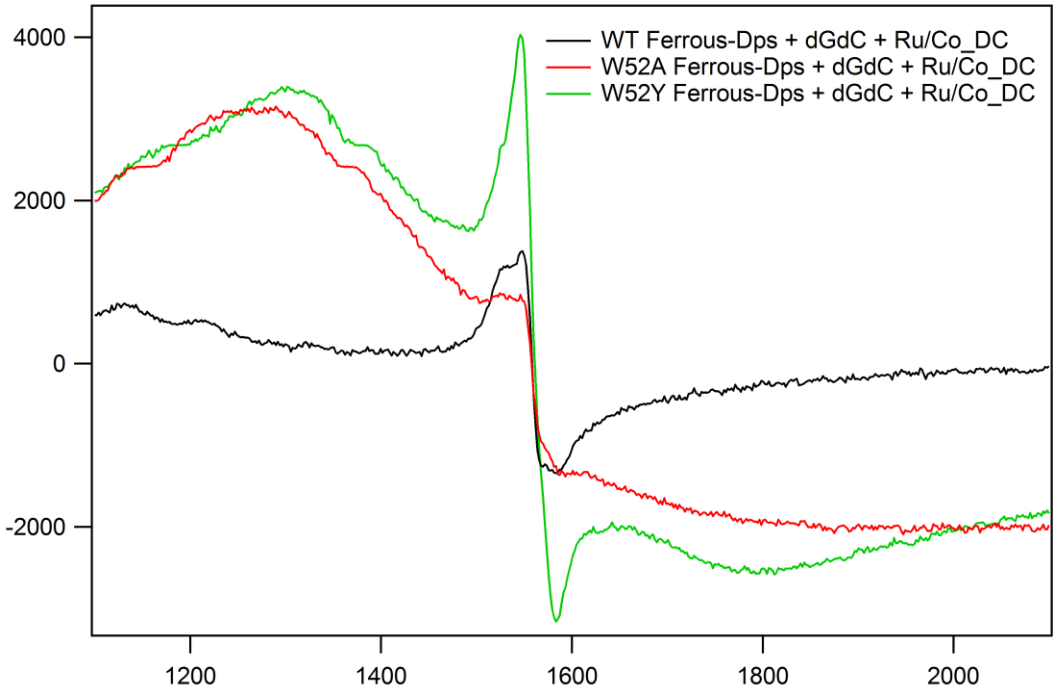

Figure 11. Dark controls (before irradiation) of DNA-bound ferrous iron-loaded WT Dps and W52A/Y mutants. Concentrations: 20 μM Dps (Fe^{2+}/Dps: WT: 16.0 ± 0.5, W52A: 10.1 ± 0.2; W52Y: 11.5 ± 0.2), 1 mM base-pairs poly(dGdC)$_2$ DNA, 20 μM $[Ru(phen)(dppz)(bpy')]^{2+}$, 120 μM $[Co(NH_3)_5Cl]^{2+}$. Buffer: 50 mM Tris, pH 7.0, 150 mM NaCl, 5% glycerol. Instrument settings: modulation amplitude = 5 G at 100 kHz; frequency = 9.37 GHz; microwave power = 6.4 mW; temperature = 10 K.

3.3.4 Hydrogen peroxide survival assay

The survival of *E. coli* upon exposure to hydrogen peroxide was investigated for cells containing WT, W52A, or W52Y Dps. The *dps* knockout *E. coli* strain (*dps*::*kan* Δ*recA* Δ*ara*) (ZK2471) was transformed with a pBAD18 plasmid containing either the *E. coli* WT, W52A, or W52Y *dps* gene under the control of an inducible promoter. Adapted from the method of Martinez and Kolter (*25*), cells were grown overnight and diluted into fresh media with the addition of either the inducer (+), L-arabinose, or sterile water (-). Cells were then grown to exponential phase (OD_{600} = 0.3-0.4) and challenged with varying concentrations of hydrogen peroxide. After stopping the reaction with catalase, cells were diluted and plated in order to quantify colony forming units (CFU). The results from two trials using a 0.2% w/v concentration of L-arabinose inducer are shown in Figure 12. Each data set (i.e., WT Dps induced, 0 – 50 mM hydrogen peroxide) was normalized to the number of colonies on the no hydrogen peroxide plate. The number of normalized colonies under each condition for each trial is shown as an individual point, with the filled markers representing cells with Dps induced and the open markers representing cells with Dps un-induced.

Like was previously observed (*25*), there is a clear difference in bacterial survival upon increasing concentrations of hydrogen peroxide between cells where WT Dps is induced compared to un-induced cells. Overall, cells containing WT Dps survived the hydrogen peroxide challenge best, as can be clearly seen in the inset of Figure 12, with surviving colonies at the highest concentration of hydrogen peroxide. Cells containing

W52Y Dps survive the hydrogen peroxide challenge more effectively than those with W52A Dps, which died off almost as quickly as the un-induced cells. This trend is similar to what was observed in EPR experiments, where the largest attenuation in the yield of iron oxidation following DNA photooxidation was seen with W52A Dps. Thus, W52 is important for cells containing Dps to survive this hydrogen peroxide challenge. In light of our EPR studies on the W52 Dps mutants, where we saw a difference in proficiency between chemical oxidation by a diffusing oxidant and oxidation following DNA photooxidation, some of this *in vivo* effect could be due to inhibition of the DNA-mediated oxidation of Dps upon mutation of W52.

Perhaps the tyrosine residue in W52Y Dps can yet act as a molecular capacitor inside cells, preventing reactive oxygen species (ROS) formation in the hydrogen peroxide oxidation of mononuclear iron sites. Therefore, a one-electron oxidant like $[Rh(phi)_2bpy]^{3+}$ may further elucidate the possible ET role of Dps W52 *in vivo*. The photooxidant $[Rh(phi)_2bpy]^{3+}$ does not require a diffusing quencher and selectively oxidizes DNA rather than producing ROS (*7*). This Rh complex has been previously used successfully to demonstrate SoxR and p53 oxidation within cells as a result of DNA photooxidation (*36*,*37*).

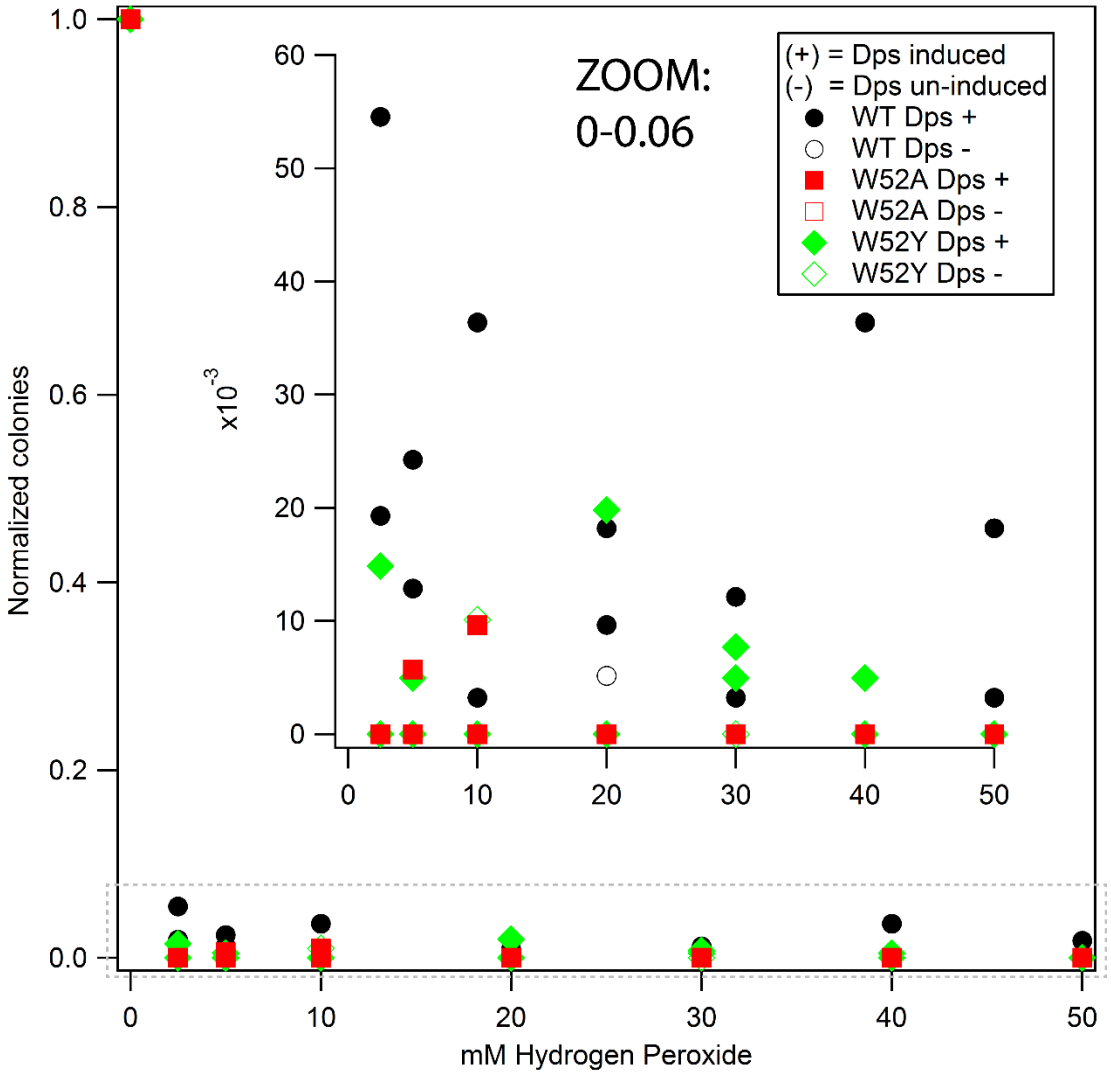

Figure 12. Hydrogen peroxide survival assay comparing *E. coli* with WT (black), W52A (red) or W52Y (green) Dps, where Dps has been either induced with 0.2% w/v L-arabinose (+, filled markers) or not induced (-, open markers). Each data set (i.e., WT Dps induced, 0 – 50 mM hydrogen peroxide) was normalized to the number of colonies on the no hydrogen peroxide plate. Inset is a zoom of the region shown in the gray dashed box (0 – 0.06 normalized colonies).

3.4 Conclusions

We have used EPR to spectroscopically confirm the oxidation of WT ferrous iron-loaded *E. coli* Dps following DNA photooxidation with the flash-quench technique. When poly(dGdC)$_2$ is substituted with poly(dAdT)$_2$ DNA, the yield of Dps oxidation as evidenced by mononuclear ferric iron species at an apparent *g*-value of 4.3, is decreased 3-fold, indicating that guanine radicals facilitate Dps oxidation. Because of the longer lifetime of the guanine radical, its formation likely allows more time for Dps oxidation by better competing with rapid BET to the intercalated ruthenium(III) oxidant produced by flash-quench. The more favorable oxidation of Dps by guanine radicals also supports the feasibility of our hypothesis of a long-distance protection mechanism via DNA CT where Dps is oxidized to fill guanine radical holes in the bacterial genome produced by ROS.

In 12-mer Dps proteins, there is a conserved tryptophan residue in close proximity to the ferroxidase site (W52 in the *E. coli* protein), whereas 24-mer ferritins contain a conserved tyrosine residue. In both cases, this aromatic residue has been proposed to act as a molecular capacitor, providing an extra electron during iron oxidation in order to prevent formation of oxygen radicals (*21*,*23*). The location of the conserved tryptophan residue in Dps proteins between the ferroxidase site and protein surface suggests a possible role as ET hopping intermediate in the DNA-mediated oxidation of the iron site. Here we use site-directed mutagenesis, creating W52A and W52Y *E. coli* Dps, to investigate this possibility. While overall protein folding seems unaffected by these mutations, iron binding is somewhat attenuated. When adjusted for iron loading, the yield of Dps oxidation by a diffusing

oxidant, ferricyanide, was not attenuated by these W52 mutations. However, even adjusted for iron loading, the level of iron oxidation observed in EPR experiments upon DNA photooxidation for both W52A and W52Y Dps is attenuated with respect to the WT protein, suggesting that W52 may play a role in mediating ET from the iron site to DNA. Because the intercalating ruthenium photooxidant used in these experiments is a one-electron oxidant, the deficiency in iron oxidation for these mutants suggests a role for W52 as an electron transfer hopping intermediate rather than a molecular capacitor. The reduction potentials may be precisely tuned to depend on tryptophan as a hopping intermediate, with the result that the tyrosine mutation is disruptive to ET.

We also probe the role of *E. coli* W52 Dps in cells using a hydrogen peroxide survival assay. Cells containing WT Dps survived the hydrogen peroxide challenge best. Whereas there was some attenuation in survival for cells containing W52Y Dps, W52A Dps cells died off almost as quickly as cells that lacked Dps altogether. In view of our EPR studies, some of this *in vivo* effect could be due to inhibition of the DNA-mediated oxidation of Dps upon mutation of W52. Perhaps this tyrosine residue can still act as a molecular capacitor inside cells, preventing ROS formation in the hydrogen peroxide oxidation of mononuclear iron sites. Therefore, a one-electron oxidant like $[Rh(phi)_2bpy]^{3+}$ may further elucidate the possible ET role of Dps W52 *in vivo*.

Interestingly, Dps seems to act as a checkpoint during oxidative stress to delay the initiation of DNA replication in *E. coli* until oxidative DNA damage has been repaired (*38*). Specifically, Chodavarapu *et al.* have shown that Dps interacts with DnaA, inhibiting DnaA-

dependent unwinding of the chromosomal origin (oriC). Thus elevated levels of Dps induced by OxyR under oxidative stress conditions reduce the frequency of replication initiation (*38*). Their data also suggest that DNA binding of Dps is necessary for the inhibition of oriC unwinding. This raises the question if Dps could be signaling with 4Fe4S cluster-containing DNA processing enzymes as part of this checkpoint inhibition.

While the reduction potentials of the ferroxidase site of *E. coli* Dps are unknown, the potential of the mononuclear iron site is less than that of ferricyanide (0.43 V versus NHE). Additionally, the reduction potentials of the ferroxidase site of *P. furiosus* ferritin have been reported as 210 mV for Fe^{3+}-Fe^{3+} to Fe^{3+}-Fe^{2+} and 50 mV for Fe^{3+}-Fe^{2+} to Fe^{2+}-Fe^{2+} (*39*). Therefore the reduction potentials of the ferroxidase site of Dps may perhaps be in an appropriate range to participate in DNA-mediated signaling with 4Fe4S cluster-containing helicases or base excision repair glycosylase enzymes. One could imagine a model where DNA-bound Dps oxidizes these proteins through DNA CT, causing them to remain bound to the DNA and process in towards lesions in the region of the oriC.

In conclusion, we have spectroscopically confirmed the oxidation of *E. coli* Dps following DNA photooxidation with the flash-quench technique, suggested the possibility of an ET hopping intermediate, and moved towards understanding the role of DNA CT with Dps in inside cells. Clearly further work is necessary to elucidate the possible roles of Dps *in vivo*.

References

1. Chiancone, E.; Ceci, P. The multifaceted capacity of Dps proteins to combat bacterial stress conditions: Detoxification of iron and hydrogen peroxide and DNA binding. *Biochim. Biophys. Acta* **2010**, *1800*, 798-805.

2. Zhao, G.; Ceci, P.; Ilari, A.; Giangiacomo, L.; Laue, T. M.; Chiancone, E.; Chasteen, N.D. Iron and hydrogen peroxide detoxification properties of DNA-binding protein from starved cells. *J. Biol. Chem.* **2002**, *277*, 27689-27696.

3. Ceci, P.; Cellai, S.; Falvo, E.; Rivetti, C.; Rossi, G. L.; Chiancone, E. DNA condensation and self-aggregation of *Escherichia coli* Dps are coupled phenomena related to the properties of the N-terminus. *Nucleic Acids Res.* **2004**, *32*, 5935-5944.

4. Wolf, S.G.; Frenkiel, D.; Arad, T.; Finkel, S.E.; Kolter, R.; Minsky, A. DNA protection by stress-induced biocrystallization. *Nature* **1999**, *400*, 83-85.

5. Grodick, M.A.; Muren, N.B.; Barton, J.K. DNA charge transport within the cell. *Biochemistry* **2015**, *54*, 962-973.

6. Saito, I.; Nakamura, T.; Nakatani, K.; Yoshioka, Y.; Yamaguchi, K.; Sugiyama, H. Mapping of the hot spots for DNA damage by one-electron oxidation: Efficacy of GG doublets and GGG triplets as a trap in long-range hole migration. *J. Am. Chem. Soc.* **1998**, *120*, 12686-12687.

7. Hall, D.B.; Holmlin, R.E.; Barton, J.K. Oxidative DNA damage through long-range electron transfer. *Nature* **1996**, *382*, 731-735.

8. Arkin, M.R.; Stemp, E.D.A.; Pulver, S.C.; Barton, J.K. Long-range oxidation of guanine by Ru(III) in duplex DNA. *Chem. Biol.* **1997**, *4*, 389-400.

9. Slinker, J.D.; Muren, N.B.; Renfrew, S.E.; Barton, J.K. DNA charge transport over 34 nm. *Nat. Chem.* **2011**, *3*, 228-233.

10. Arnold, A.R.; Barton, J.K. DNA protection by the bacterial ferritin Dps via DNA charge transport. *J. Am. Chem. Soc.* **2013**, *135*, 15726-15729.

11. Stemp, E.D.A.; Arkin, M.R.; Barton, J.K. Oxidation of guanine in DNA by $Ru(phen)_2(dppz)^{3+}$ using the flash-quench technique. *J. Am. Chem. Soc.* **1997**, *119*, 2921-2925.

12. Yavin, E.; Boal, A.K.; Stemp, E.D.A.; Boon, E.M.; Livingston, A.L.; O'Shea, V.L.; David, S.S.; Barton, J.K. Protein-DNA charge transport: Redox activation of a DNA repair protein by guanine radical. *Proc. Nat. Acad. Sci. USA* **2005**, *102*, 3546-3551.

13. Su, M.; Cavallo, S.; Stefanini, S.; Chiancone, E.; Chasteen, N.D. The so-called *Listeria innocua* ferritin is a Dps protein. Iron incorporation, detoxification, and DNA protection properties. *Biochemistry* **2005**, *44*, 5572-5578.

14. Zhao, G.; Ceci, P.; Ilari, A.; Giangiacomo, L.; Laue, T.M.; Chiancone, E.; Chasteen, N.D. Iron and hydrogen peroxide detoxification properties of DNA-binding protein from starved cells. *J. Biol. Chem*. **2002**, *277*, 27689–27696.

15. Schwartz, J.K.; Liu, X.S.; Tosha, T.; Diebold, A.; Theil, E.C.; Solomon, E.I. CD and MCD spectroscopic studies of the two Dps miniferritin proteins from *Bacillus anthracis*: Role of O_2 and H_2O_2 substrates in reactivity of the diiron catalytic centers. *Biochemistry* **2010**, *49*, 10516-10525.

16. Bou-Abdallah, F.; Chasteen, N.D. Spin concentration measurements of high-spin (g'=4.3) rhombic iron(III) ions in biological samples: theory and application. *J. Biol. Inorg. Chem*. **2008**, *23*, 15-24.

17. Gibson, J.F. EPR of iron in biological systems. In *ESR and NMR of Paramagnetic Species in Biological and Related Systems*. Bertini, I., Drago, R.S., Eds.; Springer: Netherlands, 1979, pp 225-253.

18. Sun, S.; Chasteen, N.D. Rapid kinetics of the EPR-active species formed during initial iron uptake in horse spleen apoferritin. *Biochemistry* **1994**, *33*, 15095-15102.

19. Hayden, J.A.; Hendrich, M.P. EPR spectroscopy and catalase activity of manganese-bound DNA-binding protein from nutrient starved cells. *J. Biol. Inorg. Chem*. **2010**, *15*, 729-736.

20. Nguyen, K.H.; Smith, L.T.; Xiao, L.; Bhattacharyya, G.; Grove, A. On the stoichiometry of *Deinococcus radiodurans* Dps-1 binding to duplex DNA. *Proteins* **2012**, *80*, 713-721.

21. Bellapadrona, G.; Ardini, M.; Ceci, P.; Stefanini, S.; Chiancone, E. Dps proteins prevent Fenton-mediated oxidative damage by trapping hydroxyl radicals within the protein shell. *Free Radical Bio. Med*. **2010**, *48*, 292-297.

22. Chen-Barrett, Y.; Harrison, P. M.; Treffry, A.; Quail, M. A.; Arosio, P.; Santambrogio, P.; and Chasteen, N. D. Tyrosyl radical formation during the oxidative iron deposition in the human apoferritin. *Biochemistry* **1995**, *34*, 7847-7853.

23. Ebrahimi, K.H.; Hagedoorn, P.-L.; Hagen, W.R. A conserved tyrosine in ferritin is a molecular capacitor. *ChemBioChem* **2013**, *14*, 1123-1133.

24. Bou-Abdallah, F.; Yang, H.; Awomolo, A.; Cooper, B.; Woodhall, M.R.; Andrews, S.C.; Chasteen, N.D. Functionality of the three-site ferroxidase center of *Escherichia coli* bacterial ferritin (EcFtnA). *Biochemistry* **2014**, *53*, 483-495.

25. Martinez, A.; Kolter, R. Protection of DNA during oxidative stress by the nonspecific DNA-binding protein Dps. *J. Bacteriol.* **1997**, *179*, 5188-5194.

26. David, S.S.; O'Shea, V.L.; Kundu, S. Base-excision repair of oxidative DNA damage. *Nature*, **2007**, *447*, 941-950.

27. Sovenyhazy, K.M.; Bordelon, J.A.; Petty, J.T. Spectroscopic studies of the multiple binding modes of a trimethine-bridged cyanine dye with DNA. *Nucleic Acids Res.* **2003**, *31*, 2561-2569.

28. Anderson P.A.; Deacon, G.B.; Haarmann, K.H.; Keene, F.R.; Meyer, T.J.; Reitsma, D.A.; Skelton, B.W.; Strouse, G.F.; Thomas, N.C.; Treadway, J.A.; White, A.H. Designed synthesis of mononuclear tris(heteroleptic) ruthenium complexes containing bidentate polypyridyl ligands. *Inorg. Chem.* **1995**, *34*, 6145-6157.

29. Kiassen, N.V.; Marchington, D.; McGowan, H.C.E. H_2O_2 determination by the I_3^- method and by $KMnO_4$ titration. *Anal. Chem.* **1994**, *66*, 2921-2925.

30. Grant, R.A.; Filman, D.J.; Finkel, S.E.; Kolter, R.; Hogle, J.M. The crystal structure of Dps, a ferritin homolog that binds and protects DNA. *Nat. Struct. Biol.* **1998**, *5*, 294-303.

31. Kelly, S.M.; Jess, T.J.; Price, N.C. How to study proteins by circular dichroism. *Biochim. Biophysica. Acta* **2005**, *1751*, 119-139.

32. O'Neill, M.A.; Barton, J.K. DNA charge transport: Conformationally gated hopping through stacked domains. *J. Am. Chem. Soc.* **2004**, *126*, 11471-11483.

33. Dutton, P.L. Redox potentiometry: Determination of midpoint potentials of oxidation-reduction components of biological electron-transfer systems. *Methods Enzymol.* **1978**, *54*, 411-435.

34. Shih, C.; Museth, A.K.; Abrahamsson, M.; Blanco-Rodriguez, A.M.; Di Bilio, A.J.; Sudhamsu, J.; Crane, B.R.; Ronayne, K.L.; Towrie, M.; Vlček, A. Jr.; Richards, J.H.; Winkler, J.R.; Gray, H.B. Tryptophan-accelerated electron flow through proteins. *Science* **2008**, *320*, 1760-1762.

35. Warren, J.J.; Winkler, J.R.; Gray, H.B. Redox properties of tyrosine and related molecules. *FEBS Lett.* **2012**, *586*, 596-602.

36. Lee, P.E.; Demple, B.; Barton, J.K. DNA-mediated redox signaling for transcriptional activation of SoxR. *Proc. Natl. Acad. Sci. USA* **2009**, *106*, 13164-13168.

37. Augustyn, K.E.; Merino, E.J.; Barton, J.K. A role for DNA-mediated charge transport in regulating p53: Oxidation of the DNA-bound protein from a distance. *Proc. Natl. Acad. Sci. USA* **2007**, *104*, 18907-18912.

38. Chodavarapu, S.; Gomez, R.; Vicente, M.; Kaguni, J.M. *Escherichia coli* Dps interacts with DnaA protein to impede initiation: a model of adaptive mutation. *Mol. Microbiol.* **2008**, *67*, 1331-1346.

39. Tatur, J.; Hagen, W.R. The dinuclear iron-oxo ferroxidase center of *Pyrococcus furiosus* ferritin is a stable prosthetic group with unexpectedly high reduction potentials. *FEBS Lett.* **2005**, *579*, 4729-4732.

Chapter 4

Multiplexed Electrochemistry of DNA-Bound Metalloproteins*

*Adapted from Pheeney, C.G.; Arnold, A.R.; Grodick, M.A.; Barton, J.K. *J. Am. Chem. Soc.* **2013**, *135*, 11869-11878. C.G.P. performed electrochemical measurements; A.R.A. performed mutagenesis and protein purification for mutant EndoIII as well as circular dichroism; M.A.G. performed protein purification of wild type EndoIII.

4.1 Introduction

Multiplexed electrodes are emerging as a powerful analytical tool particularly in the development of electrochemical diagnostics for the detection of pathogens and cancer markers (*1-13*). Multiplexed DNA-modified electrodes have been developed to sense an extensive range of targets including small molecules (*4,5,11*), DNA (*6,10-12*), RNA (*8,9,11*), and proteins (*3,7,11-13*). These devices all strive to achieve the same goals of enhanced sensitivity, faster detection times, and tolerance to cell lysates (*5,9,12*). Despite variety in the design of these multiplexed DNA-modified electrodes, they all possess the same intrinsic benefits of statistical comparisons and parallel experimentation; these advantages have proven to be essential for the electrochemical characterization of complex systems. Ultimately, these technologies possess ideal attributes for performing the next generation of fundamental electrochemical measurements as they have been optimized for low variability, real-time monitoring, and complex substrates.

The utility of multiplexed analysis for the fundamental studies of macromolecules was demonstrated in the characterization of charge transport through DNA (*12-14*). One such case is the measurement of ground-state DNA-mediated charge transport (DNA CT) through exceptionally long DNA distances up to 34 nm (*14*). DNA CT is the process through which charge is conducted through the π-stack of the DNA base pairs (*15-17*). Both the exquisite sensitivity of even a subtle perturbation in DNA stacking (*18,19*) and the shallow distance dependence (*14,15*) of DNA CT have been characterized using DNA-modified electrodes affixed with a redox-active moiety at the distal end of the duplex.

Multiplexing these DNA-modified electrodes onto a single device was crucial in establishing that the electrochemical signal was generated via DNA CT over such long molecular distances and that the π-stack of the DNA was well stacked and in a biologically relevant conformation (*14*).

Here we utilize multiplexed technology to investigate the electrochemistry of DNA repair proteins containing [4Fe-4S] clusters (Figure 1). DNA-modified electrodes have become a necessary tool to investigate the electrochemistry of the iron–sulfur cofactor of many DNA repair proteins, including endonuclease III (EndoIII), MutY, UDG, SoxR, and XPD, toward identifying the *in vivo* relevance for this redox activity (*20-24*). Upon DNA binding of EndoIII, the $3^{+}/2^{+}$ redox couple of its [4Fe-4S] cluster has been shown to shift approximately –200 mV compared to freely diffusing protein, to approximately 80 mV versus NHE (*25*). Thus, binding of the DNA polyanion brings the $3^{+}/2^{+}$ redox potential of the [4Fe-4S] cluster into a physiologically relevant range. Moreover, disease-related mutants show deficiencies in DNA CT through their weaker electrochemical signals. Interestingly, DNA binding proteins involved in genome maintenance have increasingly been found to contain [4Fe-4S] clusters (*26-29*). We have proposed that the redox chemistry of these [4Fe-4S] clusters is critical as a first step in the search mechanism used by DNA repair proteins to redistribute to the vicinity of DNA damage (*21,30*). The proposed model hinges on the ability of these [4Fe-4S] cluster proteins to electronically couple to the π-stack of DNA in order to perform efficient searching of the genome facilitated by DNA CT. This efficient DNA-mediated CT between repair proteins seems to depend on the similar reduction

potentials of their clusters. The consistent DNA-bound midpoint potential of these various proteins containing [4Fe-4S] clusters has been of particular interest. In this work, we investigate how the electrostatics of the protein fold, in addition to binding of the DNA polyanion, may tune the reduction potential of the cluster. Thus, it becomes important to characterize the DNA-bound electrochemistry of these proteins containing [4Fe-4S] clusters in a quantitative manner that allows for direct side-by-side comparison of potentials and couplings through multiplexing.

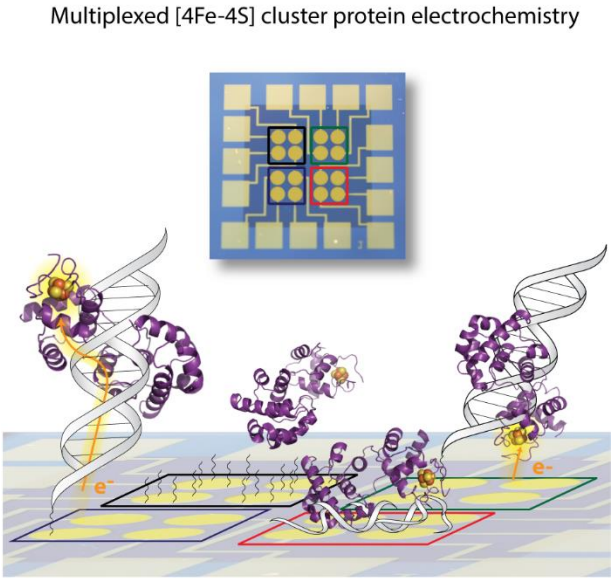

Figure 1. Schematic depicting the versatility of multiplexed analysis for the investigation of metalloprotein electrochemistry. Our multiplexed devices are composed of 16 electrodes that are divisible into four separate quadrants of four electrodes, having the capability of producing four distinct experimental conditions on a single Au surface. This assembly allows for facile comparisons of the electrochemical signal from various DNA-bound proteins across varying DNA substrates and morphologies.

4.2 Experimental section

4.2.1 Oligonucleotide preparation

All DNA substrates were synthesized on a 3400 Applied Biosystems DNA synthesizer with all phosphoramidites and reagents purchased from Glen Research. The sequences of the DNA substrates used were 5′-HS-C_6-AGTACAGTCATCGCG-3′ for the thiol strand and 3′-TCATGTCAGTAGCGC-5′ for the complement strand. Additional complements were prepared that yield either a TC mismatch or an abasic site at the position of the underlined adenine. Both the complement and thiol-modified DNA were purified through standard procedures as previously reported (*13*). All single-stranded DNA was purified by high-pressure liquid chromatography (HPLC) using a reverse-phase PLRP-S column, purchased from Agilent. The identity of the oligonucleotides was confirmed by matrix-assisted laser-desorption ionization time-of-flight (MALDI-TOF) mass spectrometry. The thiol-modified single-stranded DNA was reduced with 100 mM dithiothreitol (Sigma) in Tris buffer (50 mM Tris HCl, 50 mM NaCl, pH 8.4) for 40 minutes and purified by size exclusion chromatography (Nap5 Sephadex G-25, GE Healthcare) as well as reverse-phase HPLC. Single-stranded DNA stocks were then desalted by precipitation in ethanol and resuspended in phosphate buffer (5.0 mM phosphate, 50 mM NaCl, pH 7.0). Equimolar amounts of single-stranded stocks were combined based on quantification by UV-visible spectroscopy. The extinction coefficients at 260 nm from the IDT SciTools were used for the quantification of the single-stranded DNA stocks. All DNA solutions were then

thoroughly deoxygenated with argon and annealed by heating to 90°C followed by a slow cooling to ambient temperature over 90 min.

4.2.2 Site-directed mutagenesis

E200K, Y205H, and K208E EndoIII mutants were prepared using a pET11 vector containing the *nth* gene with N-terminal ubiquitin and hexahistidine tags (*22*) and a Quikchange II-E site-directed mutagenesis kit (Stratagene). Y82A EndoIII was prepared previously (*22*). Primer sequences are shown in Table 1, with mutagenized codons underlined. Primers were purchased from Integrated DNA Technologies. All mutagenized plasmids were sequenced (Laragen) to confirm the desired sequences.

4.2.3 Protein overexpression and purification

Mutant and WT pET11 plasmids were transformed into BL21star(DE3)pLysS *Escherichia coli* cells (Invitrogen) for overexpression. The EndoIII proteins were overexpressed and purified according to a protocol adapted from published procedures (*22*). Specifically, a stock of BL21star-(DE3)pLysS containing a pET11-ubiquitin-His_6-*nth* construct was used to inoculate a 100 mL culture of LB containing 100 μg/mL of ampicillin and 35 μg/mL of chloramphenicol. This culture was grown overnight at 37°C with shaking. Then, 1 mL of the overnight culture was used to inoculate each of four 1L cultures of LB containing the same amount of ampicillin and chloramphenicol as the overnight culture. The 1L cultures were shaken at 37°C until the OD_{600} reached ~0.6-0.8. Enough isopropyl β-D-1-thiogalactopyranoside (IPTG) was then added to bring the total concentration of IPTG to 300 μM. The cultures were subsequently shaken at 150 rpm for ~3.5 hours at

30°C. The cells were collected by centrifugation at 5,500 rpm for 15 minutes, flash-frozen, and stored at -80°C. All subsequent steps were carried out at 4°C or on ice.

On the day of the purification the pellet was resuspended in 250 mL of Buffer A (20 mM sodium phosphate, pH 7.4, 250 mM NaCl, 5 mM DTT, 5% glycerol, DNase (Roche), RNase (Roche), and EDTA-free protease inhibitor cocktail tablets (Roche)). The resuspended cells were lysed via microfluidization. The cell lysate was clarified by centrifugation at 17,000 *g* for 30 minutes. Enough NaCl was added to the resulting supernatant to bring the NaCl concentration to 500 mM. The supernatant was then loaded onto a Histrap HP column (GE Healthcare) that had been equilibrated with buffer B (20 mM sodium phosphate, pH 7.4, 500 mM NaCl, 1 mM DTT). After washing with buffer B, EndoIII was eluted using a gradient from 0-100% buffer C (20 mM sodium phosphate, pH 7.4, 500 mM NaCl, 500 mM imidazole, 1 mM DTT) over 20 column volumes. A yellow band that eluted at ~100 mM imidazole was collected. This imidazole-containing buffer was then immediately exchanged into buffer D (20 mM sodium phosphate, pH 7.4, 500 mM NaCl, 0.5 mM EDTA, and 20% glycerol) using a HiPrep 26/10 desalting column (GE Healthcare). The protein solution, now in buffer D, was concentrated down to ~5 mL using 10,000 MWCO Amicon Ultra-15 centrifugation filter units (Millipore) and was loaded onto a HiLoad Superdex 16/600 75 pg size exclusion column (GE Healthcare) that had been equilibrated with the protein storage buffer (20 mM sodium phosphate, pH 7.4, 100 mM NaCl, 0.5 mM EDTA, 20% glycerol). A clean peak that eluted after approximately 50-55 mL of buffer had passed through the column was collected and

concentrated to achieve a final concentration of ~100 μM as quantified using an ε_{410} of 17,000 $M^{-1}cm^{-1}$ (*30*). The protein was then aliquoted, flash-frozen in liquid nitrogen and stored at -80°C. The approximate yield was 6 mg/L. The purity of the protein was determined to be >95% as analyzed by SDS-PAGE (data not shown). The glycosylase activity of mutants was compared to that of wild-type EndoIII based on previously established methods (*22*).

4.2.4 Multiplexed chip fabrication

Multiplexed chips consisting of 16 gold electrodes were prepared using standard photolithography techniques as adapted from previously established protocols (*13*). Photoresist was used to pattern nine 1 in. by 1 in. chips on 525 μm thick silicon wafers (SiliconQuest) that had a thermal oxide layer grown to a thickness of roughly 4000 Å to insulate the wafer. A titanium adhesion layer (3 nm) followed by a gold layer (100 nm) was deposited using an electron beam evaporator without breaking the vacuum between depositions. The metal lift-off was performed directly after metal deposition using Remover PG (MicroChem) heated to 60 °C for 1 hour. The wafers were then dehydrated by baking at 180 °C for at least 2 hours, and an insulating SU8 layer (3 μm) was coated on the wafer. This SU8 layer was patterned such that the working electrodes and contact pads were left exposed, yet the connective wires were covered to define a controlled working electrode area (2 mm^2). The SU8 was cured with a final hard bake at 150 °C for 15 minutes. The wafer was then cleaved into individual chips (Dynatex Scriber/Braker) to prevent any scratching of the exposed working electrode surfaces.

4.2.5 DNA-modified electrode assembly

Single electrode experiments were performed with a low-volume constrained Au(111) on mica surface (Molecular Imaging), as previously established (*20*). Multiplexed electrode experiments were performed with the 16 electrode chips divided into four quadrants of four electrodes each (*13*). Multiplexed chips were cleaned in acetone and isopropyl alcohol as well as ozone-cleaned for 5 minutes at 20 mW immediately prior to the assembly into a holder and the exposure to thiol-modified DNA. The cleaned chip was then assembled in a polycarbonate holder used to position the chip. A rubber gasket and acrylic clamp is used to define the four quadrants and create a common central well. The rubber Buna N gasket (0.020 in. thick, unless otherwise indicated) and clamp are manufactured by SAS Industries and Xcentric, respectively. A fresh gasket and clamp are used for each experiment to prevent any cross-contamination between experiments.

Duplex DNA (20 μL of 25 μM) was placed in each quadrant of a multiplexed chip and left to self-assemble overnight (16–24 hours) in a humid environment. To ensure efficient monolayer formation, thiol-modified DNA was used within 2 weeks of the dithiothreitol reduction. Loosely packed DNA films were assembled in the absence of $MgCl_2$, while closely packed DNA films were assembled with the addition of 100 mM $MgCl_2$. Once DNA films were assembled and thoroughly washed with phosphate buffer, the electrodes were backfilled with 1 mM 6-mercaptohexanol (MCH) for 45 minutes in phosphate buffer with 5% glycerol. Background scans were acquired with common running buffers exposed to the electrodes. An initial background scan is acquired in phosphate buffer

(5 mM phosphate, 50 mM NaCl, pH 7.0) followed by a subsequent scan in spermidine buffer (5 mM phosphate, 50 mM NaCl, 40 mM $MgCl_2$, 5 mM spermidine, pH 7.0).

4.2.6 Protein electrochemical measurements

Electrochemical measurements were performed with a CHI620D electrochemical analyzer and a 16-channel multiplexer from CH Instruments. A three-electrode setup was used with a common Pt auxiliary and a quasi Ag/AgCl reference electrode (Cypress Systems) placed in the central well of the clamp. Cyclic voltammetry data were collected at 100 mV/s over a window of 0.1 mV to -0.4 mV versus Ag/AgCl unless otherwise indicated. After background scans, EndoIII samples in phosphate buffer (20 mM sodium phosphate, 100 mM NaCl, 0.5 mM EDTA, 20% glycerol, pH 7.4) were added to the central well or separated quadrants (120 μL total for the four quadrants), ranging in concentrations from 30 to 90 μM quantified using the absorbance of the [4Fe-4S] cluster at 410 nm (ε = 17,000 $M^{-1}cm^{-1}$) (*30,31*). EndoIII was allowed to incubate on the multiplexed chip for up to 12 hours and monitored over time. The chip was stored in a humid environment between subsequent scans to prevent solution evaporation and hold the concentration constant over time.

4.2.7 Circular dichroism thermal denaturation

For protein samples (5 μM), the ellipticity at 223 nm (the largest difference between native and denatured protein) was measured as a function of increasing temperature (20 to 60°C) using a model 62A DS circular dichroism spectrometer (AVIV). All data shown are the average of at least duplicate measurements. Measured ellipticity was converted to

fractional change in ellipticity by assigning the native protein a value of 0 and the fully denatured protein a value of 1. In order to extract melting temperature values, data were fit using a nonlinear least-squares regression to a simple two-state unfolding model (*32*), shown in Equation 1. Reported errors in T_m values are derived from this fitting.

Table 1. Primer sequences used to create Y205H, E200K, and K208E EndoIII with mutagenized codons underlined.

Mutation	Primer
Y205H	5'- TGT GAA **CAC** AAA GAG AAA GTT GAC ATC TGA GGA TCC GGC TGC TAA C -3' (Forward)
	5'- GTT AGC AGC CGG ATC CTC AGA TGT CAA CTT TCT CTT T**GT** **G**TT CAC A -3' (Reverse)
E200K	5'- GCC CCG CTG TGG CTC TTG TAT TAT T**AA** **A**GA TCT TTG TGA ATA C -3' (Forward)
	5'- GTA TTC ACA AAG ATC **TTT** AAT AAT ACA AGA GCC ACA GCG GGG C -3' (Reverse)
K208E	5'- GTG AAT ACA AAG AG**G** **AA**G TTG ACA TCT GAG GAT CCG GCT GCT AAC -3' (Forward)
	5'- GTT AGC AGC CGG ATC CTC AGA TGT CAA C**TT** **C**CT CTT TGT ATT CAC -3' (Reverse)

$$Y = \frac{(y_n + m_n T) + (y_d + m_d T) exp\left(\frac{\Delta H_m}{R}\left(\frac{1}{T_m} - \frac{1}{T}\right)\right)}{1 + exp\left(\frac{\Delta H_m}{R}\left(\frac{1}{T_m} - \frac{1}{T}\right)\right)}$$

Equation 1. Circular dichroism (CD) thermal denaturation data was fit using a non-linear least-squares regression to a simple two-state unfolding model (*32*), where Y is the fractional ellipticity, T is the temperature in Celsius, ΔH_m is the enthalpy at the unfolding transition, T_m is the melting temperature (°C), R is the ideal gas constant, while m_n and y_n describe the pre-transition (native protein) slope and y-intercept and m_d and y_d describe the equivalent values post-transition (denatured protein). Reported errors in T_m values are derived from this fitting.

4.3 Results

4.3.1 Multiplexed electrochemistry of EndoIII

The electrochemical behavior of the [4Fe-4S] cluster of EndoIII incubated on loosely packed DNA films, assembled in the absence of $MgCl_2$, was first compared between individual and multiplexed electrode assemblies. A reversible signal for the [4Fe-4S] cluster of EndoIII, with the ratio of the reduction and oxidation currents being near unity, at a midpoint potential of 80 ± 3 mV vs NHE was observed on both single electrode and multiplexed assemblies (Figure 2). The signal size for the redox couple of EndoIII depended on incubation time and concentration on both assemblies; this behavior as well as the midpoint potential is consistent with previously established results for EndoIII on DNA-modified electrodes (*22*). The consistency across all 16 multiplexed electrodes was comparable to that seen with previous multiplexed DNA-modified electrodes and showed at most a 3.5% deviation in signal size (Figure 2) (*13*). The analogous experiment run on individual single electrodes would yield dramatically higher variability on the order of 20-40% (*22*).

Due to the modular nature of the multiplexed electrode assembly, the thickness of the rubber gasket used to seal the central well was varied to increase accessibility to the electrodes. Background scans and EndoIII signal sizes were compared for gaskets 0.064, 0.032, and 0.020 in. thick. Oxygen contributions in the background scans, likely caused by trapped oxygen in close proximity to the electrode surface, were decreased drastically with the use of the thinner gaskets yielding much more uniform CVs and increased EndoIII signal

size (Figure 3). Overall, the most exposed electrodes produced a featureless background scan resulting in a 0.020 in. thick Buna N gasket being utilized for all subsequent experiments.

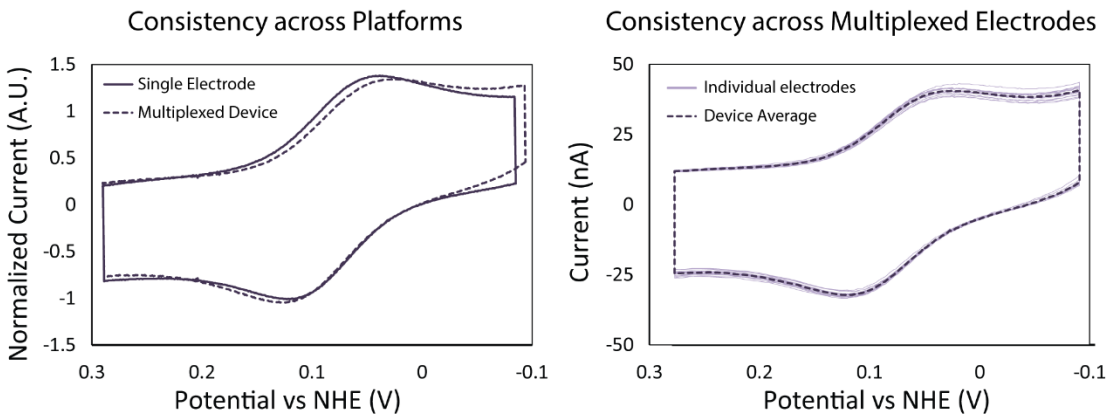

Figure 2. Consistency of DNA-modified electrodes. (*Left*) Signals generated after incubation of loosely packed DNA-modified electrodes with EndoIII (30 μM) in phosphate buffer (20 mM sodium phosphate, 100 mM NaCl, 0.5 mM EDTA, 20% glycerol, pH 7.4) were used to directly compare the single (solid) and multiplexed (dashed) electrochemical assemblies. The cyclic voltammetry (scan rate = 100 mV/s) was normalized, based on the capacitance at 0.3 mV vs NHE, so relative signal sizes could be compared across platforms. (*Right*) Variability of the EndoIII signal, under the same conditions, across all 16 electrodes (light solid line) of a single multiplexed device was within 3.5% of the average CV for the device (dark dashed line).

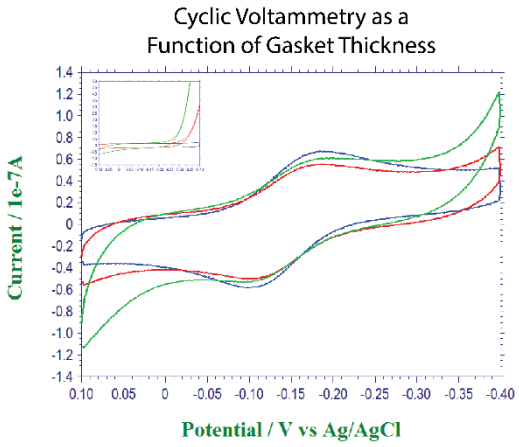

Figure 3. Cyclic voltammetry (scan rate = 100 mV/s) of EndoIII (30 μM) incubated on closely packed well-matched duplex DNA monolayers acquired in phosphate buffer (20 mM sodium phosphate, 100 mM NaCl, 0.5 mM EDTA, 20 % glycerol, pH 7.4) are presented. Three different thicknesses for the Buna N gasket, utilized during the multiplexed chip assembly, were tested: 0.64″ (green), 0.32″ (red), and 0.20″ (red). With decreasing gasket thickness the signal generated from EndoIII is shown to increase while the background contributions decrease. *Inset*: Background signals acquired prior to the addition of EndoIII in spermidine buffer (5 mM phosphate, 50 mM NaCl, 40 mM $MgCl_2$, 5 mM spermidine, pH 7.0).

4.3.2 EndoIII on differing DNA monolayers

The effect of DNA substrates and film morphology on the EndoIII signal was next investigated. Allowing the self-assembly of DNA monolayers to form in the presence of $MgCl_2$ dramatically affects the film packing and ultimately the density of the DNA monolayer formed (*33*). In the presence of $MgCl_2$, the negative charge of the DNA phosphate backbone is screened, allowing neighboring duplexes to more closely associate and self-assemble into a tightly packed DNA monolayer.

Incubation of EndoIII on DNA-modified electrodes assembled with duplex DNA (dsDNA) was found to produce a redox couple with the same midpoint potential as previously described (80 ± 3 mV vs NHE) regardless of DNA film morphology, while single-stranded DNA (ssDNA) monolayers showed cyclic voltammograms that were relatively featureless compared to background scans, even after 8 hours of protein incubation (Figure 4). As both the underlying gold surface and the protein solution were common across all electrodes, this appearance of a reversible redox couple from EndoIII on the dsDNA monolayers but not on the ssDNA films indicates that the signal generated from EndoIII is dependent on binding to duplex DNA. Moreover, since the DNA-bound redox potential for EndoIII is not observed on these ssDNA-modified electrodes, these ssDNA-modified electrodes provide a useful control against surface contaminants.

The DNA-bound signal of EndoIII was then compared on DNA-modified electrodes assembled with different morphologies. The peak splitting for the $3^+/2^+$ redox couple of the [4Fe-4S] cluster of EndoIII was found to be dependent on monolayer morphology, while the

midpoint potential remained unaltered. The consistency of the midpoint potentials between the surface morphologies indicates that EndoIII is in the same electrostatic environment, bound to duplex DNA, regardless of the monolayer morphology. The closely and loosely packed DNA monolayers show peak splittings of 88 ± 4 and 64 ± 2 mV, respectively (Figure 4). In addition to the increase in peak splitting, there is also a broadening of the signal observed upon switching to the more closely packed DNA films. Increases in the peak splitting and broadening of the redox couple are both indicative of decreases in the rate of electron transfer and the homogeneity of the electrochemical process (*34*). These two characteristics, an increase in peak splitting and heterogeneity, have previously been seen as characteristics of a redox-active moiety on DNA-modified electrodes being reduced by DNA CT (*35*).

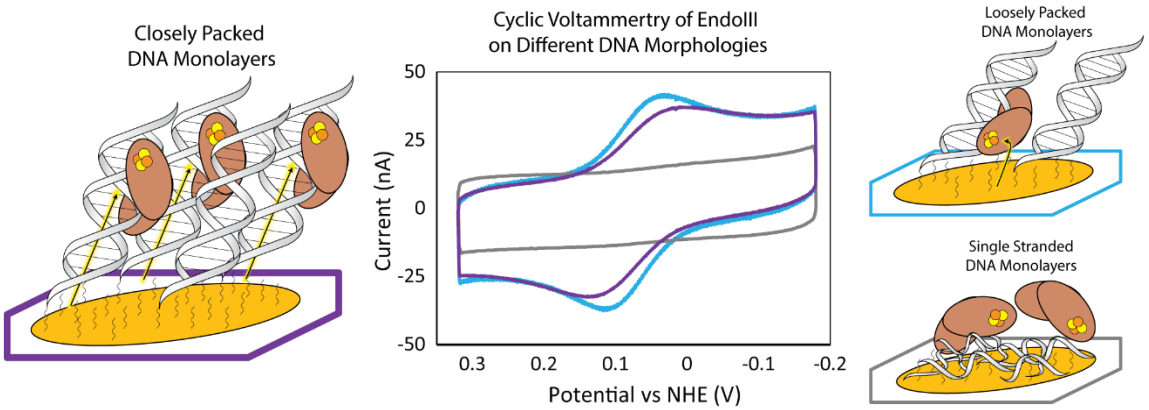

Figure 4. Electrochemistry of EndoIII on DNA-modified electrodes was determined as a function of the underlying DNA film morphology. DNA monolayers were allowed to self-assemble over 16-24 hours either with or without 100 mM $MgCl_2$ to form either closely (purple) or loosely (blue) packed DNA monolayers. All morphologies were directly compared on the same multiplexed device so the differences in the EndoIII (60 µM) redox signal could be resolved. Cyclic voltammetry scans (scan rate = 100 mV/s) were compared in phosphate buffer (20 mM sodium phosphate, 100 mM NaCl, 0.5 mM EDTA, 20% glycerol, pH 7.4), and the peak splitting and signal size were both quantified. Single-stranded DNA monolayers (gray) were prepared and shown to not produce a DNA-bound EndoIII signal.

4.3.3 DNA-mediated electrochemistry of EndoIII

The mechanism of electron transfer to the [4Fe-4S] cluster in EndoIII was next investigated on both loosely and closely packed dsDNA modified electrodes. DNA-mediated reduction is exceptionally sensitive to even subtle perturbations to the intervening π-stack (*18,19*). Therefore, the yield of [4Fe-4S] cluster reduction was examined after introducing a single perturbation site into the DNA duplexes self-assembled on the electrodes. Either a single thymine-cytosine mismatch (TC) or an abasic site (Ab) was incorporated into thiol-modified dsDNA near the electrode surface to prevent EndoIII binding to the π-stack below the perturbation site, as EndoIII binds nonspecifically to non-substrate DNA. The dsDNA stocks for the well-matched (WM), TC, and Ab sequences were all quantified and annealed using the same thiol-modified ssDNA stock. This consistency of the thiol strand avoids any variability caused by the efficiency of monolayer formation due to the reactivity of the thiol modifier. These dsDNA sequences, as well as a ssDNA control, were then assembled on a multiplexed chip.

The reduction signal for the [4Fe-4S] cluster of EndoIII was characterized across these different DNA substrates on both loosely and closely packed films (Figure 5). When these DNA substrates were assembled in the presence of $MgCl_2$, producing closely packed DNA monolayers, the reduction signal of EndoIII was attenuated upon introducing single base pair lesions. The WM, TC, and Ab dsDNA monolayers gave signal sizes of 56 ± 1, 42 ± 1, and 41 ± 4 nA, respectively, after EndoIII incubation (60 μM for 8 hours), resulting in an average signal attenuation of 24 ± 1 and 26 ± 2% upon incorporating a TC mismatch

or an abasic site, respectively (Figure 5). This attenuation in the reduction signal due to the incorporation of perturbations to the π-stack supports the assignment of the electrochemical signal from EndoIII observed on closely packed DNA films being mediated by DNA CT. Conversely, when the same set of DNA substrates was compared using loosely packed DNA monolayers, there was no significant difference in the reduction signal observed with the introduction of these perturbations. The loosely packed DNA monolayers of WM, TC mismatched, and Ab DNA produced signal sizes of 45 ± 0.3, 42 ±1, and 44 ± 1 nA, respectively, which yield a p value >0.05 when compared using a one-tailed t test, do not display statistically significant signal attenuation as compared to EndoIII bound to the closely packed DNA monolayer. This lack of signal attenuation with the incorporation of perturbation to the π-stack indicates that the DNA-bound signal of EndoIII is not mediated by electron transfer through the π-stack in loosely packed DNA monolayers.

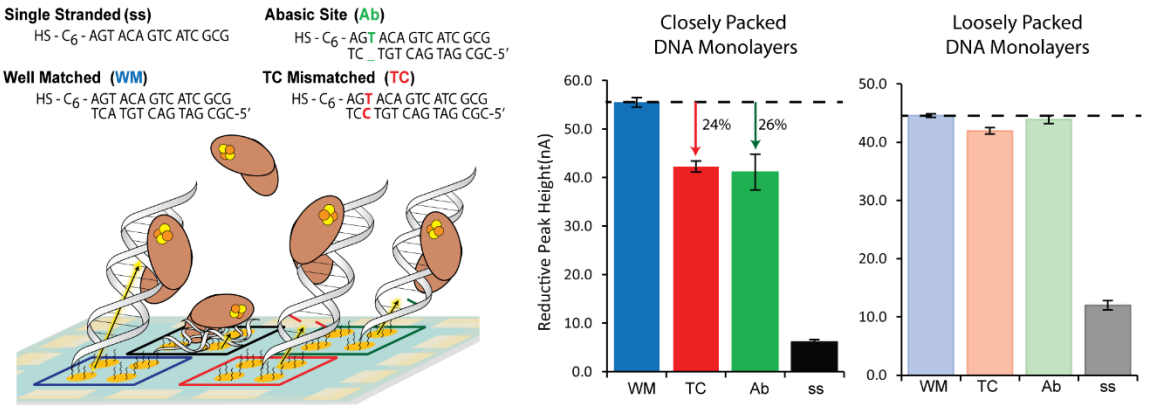

Figure 5. Degree of signal attenuation induced by a single perturbation to the π-stack for both closely and loosely packed DNA monolayers was investigated. (*Left*) Schematic of multiplexed devices prepared with well-matched (blue), TC-mismatched (red), and abasic site (green) duplex DNA, and a single-stranded control (black). The sequences are indicated above. (*Right*) Reductive signals from DNA-bound EndoIII in phosphate buffer (20 mM sodium phosphate, 100 mM NaCl, 0.5 mM EDTA, 20% glycerol, pH 7.4) were quantified for DNA monolayers assembled in both the presence (dark) and the absence (light) of 100 mM $MgCl_2$, yielding closely and loosely packed DNA, respectively. The percent signal attenuations of the TC mismatch and abasic site were determined based on the average signal size, across all four electrodes in a quadrant, compared to that of well-matched DNA. The signals generated from closely packed DNA films displayed distinct attenuation upon introducing either a mismatch or abasic site, while the signals from loosely packed DNA films did not display this sequence dependence.

4.3.4 Kinetics of EndoIII reduction

The kinetics of EndoIII reduction was assessed on these two different dsDNA morphologies to explore further the mechanistic differences in the electron transfer pathways. In addition to the peak splitting, the EndoIII reduction on loosely and closely packed DNA monolayers was found to differ in the signal accumulation both as a function of scan rate as well as incubation time. For a diffusion rate-limited process, this signal accumulation increases linearly as a function of the square root of the scan rate (*34*). The [4Fe-4S] cluster signal of EndoIII was measured over 10 different scan rates ranging from 10 to 200 mV/s on both loosely and closely packed dsDNA films and plotted as a function of the square root of the scan rate, $\nu^{1/2}$ (Figure 6). In the case of loosely packed dsDNA films, the current was found to be linear with respect to $\nu^{1/2}$, as previously established for the diffusion-rate-limited reduction of DNA-bound [4Fe-4S] cluster proteins on this dsDNA film morphology (*24*). The same protein solution, on the same multiplexed chip, displayed nonlinear behavior on closely packed dsDNA films. More quantitative approaches for determining the rate of electron transfer, such as the Laviron analysis, were not possible due to the degree of heterogeneity of the observed electrochemical signals. However, the total signal accumulation for the reduction of EndoIII as a function of time on both these dsDNA film morphologies displayed the same trend; loosely versus closely packed dsDNA films accumulated signal linearly and nonlinearly, respectively, over time (Figure 7). This further supports the finding that only the signal observed on the loosely packed dsDNA films is limited by diffusion.

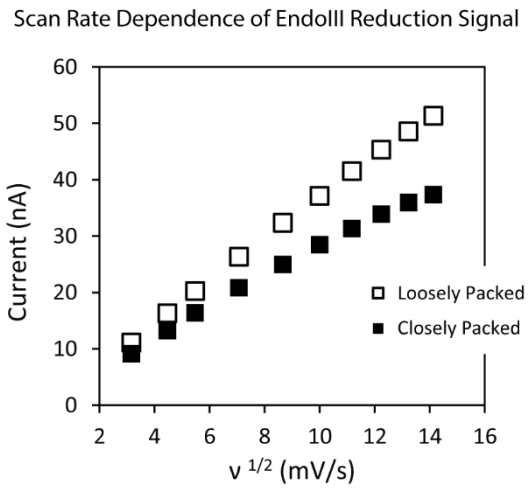

Figure 6. Kinetic analysis of the signal generated from EndoIII on differing DNA film morphologies is indicated. Cyclic voltammetry scans (scan rates ranging from 10 to 200 mV/s) of EndoIII were obtained in phosphate buffer (20 mM sodium phosphate, 100 mM NaCl, 0.5 mM EDTA, 20% glycerol, pH 7.4) for both closely (solid) and loosely (outlined) packed DNA monolayers. The reductive peak height for both morphologies, on the same multiplexed device, was quantified and plotted as a function of the square root of the scan rate, $\nu^{1/2}$. The nonlinearity of the signal from closely packed DNA films indicates that the signal is not diffusion-rate-limited.

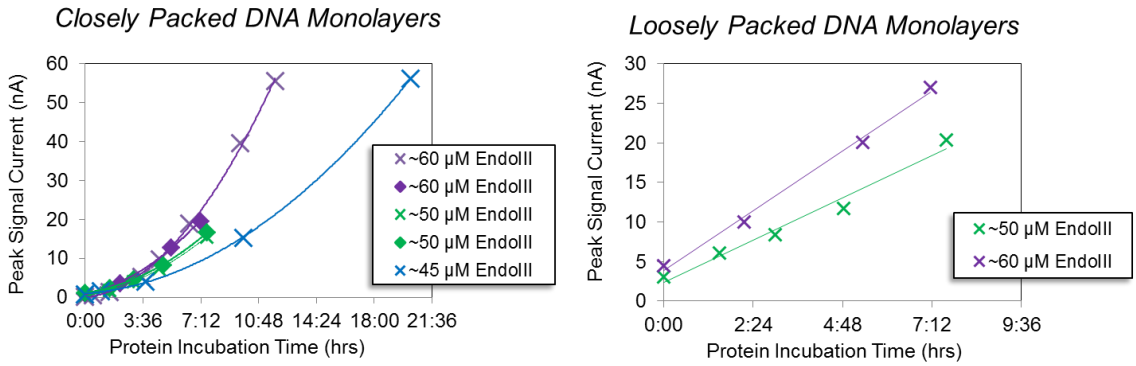

Figure 7. Signal accumulation of EndoIII as a function of time at various concentrations on both closely and loosely packed dsDNA monolayers formed in the presence and absence of 100 mM $MgCl_2$ during assembly, respectively. The peak signal current was quantified based on the reductive signal of EndoIII in the cyclic voltammaogram (scan rate = 100 mV/s) acquired in phosphate buffer (20 mM sodium phosphate, 100 mM NaCl, 0.5 mM EDTA, 20% glycerol, pH 7.4).

4.3.5 Multiplexed characterization of DNA CT proficiency

Since the electrochemical signal for the [4Fe-4S] cluster of EndoIII is generated primarily via DNA CT on closely packed dsDNA films, the DNA CT proficiency of a known disease-related mutant, Y82A, was compared to that of wild-type EndoIII using this morphology. The Y82A mutant of EndoIII has previously been shown to be DNA CT-deficient compared to wild-type EndoIII using individual DNA-modified electrodes (*21,22*). The DNA CT deficiency has been attributed to disruptions in the electron transport pathway from the DNA π-stack to the [4Fe-4S] cluster due to mutation of the aromatic tyrosine residue, located in close proximity to the π-stack based on the crystal structure of the wild-type protein bound to DNA (*36*). The quantification of the extent of DNA CT proficiency for [4Fe-4S] cluster proteins has proven to be challenging due to the variability between individual DNA-modified electrodes.

Multiplexed characterization of the wild-type (WT) and Y82A mutant EndoIII allows for a more quantitative comparison of the extent of coupling with the DNA-modified electrode. Multiplexed chips were assembled with half well-matched and half TC mismatched closely packed dsDNA films. Orthogonally, WT and Y82A EndoIII were added to two quadrants each, such that each protein was incubated on both well matched and TC-mismatch DNA-modified electrodes (Figure 8). Samples of equal protein concentration were prepared based on the absorption at 410 nm, reflecting the [4Fe-4S] cluster concentration for each protein (~70 μM). Using this multiplexed configuration, the reduction of the [4Fe-4S] cluster in both WT and Y82A mutant EndoIII was confirmed to

have been generated via DNA CT since both proteins displayed signal attenuation (23 ± 3%) upon introducing a TC mismatch. Furthermore, the signal from Y82A was 72 ± 5% attenuated compared to that of wild-type EndoIII. Taken together with the attenuation upon mismatch incorporation, the observation of decreased DNA-mediated signal intensity verifies that the Y82A mutation results in a deficiency in DNA CT. Circular dichroism (CD) thermal denaturation confirmed that the stability of the protein fold was relatively unaltered upon introducing the Y82A mutation (Figure 8). Upon fitting the thermal denaturation curves to a two-state unfolding model (*32*), melting temperatures for Y82A and WT EndoIII were found to be 49.2 ± 0.3 and 48.5 ± 0.3 °C, respectively.

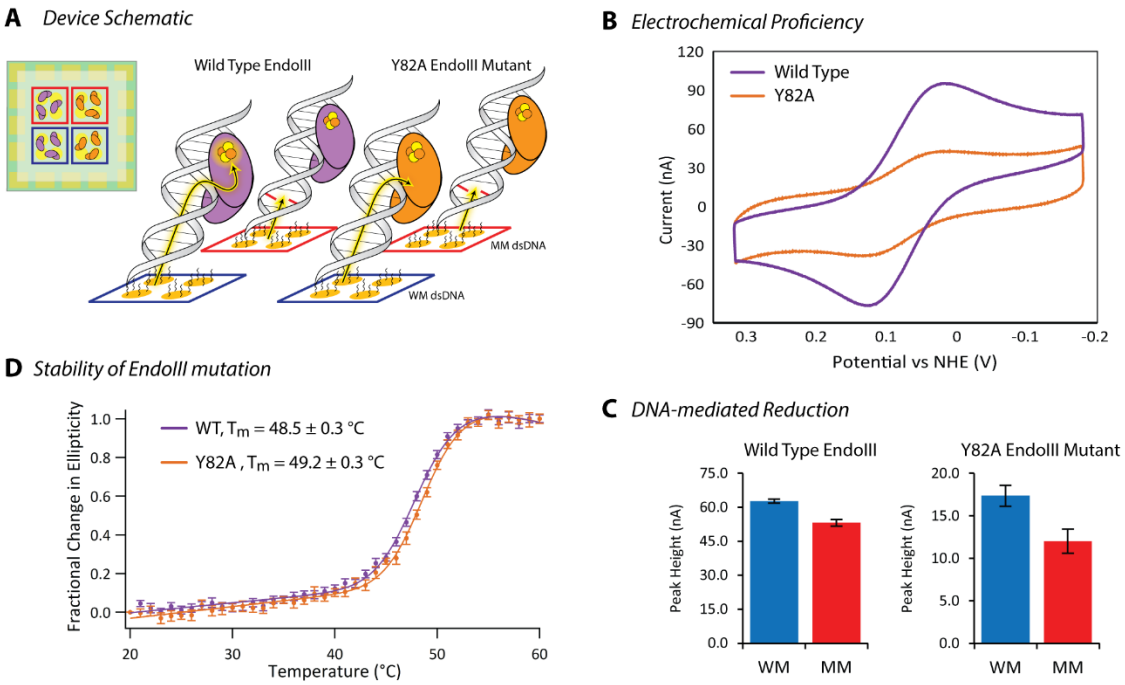

Figure 8. Comparison of the electrochemical properties and stability of wild-type EndoIII and a Y82A mutant. (*A*) Multiplexed electrode assembly schematic where electrodes are assembled with 100 mM $MgCl_2$, with either well-matched (blue) or TC-mismatched (red) duplex DNA, and then incubated with either wild-type (purple) or Y82A (orange) EndoIII (70 µM, based on absorbance at 410 nm). (*B*) Cyclic voltammetry (scan rate = 100 mV/s) in phosphate buffer (20 mM sodium phosphate, 100 mM NaCl, 0.5 mM EDTA, 20% glycerol, pH 7.4) are indicated for both wild-type and Y82A EndoIII on closely packed, well-matched DNA monolayers. (*C*) Reductive signal upon introducing a TC mismatch (red) compared to well-matched (blue) validates the mechanism of reduction to be DNA-mediated for both proteins. (*D*) Circular dichroism thermal denaturation (5 µM protein) validates that the Y82A mutation does not significantly alter the stability of the protein.

4.3.6 Direct comparison of electrostatic EndoIII mutants

Finally, the multiplexed DNA-modified electrodes were harnessed for the characterization of a new family of EndoIII mutants relative to wild-type protein. In designing this new family of EndoIII mutants, only residues that were unlikely to cause significant changes in the DNA binding affinity of EndoIII were chosen. Specifically, no residues in the conserved DNA binding FCL motif (*37*), residues Thr186 to Cys194, were mutated. The glycosylase activity of these mutants was verified to be equal to that of wild-type protein (Figure 9), so that the observed electrochemical differences cannot be attributed to deficiencies in DNA binding. The Y205H, K208E, and E200K EndoIII mutations investigated were originally designed to explore a possible shift in the midpoint potential of the [4Fe-4S] cluster since these mutations alter the electrostatics surrounding the cluster. However, as can be seen in Figure 10, when compared in parallel on a single multiplexed chip on a closely packed dsDNA film, the midpoint potential of all the mutants are not found to be statistically different, ±10 mV of the WT protein (Figure 10). Likely, the electrostatic effects of the DNA polyanion along with the associated counterions mitigate any effects of local electrostatic changes of nearby peptides.

Interestingly, despite the lack of difference in midpoint potential, large differences in signal intensity between the mutants relative to WT were observed when the electrochemistry of the proteins was assayed at equivalent concentrations based on the absorbance of the [4Fe-4S] cluster at 410 nm, which are statistically significant with 95% confidence based on a two-tailed *t* test. E200K yields a reductive current of 14.8 ±

0.3 nA in the cyclic voltammogram and is seen to be CT-deficient relative to WT EndoIII which displays a current intensity of 24.4 ± 0.8 nA. In contrast, K208E and Y205H exhibit significantly larger signals, 56.5 ± 2 and 118 ± 6 nA, respectively, relative to the WT protein.

To explore these significant differences, CD thermal denaturation experiments were performed. The melting temperatures for the Y205H, K208E, and E200K EndoIII as well as wildtype protein (5 μM) are 45.0 ± 0.3, 45.3 ± 0.3, 49.3 ± 0.3, and 48.5 ± 0.3 °C, respectively (Figure 10). The denaturation temperature of these EndoIII mutants correlates with the electrochemical signal size. Those that show a thermal stability that is reduced relative to the wild-type protein show a significantly higher signal size electrochemically. Conversely, E200K is slightly stabilized relative to the wild-type protein and displays an attenuated electrochemical signal. For all proteins, the signal initially grows with time and subsequently diminishes over extended incubation times. This signal decrease with time correlates with the thermal stability of the proteins; those proteins that are thermally destabilized diminish faster, while the signal persists for more stable proteins (Figure 11). Notably, the Y205H mutation, which is involved in hydrogen bonding to the [4Fe-4S] cluster, is found to be the most proficient in DNA CT, with a 5-fold larger signal than wild-type and the least stable mutant by both electrochemical measurements and CD thermal denaturation.

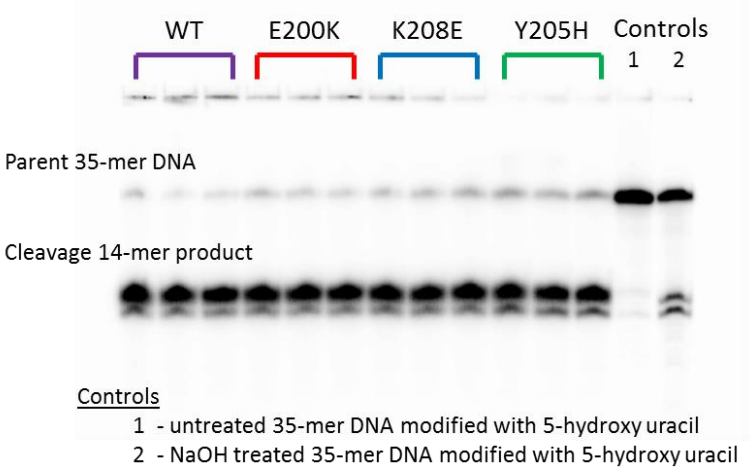

Mutant	% Activity Compared to WT
E200K	98.0 ± 1.5
K208E	95.8 ± 1.8
Y205H	91.6 ± 2.1

Figure 9. Enzymatic assay for EndoIII glycosylase activity. Glycosylase activity was determined for each mutant (Y205H, K208E, and E200K) compared to wild type EndoIII based on previously established methods (*22*). For this assay, protein samples (1 μM) were incubated for 15 min at 37°C with 5′-^{32}P-radiolabeled 35-mer duplex DNA (100 nM) modified with 5-hydroxy uracil, a substrate for EndoIII, in 10 mM Tris HCl, 1 mM EDTA, 50 mM NaCl, pH 7.6. Reactions were then quenched by adding of 1 M NaOH to a final concentration of 100 mM NaOH, dried, and electrophoresed through 20% denaturing PAGE at 90 W for 1.5 hours. Glycosylase activity of EndoIII results in the appearance of the 14-mer cleavage product in the denaturing gel. The glycosylase activity was determined as the fraction of 14-mer product observed relative to the total quantity of DNA and the percent activity compared to WT (purple) was then calculated for Y205H (green), K208E (blue), and E200K (red). Two control lanes containing the 35-mer duplexed DNA, yet lacking the enzymatic protein, were either untreated or treated with the 1 M NaOH.

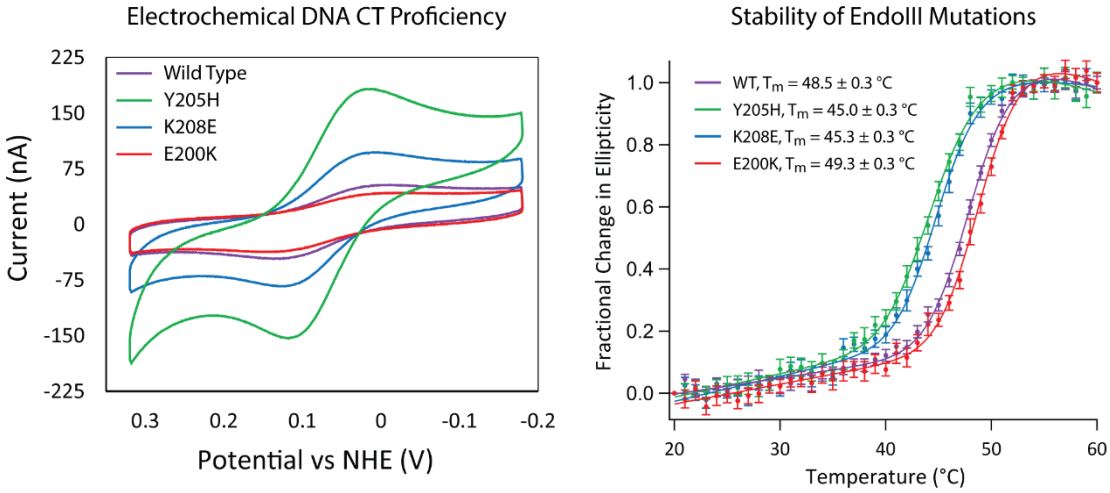

Figure 10. Electrochemical and stability comparison of a new family of electrostatic EndoIII mutations, Y205H (green), K208E (blue), and E200K (red), with wild-type EndoIII (purple). (*Left*) Cyclic voltammetry (scan rate = 100 mV/s) in phosphate buffer (20 mM sodium phosphate, 100 mM NaCl, 0.5 mM EDTA, 20% glycerol, pH 7.4) is displayed for all four proteins on closely packed (assembled with 100 mM $MgCl_2$), well-matched DNA monolayers. Protein samples had equivalent concentrations of [4Fe-4S] (70 µM based on the 410 nm absorbance). (*Right*) Circular dichroism thermal denaturation (5 µM protein) was performed to correlate the altered electronic coupling of these mutations in close proximity of the [4Fe-4S] cluster with the differential stability of the proteins.

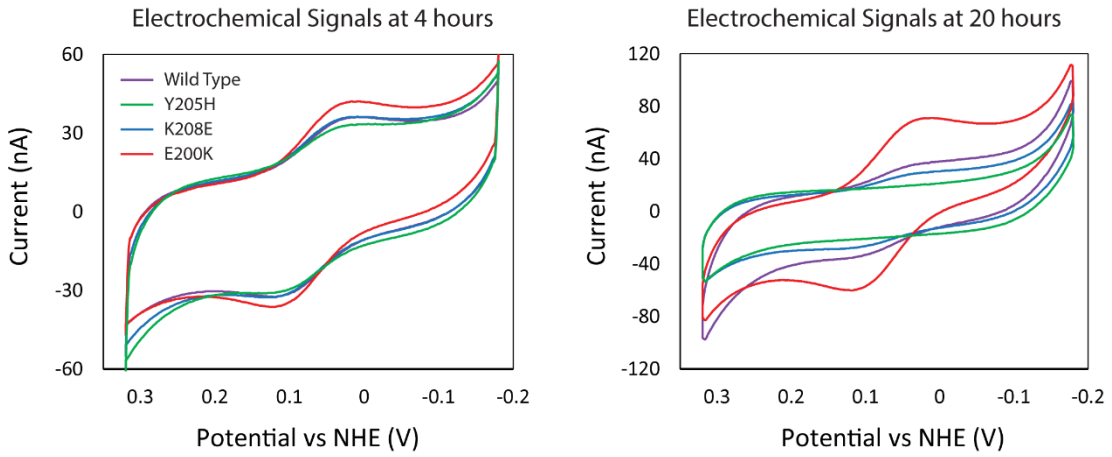

Figure 11. Electrochemical stability of EndoIII mutants. (*Left*) Protein concentrations were normalized for electrochemistry coupling to yield approximately equivalent signal sizes at early time points (~4 hours). Cyclic voltammetry (scan rate = 100 mV/s) acquired in phosphate buffer (20 mM sodium phosphate, 100 mM NaCl, 0.5 mM EDTA, 20% glycerol, pH 7.4) for wild type (purple), Y205H (green), K208E (blue), and E200K (red) EndoIII are presented. (*Right*) After extended incubation (~20 hours) on the multiplexed chip, the electrochemical signal from the electrostatic EndoIII mutants and wild type protein diminished based on their CVs. The degree of signal loss directly correlates with the stability and DNA CT proficiency of the proteins, with the remaining signal size decreasing in the following order: E200K (red), wild type (purple), K208E (blue), and finally Y205H (green), which had no discernible signal remaining.

4.4 Discussion

4.4.1 Multiplexed electrochemical analysis of EndoIII

In this study, the redox activity of the [4Fe-4S] cluster of EndoIII upon DNA binding was investigated using multiplexed DNA-modified electrodes. The utility of multiplexed analysis has previously been illustrated in using DNA-modified electrodes for the detection of biomarkers (*3-11*) as well as in performing sensitive measurements of DNA CT on long DNA duplexes (*14*). As there is growing interest in understanding of the redox properties of proteins containing [4Fe-4S] clusters that are involved in genome maintenance, the extension of multiplexed analysis has become essential to investigate these complex proteins and their subtle differences in redox behavior.

The electrochemical signal of EndoIII obtained using multiplexed DNA-modified electrodes was shown to be comparable to that seen using individual DNA-modified electrodes (*20-22*). Differences in peak potential and signal size are difficult to compare on individual electrodes given the variability in DNA-modified surfaces among experiments. The complexity of protein samples further amplifies this variability. Multiplexing removes the variability associated with protein preparation and surface modification. Specifically, multiplexing allows, with confidence, for a given protein to be examined in parallel across different DNA substrates or for many proteins to be compared on a given DNA substrate. Thus, by harnessing this ability to probe in parallel for subtle differences in the electrochemical signal of EndoIII, effects of DNA substrate and morphology can be elucidated.

4.4.2 Mechanistic insights into EndoIII electrochemistry

Multiplexed analysis of the $3^{+}/2^{+}$ redox couple of EndoIII on differing DNA morphologies shows subtle differences in the DNA-bound electrochemical signals. These differences in electrochemistry result from differences in electron transfer pathways between the electrode and DNA-bound EndoIII that vary as a function of DNA film morphology. DNA-modified electrodes with single-stranded DNA, first, are found to function as an ideal control. Since EndoIII does not bind single-stranded DNA with high affinity, the single-stranded DNA does not serve as a means to increase the local concentration of EndoIII at the electrode surface. Moreover, it appears that the negatively charged single-stranded DNA serves as an effective passivation layer, preventing protein denaturation on the gold surface, a common occurrence for protein electrochemistry (*38*). Instead, EndoIII appears to be electrochemically silent on these electrodes modified with single-stranded DNA.

Second, the duplex DNA film morphology, established during electrode assembly, is demonstrated to be critical in dictating the predominant electron transfer pathway between the electrode surface and the [4Fe-4S] cluster of DNA-bound EndoIII. Differing electron transfer pathways to a single DNA-bound redox-active moiety were previously characterized using DNA-modified electrodes with covalent redox-active reporters (*14,35*). In the case of a DNA-bound redox-active reporter, such as DNA-tethered methylene blue, it has been shown that the accessibility of the redox-active moiety to the electrode surface determines whether the predominant reduction mechanism is DNA CT or direct reduction by the surface of the electrode (*35*). In the case of the DNA-mediated reduction, we have

established that the rate-limiting step for the DNA-mediated reduction of distally bound redox-active species is not DNA CT, but tunneling through the alkane thiol linkage to the electrode (*39*). The lateral charge diffusion through these DNA-modified films has also been established to be quite slow, negating the possibility of cross-talk throughout these films (*40*). The redox activity of EndoIII on DNA-modified electrodes assembled with closely packed DNA monolayers, with limited surface accessibility, display all the previously established hallmarks of a DNA-mediated reduction pathway, including increased peak splitting, signal broadening, sensitivity to perturbations, and non-diffusion-rate-limited kinetics. Conversely, the DNA-bound electrochemical signal from EndoIII on loosely packed DNA films, which have enhanced surface accessibility, display the opposite electrochemical behaviors that are characteristic of an electron transfer pathway that is not DNA-mediated. As both these signals involve reduction of DNA-bound EndoIII, the signals display only subtle differences. Only by using multiplexed analysis to investigate the electrochemistry of a single protein solution in parallel across differing DNA-modified electrodes are these two different electron transfer pathways cleanly distinguishable.

4.4.3 Electron transfer in EndoIII mutants

Multiplexed analysis was demonstrated to be useful not only in the characterization of different electron transfer pathways from the electrode surface to the DNA-bound EndoIII but also in comparing directly the electron transfer efficiencies of different EndoIII mutants. As proof-of-principle, the DNA CT proficiency of a known disease-related EndoIII mutant, Y82A, was electrochemically compared to wild-type EndoIII. It has

previously been established that introducing the Y82A mutation into EndoIII yields a functionally active protein that is DNA CT-deficient (*21*). Due to the proximity of this aromatic tyrosine residue to the DNA π-stack, the deficiencies in the electrochemical signal have been attributed to disrupting the electron transfer pathway between the DNA and [4Fe-4S] cluster (*21*). Our multiplexed experiment allowed for the validation of this result along with a more quantitative assessment of CT deficiency.

The mechanism of reduction for both wild-type and Y82A EndoIII was shown to be DNA-mediated on the closely packed DNA films since both proteins display the characteristic sensitivity to single base pair perturbations. The inherent DNA CT deficiency of Y82A was characterized in parallel so that the difference in electrochemical efficiency of Y82A bound to DNA compared to wild-type can be conclusively attributed to decreased DNA CT proficiency. The degree of DNA CT deficiency quantified for this mutant was found to be twice as pronounced compared to previous measurements, given the overall decreased variability of the DNA-modified electrodes and, importantly, the decreased contributions from surface reduction of the [4Fe-4S] cluster due to the optimized DNA morphology.

Moreover, this multiplexed technology is sufficiently reliable to permit characterization of the effects on the electron transfer pathway of a new family of EndoIII mutations. This family was found to show significant differences in DNA CT efficiency, while displaying very similar DNA-bound reduction potentials for the $3^{+}/2^{+}$ redox couple of the [4Fe-4S]. Key to conclusively attributing differences, or lack thereof, observed in the

mutant electrochemistry to changes in the electron transfer pathway through EndoIII was the ability to perform this comparison on identical gold surfaces, allowing for the geometry of electron transfer between the electrode and EndoIII to be held constant.

Previous work by Burgess and co-workers that focused on changing the electrostatics in *Azotobacter vinelandii* ferredoxin I resulted in large potential shifts; a single phenylalanine to histidine mutation caused a shift of over 200 mV for the [4Fe-4S] cluster while leaving the overall protein structure unaffected (*41*). With the same aims, EndoIII mutations were prepared that invert the electrostatics of three residues within 4 Å of the [4Fe-4S] cluster that are oriented on the opposite face of the cluster relative to the DNA. Multiplexed analysis of these three different EndoIII mutants allowed for their simultaneous comparison to wild-type EndoIII. The lack of distinguishable differences of the DNA-bound midpoint potentials for these electrostatic EndoIII mutants likely reflects the overwhelming contribution of polyanionic DNA, as DNA binding already negatively shifts the reduction potential of EndoIII by approximately 200 mV (*25*). The strict consistency of the measured DNA-bound midpoint potentials likely further derives from the screening effect of counterions associated with the DNA, as well as from the broad, heterogeneous nature of the observed DNA-mediated signals.

As mentioned above, we have proposed a model where DNA repair proteins containing [4Fe-4S] clusters utilize DNA CT as a first step to localize to the vicinity of DNA damage (*21*). All of the proteins that we have investigated thus far have similar DNA-bound reduction potentials of approximately 80 mV vs NHE (*20*). These results suggest that DNA

binding could be a mechanism that standardizes the reduction potentials of iron-sulfur cluster-containing DNA repair proteins once bound to DNA, allowing for efficient DNA-mediated electron self-exchange between repair proteins.

Unlike the Y82A mutation, these mutations were specifically designed to affect residues in close proximity to the [4Fe-4S] cluster but presumably without affecting the pathway for DNA-mediated electron transfer (Figure 12). Nonetheless, as seen in Figure 10, these changes unambiguously result in significant changes in the DNA CT efficiency. Multiplexed electrochemical characterization in conjunction with thermal denaturation circular dichroism experiments indicates that the differences in DNA CT efficiencies of these mutants are most likely caused by changes in the stability and solvent accessibility of the [4Fe-4S] cluster. Those proteins with decreased thermal stability show increased DNA CT yield compared to WT. Structured water molecules have been proposed to mediate efficient biological electron transfer in several intra- (*42,43*) and intermolecular protein systems (*44-46*), generally by forming robust hydrogen-bonding pathways that increase electronic coupling between the donor and acceptor (*47*). We hypothesize that the destabilization we observe in Y205H and K208E EndoIII may result in the formation of a water pocket in EndoIII that would facilitate ET, as we have suggested previously for other destabilizing EndoIII mutations (*22*). In the case of E200K, which is slightly stabilized relative to wild-type, substitution for a larger lysine residue along the face of the cluster may instead screen the cluster from the solvent and contribute to the observed CT deficiency. While the Y82A mutant is marginally stabilized compared to WT EndoIII, it is more significantly defective in

DNA CT proficiency compared to E200K. Therefore, the extent the DNA CT deficiency of Y82A cannot be fully attributed to the change in stability and is thought to originate from directly disrupting the electron transfer pathway. Overall, it appears that differences in DNA CT proficiency can be caused both by altering the electron transfer pathway by removing aromatics and also by more indirectly modulating the electronic coupling of the cluster by changing protein stability and presumably solvent accessibility.

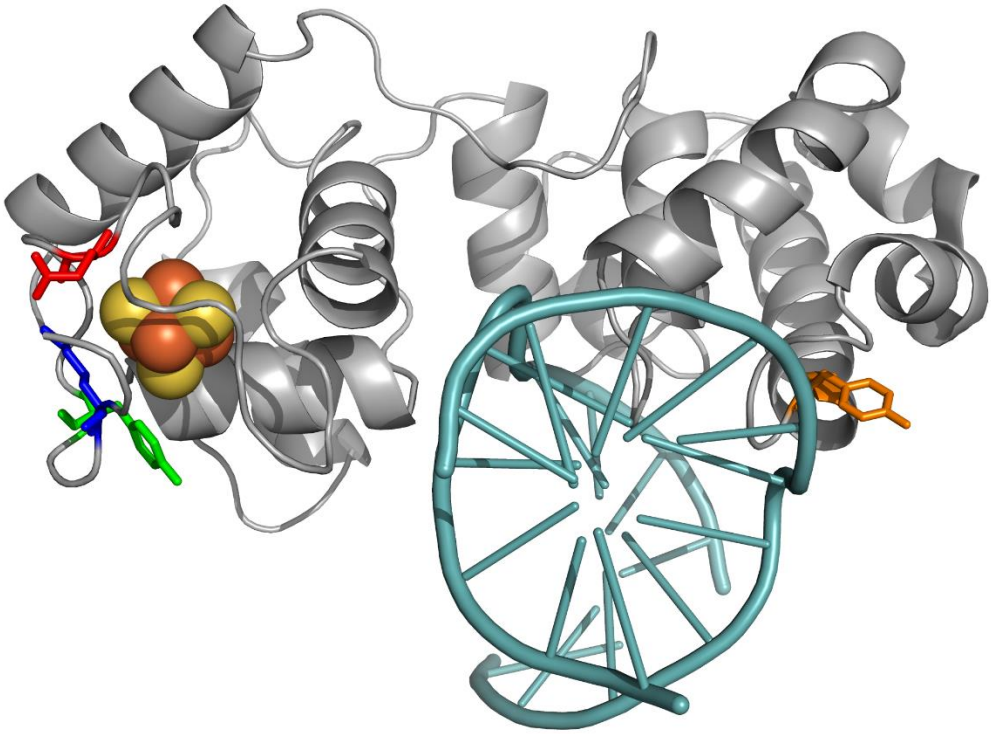

Figure 12. Crystal structure of EndoIII with the location of mutants shown relative to the DNA (cyan) and [4Fe-4S] cluster: Y205 (green), K208 (blue), E200 (red), and Y82 (orange). PDB: 2ABK with DNA from 1ORN.

4.5 Conclusions

Multiplexed characterization of the DNA repair protein EndoIII bound to DNA provides new insights into the DNA-mediated reduction of this metalloprotein and the resolution of subtle electrochemical variations associated with DNA substrate and surface morphology. Multiplexed analysis leads to more reliable statistics as well as decreased surface variability and background contribution. The reduction of EndoIII is seen to be DNA-dependent, yet once bound to duplex DNA, there are two different pathways through which the electron transfer proceeds. The predominant mechanism for the reduction of the [4Fe-4S] cluster of EndoIII is shown to correlate with the surface accessibility of the protein, resulting in DNA-mediated reduction being observed only with closely packed DNA films. In addition to the electron transfer pathway between the electrode surface and EndoIII being characterized, the use of multiplexed analysis also allowed for the direct comparison of electron transfer pathways through the protein itself. The electrochemistry and stability of various EndoIII mutants was characterized, including a new family of mutations introducing electrostatic changes in close proximity to the [4Fe-4S] cluster. The stability of a given mutation was shown to correlate with the electrochemical yield, leading to the hypothesis that mutations not directly on the electron transfer pathway through the protein can alter the rate of electron transfer by affecting the solvation surrounding the [4Fe-4S] cluster. Most interestingly, this side-by-side quantitative comparison of varying electrostatics in the protein fold provides a demonstration of the dominance that DNA binding elicits on the reduction potential of DNA repair proteins.

These multiplexed chips provide the needed flexibility and robustness to characterize the redox activity of emerging [4Fe-4S]-containing proteins that bind DNA. Multiplexed analysis will be integral in relating the function and redox activity of these DNA binding proteins in order to establish roles for these critical redox-active cofactors *in vivo*.

References

1. Zheng, G.; Patolsky, F.; Cui, Y.; Wang, U.W.; Lieber, C.M. Multiplexed electrical detection of cancer markers with nanowire sensor arrays. *Nat. Biotechnol.* **2005**, *23*, 1294-1301.

2. Morrow, T.J.; Li, M.; Kim, J.; Mayer, T.S.; Keating, C.D. Programmed assembly of DNA-coated nanowire devices. *Science* **2009**, *323*, 352.

3. Swensen, J.S.; Xiao, Y.; Ferguson, B.S.; Lubin, A.A.; Lai, R.Y.; Heeger, A.J.; Plaxco, K.W.; Soh, H.T. Continuous, real-time monitoring of cocaine in undiluted blood serum via a microfluidic, electrochemical aptamer-based sensor. *J. Am. Chem. Soc.* **2009**, *131*, 4262-4266.

4. Plaxco, K.W.; Soh, H.T. Switch-based biosensors: a new approach towards real-time, *in vivo* molecular detection. *Trends Biotechnol.* **2011**, *29*, 1-5.

5. Bonham, A.J.; Hsieh, K.; Ferguson, B.S.; Vallee-Belisle, A.; Ricci, F.; Soh, H.T.; Plaxco, K.W. Quantification of transcription factor binding in cell extracts using an electrochemical, structure-switching biosensor. *J. Am. Chem. Soc.* **2012**, *134*, 3346-3348.

6. White, R.J.; Kallewaard, H.M.; Hsieh, W.; Patterson, A.S.; Kasehagen, J.B.; Cash, K.J.; Uzawa, T.; Soh, H.T.; Plaxco, K.W. Wash-free, electrochemical platform for the quantitative, multiplexed detection of specific antibodies. *Anal. Chem.* **2012**, *84*, 1098-1103.

7. Hsieh, K.; Patterson, A.S.; Ferguson, B.S.; Plaxco, K.W.; Soh, H.T. Rapid, sensitive, and quantitative detection of pathogenic DNA at the point of care through microfluidic electrochemical quantitative loop-mediated isothermal amplification. *Angew. Chem. Int. Ed.* **2012**, *51*, 4896-4900.

8. Fang, Z.; Soleymani, L.; Pampalakis, G.; Yoshimoto, M.; Squire, J.A.; Sargent, E.H.; Kelley, S.O. Direct profiling of cancer biomarkers in tumor tissue using a multiplexed nanostructured microelectrode integrated circuit. *ACS Nano* **2009**, *3*, 3207-3213.

9. Vasilyeva, E.; Lam, B.; Fang, Z.; Minden, M.D.; Sargent, E.H.; Kelley, S.O. Direct genetic analysis of ten cancer cells: tuning sensor structure and molecular probe design for efficient mRNA capture. *Angew. Chem. Int. Ed.* **2011**, *50*, 4137-4141.

10. Lam, B.; Fang, Z.; Sargent, E.H.; Kelley, S.O. Polymerase chain reaction-free, sample-to-answer bacterial detection in 30 minutes with integrated cell lysis. *Anal. Chem.* **2012**, *84*, 21-25.

11. Das, J.; Cederquist, K.B.; Zaragoza, A.A.; Lee, P.E.; Sargent, E.H.; Kelley, S.O. An ultrasensitive universal detector based on neutralizer displacement. *Nat. Chem.* **2012**, *4*, 642-648.

12. Pheeney, C.G.; Guerra, L.F.; Barton, J.K. DNA sensing by electrocatalysis with hemoglobin. *Proc. Natl. Acad. Sci. USA* **2012**, *109*, 11528-11533.

13. Slinker, J.D.; Muren, N.B.; Gorodetsky, A.A.; Barton, J.K. Multiplexed DNA-modified electrodes. *J. Am. Chem. Soc.* **2010**, *132*, 2769-2774.

14. Slinker, J.D.; Muren, N.B.; Renfrew, S.E.; Barton, J.K. DNA charge transport over 34 nm. *Nat. Chem.* **2011**, *3*, 228-233.

15. Genereux, J.C.; Barton, J.K. Mechanisms for DNA charge transport. *Chem. Rev.* **2010**, *110*, 1642-1662.

16. Murphy, C.J.; Arkin, M.R.; Jenkins, Y.; Ghatlia, N.D.; Bossmann, S.H.; Turro, N.J.; Barton, J.K. Long range photoinduced electron transfer through a DNA helix. *Science* **1993**, *262*, 1025-1029.

17. *Charge Transfer in DNA: From Mechanism to Application*; Wagenknecht, H. A., Ed.; Wiley-VCH Verlag GmbH & Co KGaA: Weinheim, Germany, 2005.

18. Boon, E.M.; Ceres, D.M.; Drummond, T.G.; Hill, M.G.; Barton, J.K. Mutation detection by electrocatalysis at DNA-modified electrodes. *Nat. Biotechnol.* **2000**, *18*, 1096-1100.

19. Boal, A.K.; Barton, J.K. Electrochemical detection of lesions in DNA. *Bioconjugate Chem.* **2005**, *16*, 312-321.

20. Boal, A.K.; Yavin, E.; Lukianova, O.A.; O'Shea, V.L.; David, S.S.; Barton, J.K. DNA-bound redox activity of DNA repair glycosylases containing [4Fe-4S] clusters. *Biochemistry* **2005**, *44*, 8397-8407.

21. Boal, A.K.; Genereux, J.C.; Sontz, P.A.; Gralnick, J.A.; Newman, D.K.; Barton, J.K. Redox signaling between DNA repair proteins for efficient lesion detection *Proc. Natl. Acad. Sci. USA* **2009**, *106*, 15237-15242.

22. Romano, C.A; Sontz, P.A.; Barton, J.K. Mutants of the base excision repair glycosylase, Endonuclease III: DNA charge transport as a first step in lesion detection. *Biochemistry* **2011**, *50*, 6133-6145.

23. Lee, P.E.; Demple, B.; Barton, J.K. DNA-mediated redox signaling for transcriptional activation of SoxR. *Proc. Natl. Acad. Sci. USA* **2009**, *106*, 13164-13168.

24. Mui, T.P.; Fuss, J.O.; Ishida, J.P.; Tainer, J.A.; Barton, J.K. ATP-stimulated, DNA-mediated redox signaling by XPD, a DNA repair and transcription helicase. *J. Am. Chem. Soc.* **2011**, *133*, 16378-16381.

25. Gorodetsky, A.A.; Boal, A.K.; Barton, J.K. Direct electrochemistry of Endonuclease III in the presence and absence of DNA *J. Am. Chem. Soc.* **2006**, *128*, 12082-12083.

26. Wu, Y.; Suhasini, A.N.; Brosh, R.M., Jr. Welcome the family of FANCJ-like helicases to the block of genome stability maintenance proteins. *Cell. Mol. Life Sci*. **2009**, *66*, 1209-1222.

27. Vaithiyalingam, S.; Warren, E.M.; Eichman, B.F.; Chazin, W.J. Insights into eukaryotic DNA priming from the structure and functional interactions of the 4Fe-4S cluster domain of human DNA primase. *Proc. Natl. Acad. Sci. USA* **2010**, *107*, 13684-13689.

28. White, M.F.; Dillingham, M.S. Iron-sulphur clusters in nucleic acid processing enzymes. *Curr. Opin. Struct. Biol.* **2012**, *22*, 94-100.

29. Wu, Y.; Brosh, R.M., Jr. DNA helicase and helicase-nuclease enzymes with a conserved iron-sulfur cluster. *Nucleic Acids Res.* **2012**, *40*, 4247-4260.

30. Sontz, P.A.; Mui, T.P.; Fuss, J.O.; Tainer, J.A.; Barton, J.K. DNA charge transport as a first step in coordinating the detection of lesions by repair proteins. *Proc. Natl. Acad. Sci. USA* **2012***, 109*, 1856-1861.

31. Cunningham, R.P., Asahara, H., Bank, J.F., Scholes, C.P., Salerno, J.C., Surerus, K., Münck, E., McCracken, J., Peisach, J., and Emptage, M.H. Endonuclease III is an iron-sulfur protein. *Biochemistry* **1989**, *28*, 4450-4455.

32. Koepf, E.K.; Petrassi, H.M.; Sudol, M.; Kelly, J.W. WW: An isolated three-stranded antiparallel β-sheet domain that unfolds and refolds reversibly; evidence for a structured hydrophobic cluster in urea and GdnHCl and a disordered thermal unfolded state. *Protein Sci.* **1999**, *8*, 841-853.

33. Lapierre, M.A.; O'Keefe, M.; Taft, B.J.; Kelley, S.O. Electrocatalytic detection of pathogenic DNA sequences and antibiotic resistance markers. *Anal. Chem.* **2003**, *75*, 6327-6333.

34. Bard, A.J.; Faulkner, L.R. Electrochemical Methods: Fundamental and Application, 2nd ed.; John Wiley & Sons: New York, 2000; pp 580-631.

35. Pheeney, C.G.; Barton, J.K. DNA electrochemistry with tethered methylene blue. *Langmuir* **2012**, *28*, 7063-7070.

36. Fromme, J.C.; Verdine, G.L. Structure of a trapped endonuclease III-DNA covalent intermediate. *EMBO J.* **2003**, *22*, 3461-3471.

37. Thayer, M.M.; Ahern, H.; Xing, D.; Cunningham, R.P.; Tainer, J.A. Novel DNA binding motifs in the DNA repair enzyme endonuclease III crystal structure. *EMBO J.* **1995**, *14*, 4108-4120.

38. Zhang, J.; Chi, Q.; Hansen, A.G.; Jensen, P.S.; Salvatore, P.; Ulstrup, J. Interfacial electrochemical electron transfer in biology - towards the level of the single molecule. *FEBS Lett.* **2012**, *586*, 526-535.

39. Drummond, T.G.; Hill, M.G.; Barton, J.K. Electron transfer rates in DNA films as a function of tether length. *J. Am. Chem. Soc.* **2004**, *126*, 15010-15011.

40. Kelley, S.O.; Jackson, N.M.; Hill, M.G.; Barton, J.K. Long-range electron transfer through DNA films. *Angew. Chem. Int. Ed.* **1999**, *38*, 941-945.

41. Chen, K.; Bonagura, C.A.; Tilley, G.J.; McEvoy, J.P.; Jung, Y.S.; Armstrong, F.A.; Stout, C.D.; Burgess, B.K. Crystal structures of ferredoxin variants exhibiting large changes in [Fe-S] reduction potential. *Nat. Struct. Biol.* **2002**, *9*, 188-192.

42. Francisco, W.A.; Wille, G.; Smith, A.J.; Merkler, D.J.; Klinman, J.P. Investigation of the pathway for inter-copper electron transfer in peptidylglycine α-amidating monooxygenase. *J. Am. Chem. Soc.* **2004**, *126*, 13168-13169.

43. Casimiro, D.R.; Richards, J.H.; Winkler, J.R.; Gray, H.B. Electron transfer in ruthenium-modified cytochromes *c*. σ-tunneling pathways through aromatic residues. *J. Phys. Chem.* **1993**, *97*, 13073-13077.

44. Tezcan, F.A.; Crane, B.R.; Winkler, J.R.; Gray, H.B. Electron tunneling in protein crystals. *Proc. Natl. Acad. Sci. USA* **2001**, *98*, 5002-5006.

45. van Amsterdam, I.M.C.; Ubbink, M.; Einsle, O.; Messerschmidt, A.; Merli, A.; Cavazzini, D.; Rossi, G.L.; Canters, G.W. Dramatic modulation of electron transfer in protein complexes by crosslinking. *Nat. Struct. Biol.* **2002**, *9*, 48-52.

46. Miyashita, O.; Okamura, M.Y.; Onuchic, J.N. Interprotein electron transfer from cytochrome c_2 to photosynthetic reaction center: Tunneling across an aqueous interface. *Proc. Natl. Acad. Sci. USA* **2005**, *102*, 3558-3563.

47. Lin, J.; Balabin, I.A.; Beratan, D.N. The nature of aqueous tunneling pathways between electron-transfer proteins. *Science* **2005**, *310*, 1311-1313.

Chapter 5

Sulfur K-edge X-ray absorbance spectroscopy of the 4Fe4S cluster of Endonuclease III with DNA*

*Experiments done in collaboration with Yang Ha of the Solomon and Hodgson groups at Stanford University. A.R.A. prepared the samples; Y.H. measured samples and processed the data.

5.1 Introduction

Endonuclease III (EndoIII) is a glycosylase enzyme that excises oxidized pyrimidines as part of the base excision repair (BER) pathway in order to maintain the integrity of genomic DNA (*1*). EndoIII contains a $[4Fe4S]^{2+}$ cluster as-isolated (Figure 1) that is relatively insensitive to reduction and oxidation in solution (*2*), leading to a proposed structural role for the cluster although it is not required for folding or stability in the homologous BER enzyme MutY (*3*). However, we have found electrochemically that the redox potential of the EndoIII cluster shifts upon DNA binding (*4*). Here, we form DNA monolayers on electrode surfaces and then monitor the electrochemistry of a DNA-bound redox probe through DNA charge transport (CT). In this process, charge is funneled from the electrode surface through the π-stack of the DNA bases to reach the redox probe, which must be electronically coupled to the DNA π-stack (*5*). The redox probe can be an intercalating organic dye, such as nile blue or methylene blue, or a redox-active DNA-binding protein (*5*).

Specifically, we have measured the electrochemistry of *E. coli* EndoIII on highly ordered pyrolytic graphite (HOPG) electrodes that were either bare or modified with mixed-sequence 15-mer DNA. When EndoIII was investigated on a bare HOPG electrode, two signals were observed: an irreversible anodic peak at 250 mV and a cathodic peak at -300 mV, assigned to the $[4Fe4S]^{3+/2+}$ and $[4Fe4S]^{2+/1+}$ couples, respectively (*4*). Conversely, on DNA-modified HOPG electrodes, a single redox couple with a midpoint potential of 20 mV versus NHE was observed. This quasi-reversible redox signal was assigned to the $[4Fe4S]^{3+/2+}$

couple of EndoIII. A similar midpoint potential was observed on DNA-modified gold electrodes (*6*). Thus according to these electrochemistry results, DNA binding of EndoIII negatively shifts the $[4Fe4S]^{3+/2+}$ redox potential of the cluster by at least 200 mV, activating the cluster towards oxidation (*4*). Generally, the redox potential of iron-sulfur clusters is sensitive to the protein environment, with the major factors being solvent accessibility, hydrogen bonding, and electrostatics (*7*). The factors most likely involved in the negative shift in potential of the 4Fe4S cluster of EndoIII upon DNA binding are: (*i*) a more buried, less solvent-accessible cluster environment, and (*ii*) the electrostatics of the DNA poly-anion. The redox potential of DNA-bound EndoIII is high potential iron-sulfur protein (HiPIP)-like, given that the $[4Fe4S]^{3+/2+}$ couple has been shifted into a physiologically relevant range (*6*).

Other DNA processing enzymes have been discovered with similar DNA-bound $[4Fe4S]^{3+/2+}$ redox potentials of approximately 80 mV versus NHE. These include the BER proteins MutY and UDG (*6*), the nucleotide excision repair helicase XPD (*8*), and the helicase DinG shown to be involved in R-loop maturation (*9*). Additionally, because significant conformational changes do not occur upon the DNA binding of EndoIII, a thermodynamic consequence of the approximately 200 mV negative shift in redox potential is that the oxidized, $[4Fe4S]^{3+}$, form of EndoIII has a much higher affinity for DNA (3 orders of magnitude) than the reduced, $[4Fe4S]^{2+}$, form (*4*). Combined with the fast kinetics of DNA CT (picoseconds) (*10*), these observations suggested a model whereby these often low-copy number enzymes could use DNA CT to cooperate inside cells to efficiently localize

to the vicinity of lesions (*11*). Essentially, this proposed model consists of long-distance DNA-mediated electron transfer self-exchange reactions between two 4Fe4S cluster proteins with similar DNA-bound redox potentials. When the DNA intervening between the two proteins is undamaged, the self-exchange reaction can proceed efficiently, with the result that one of the DNA-bound proteins is reduced and its affinity for DNA lowered. This protein can then diffuse to another region of the genome. However, in the case of an intervening mismatch or lesion that disrupts π-stacking and attenuates DNA CT, this self-exchange reaction is inhibited. Both proteins would remain bound to the DNA in the vicinity of the lesion, significantly reducing the range over which the slower process of diffusion must occur.

While we have shown the redox potential shift of the 4Fe4S cluster of EndoIII upon DNA binding electrochemically, these experiments do not provide direct molecular evidence for the species being observed. The goal of this work is to use spectroscopic methods to directly monitor changes in the iron-sulfur cluster upon DNA binding in order to obtain this direct molecular evidence for the redox potential shift. X-ray absorbance spectroscopy (XAS) has proven to be a powerful method to monitor iron-sulfur clusters in different environments (*12*).

In XAS, high-intensity X-rays are used to selectively excite core electron transitions for specific atoms (*13*). The excitation is selective because the energies required for core electronic transitions are particular to individual atoms. When the X-ray energy matches or exceeds the binding energy of a core electron, the electron is promoted to unpopulated

energy levels or dissociated, creating a sharp absorption edge feature (Figure 2). Analysis of different regions of the X-ray absorption spectrum yields different types of information. XANES (X-ray Absorption Near Edge Structure) refers to energy range immediately before and after the excitation edge, and can provide information on the electronics and geometry of an absorbing atom, such as oxidation state, covalency, and site symmetry. EXAFS (Extended X-ray Absorption Fine Structure) refers to the energy range above the absorption edge, where the ejected electron behaves as a photoelectron wave with a sinusoidal oscillation. EXAFS can provide geometric information, and is particularly known for delivering highly accurate metal-ligand bond lengths, with an accuracy of 0.01-0.02 Å (*13*). Edges are named according to the orbital from which an electron is excited: K-edge refers to the excitation of 1s core electrons, while L-edge refers to excitation from the 2s orbital.

Rather than excitation into the continuum (dissociation), lower energy pre-edge transitions are also possible in XAS. Solomon *et al.* have demonstrated that a pre-edge feature in sulfur K-edge XANES can provide valuable information about the electronic structure of 4Fe4S clusters (*14*). The edge transition in sulfur K-edge spectra corresponds to sulfur 1s → 4p excitation. In iron-sulfur clusters, a lower energy sulfur 1s (S_{1s}) to Fe-based 3d (Fe_{3d}) transition is possible, but is electric-dipole disallowed as a *gerade* (*g*) → *g* transition. However, the sulfur 1s → sulfur 3p transition is electric-dipole allowed as a *g* → *ungerade* transition. Therefore, if sulfur 3p orbitals mix with Fe 3d orbitals, the pre-edge transition (S_{1s} → Fe_{3d}) becomes partially allowed and gains intensity. This Fe-S covalency can be quantified as the area under the pre-edge transition. In this way, the intensity of the pre-

edge feature at 2470 eV in sulfur K-edge XAS spectra (Figure 2) is a direct measure of the Fe-S covalency in iron-sulfur clusters (*14*).

Solomon *et al.* have used the intensity of the pre-edge feature in sulfur K-edge XANES to study the origin of electronic differences between HiPIPs, which are generally more buried within the protein fold, and ferredoxins, where the clusters are typically more solvent-accessible (*14*). HiPIPs, where the $[4Fe4S]^{3+/2+}$ redox couple is physiologically accessible, show higher intensity of the pre-edge feature, indicating greater Fe-S covalency, than ferredoxins, where the $[4Fe4S]^{2+/+}$ couple is accessible. Hydration was found to be a major determinant of Fe-S covalency, whereas hydrogen bonding from the peptide backbone has a relatively small effect. When a ferredoxin was lyophilized, removing solvent waters, the Fe-S covalency increases significantly, whereas when the protein fold of a HiPIP was denatured, making the cluster more solvent accessible, the covalency decreases (*14*). Solomon *et al.* conclude that the electrostatic effect of water hydrogen-bonding to sulfur ligands decreases Fe-S covalency, weakening Fe-S bonds, and destabilizing the oxidized state of the cluster. Thus ferredoxins (HiPIPs), with their lower (higher) Fe-S covalencies, are prone to reduction (oxidation) at physiological potentials. In addition to the effect of local hydrogen-bonding, the remaining contribution to the observed potentials is proposed to derive from non-local electrostatics.

Furthermore, a series of model $[Fe_4S_4(SR)_4]^{2-}$ complexes with different thiolate ligands (R) was prepared and their sulfur K-edge XAS and electrochemistry measured (*14*). Plotting the Fe-S covalency versus the $[Fe_4S_4]^{3+/2+}$ oxidation potential revealed a linear

correlation (Figure 3). The positive slope indicates that with increasing covalency, the $[Fe_4S_4]^{2+}$ cluster is more easily oxidized. This would in turn correspond to a lower $[Fe_4S_4]^{3+/2+}$ redox potential. Overall, this study showed that the Fe-S covalency measured by XAS is able to quantitatively probe the electrostatic environment of iron-sulfur clusters (*14*).

Here, we use sulfur K-edge XANES to measure the Fe-S covalency of the 4Fe4S cluster of WT *E. coli* EndoIII alone and in the presence of DNA, both in solution and in lyophilized samples. We correlate the changes in covalency with a shift in redox potential, in order to obtain molecular evidence for the decrease in redox potential upon DNA binding that was observed electrochemically. An increase in Fe-S covalency would be expected upon the DNA binding of EndoIII.

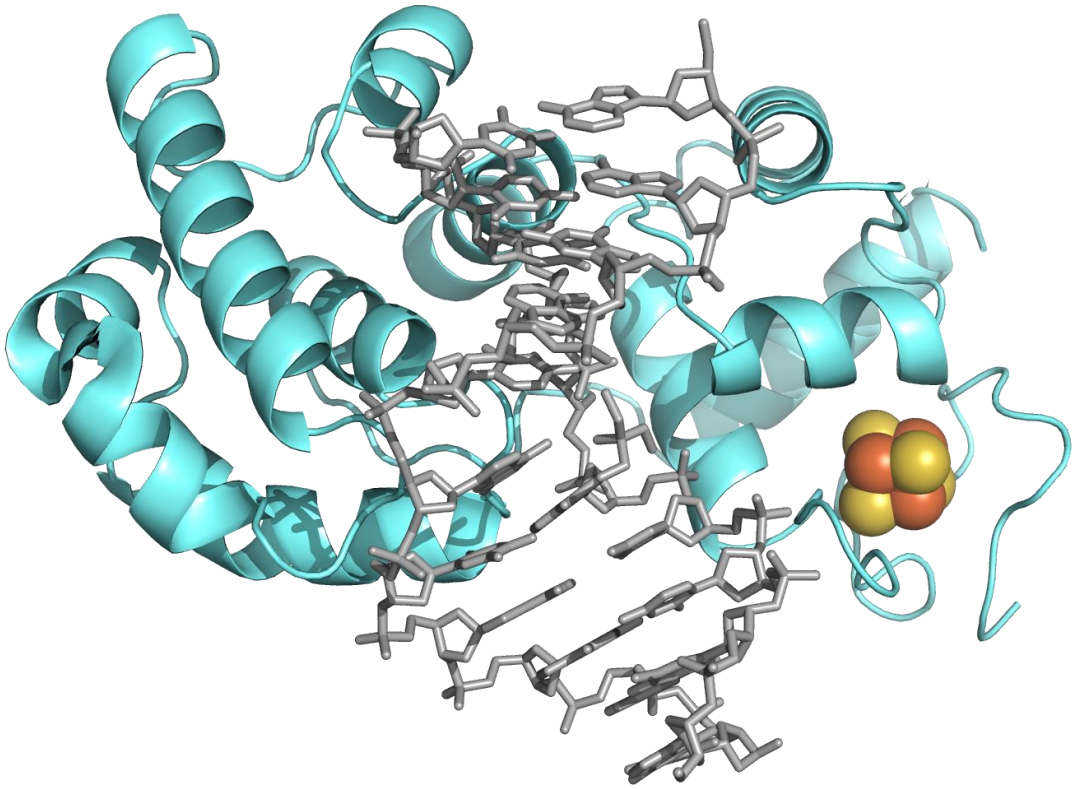

Figure 1. Crystal structure of the 4Fe4S cluster-containing base excision repair protein Endonuclease III bound to DNA. PDB: 2ABK with DNA from 1ORN. References: Thayer, M.M. et al. *EMBO J.* **1995**, *14*, 4108-4120; Fromme, J.C. et al. *EMBO J.* **2003**, *22*, 3461-3471.

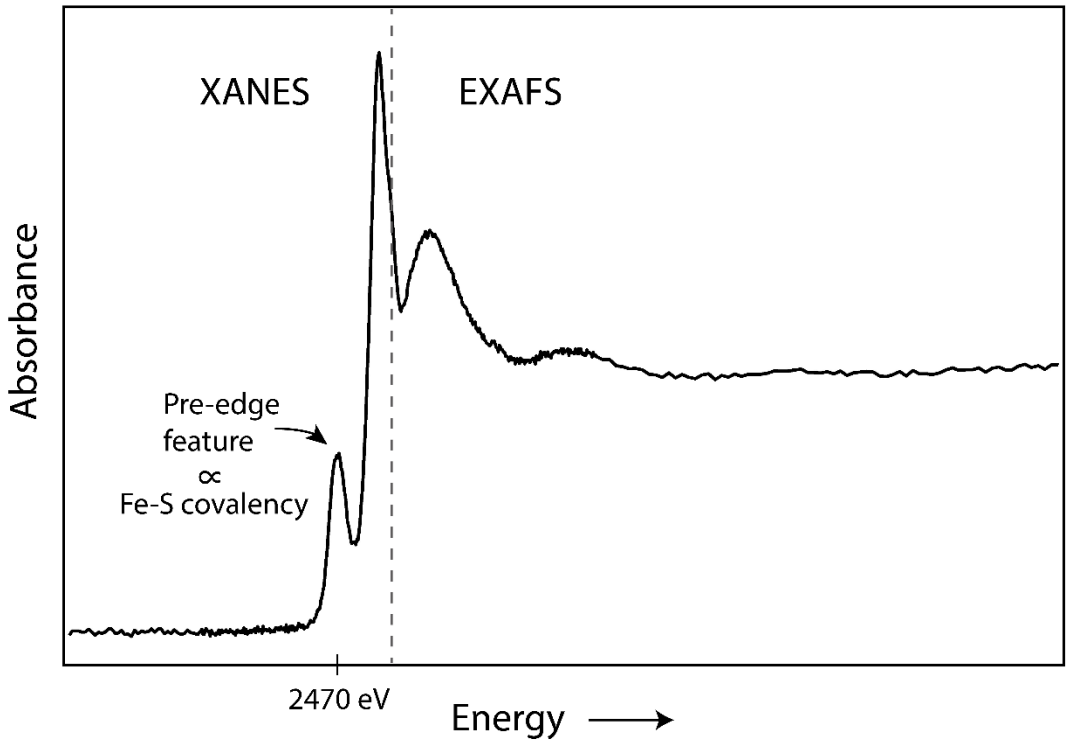

Figure 2. Sulfur K-edge X-ray absorbance spectra showing sharp absorption edge that appears with increasing X-ray energy. XANES refers to the energy range around the absorption edge, whereas EXAFS focuses on the oscillations of the ejected electron at higher energies. The spectra of EndoIII in solution is shown. The intensity of the pre-edge feature at 2470 eV is proportional to the Fe-S covalency of 4Fe4S clusters, which can be correlated to their redox potential.

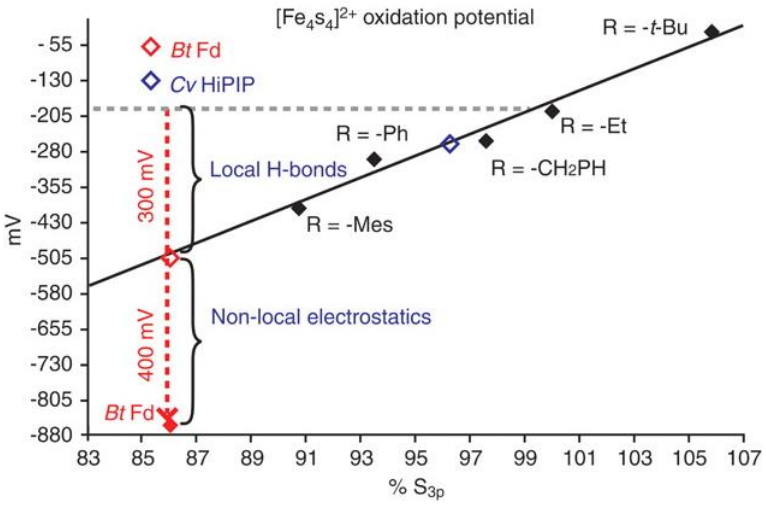

Figure 3. Plot of Fe-S covalency as a function of $[Fe_4S_4]^{2+}$ oxidation potential for a series of $[Fe_4S_4(SR)_4]^{2-}$ complexes with different thiolate ligands (R) (black diamonds). Shown relative to the model complex with R = Et, which has been assigned 100% covalency. Open diamonds represent predicted oxidation potential values based on covalency. From Dey et al. *Science* **2007**, *318*, 1464-1468. Reprinted with permission from AAAS.

5.2 Experimental section

5.2.1 Expression and purification of EndoIII

WT *E. coli* EndoIII was overexpressed in BL21star-(DE3)pLysS cells containing a pET11-ubiquitin-His_6-*nth* construct and purified as detailed previously (*15*), with the exception that the final buffer contained 10% glycerol, rather than 20% glycerol (20 mM sodium phosphate, pH 7.5, 0.5 mM EDTA, 150 mM NaCl, 10% glycerol). EndoIII in this 10% glycerol buffer is stable overnight stored at 4°C, but is less stable in the absence of glycerol; therefore glycerol was not removed until the day of sample preparation. On the day of sample preparation, glycerol was removed from half the volume of protein solution using HiPrep 26/10 desalting column (GE Healthcare) equilibrated with a buffer containing 20 mM sodium phosphate, pH 7.5, 0.5 mM EDTA, 150 mM NaCl. Next, the protein solutions either containing 10% glycerol or no glycerol were separately concentrated. First, 10,000 MWCO Amicon Ultra 15 mL centrifugation filter units (Millipore) were used to concentrate each protein solution to 1 mL or less. Finally, 10,000 MWCO Amicon Ultra 0.5 mL centrifugation filter units (Millipore) were used to concentrate the protein solutions until very dark colored, to approximately 300 µL each if using an entire protein preparation from 6 L of bacterial culture.

5.2.2 Sample preparation

DNA strands were purchased from Integrated DNA Technologies (a 20-mer mixed sequence strand: 5′-GTGAGCTAACGTGTCAGTAC-3′ and its complement). DNA strands (5 µmol) were resuspended in MilliQ water (200 µL, divided into 100 µL aliquots)

and purified by ethanol precipitation. Briefly, 1000 µL of cold 200 proof ethanol, followed by 50 µL of 3 M NaCl were added to the 100 µL DNA solutions and vortexed; the DNA should precipitate. Solutions were then frozen in liquid nitrogen for approximately 5 minutes and spun at 16,000 RCF to pellet the DNA. Finally, the supernatant was removed and the pellet dried on a speed-vac. When dried, the strands were resuspended in 20 mM sodium phosphate, pH 7.5, 0.5 mM EDTA, 150 mM NaCl, either with 10% glycerol or lacking glycerol and quantified based on calculated ε_{260} values for the strands (Integrated DNA Technologies) of 197,800 $M^{-1}cm^{-1}$ for the 20-mer strand and 190,200 $M^{-1}cm^{-1}$ for its complement. Annealing of the strands to form duplexed DNA was accomplished by combining equimolar amounts of the single-stranded DNAs, heating at 90°C for 5 minutes, and slow cooling to room temperature. Separate duplex solutions were prepared in either 10% glycerol or no glycerol buffer.

On the same day as glycerol removal from half of the EndoIII protein solution, and after concentration of the separate 10% glycerol and no glycerol protein solutions, a 4Fe4S cluster loading ratio was calculated for each solution. This calculation is based on the characteristic UV-Visible absorbance at 410 nm of 4Fe4S clusters (Figure 4). To calculate a loading ratio, the concentration of each solution was measured by two separate methods: using ε_{410} = 17,000 $M^{-1}cm^{-1}$, which is specific to the presence of 4Fe4S clusters, and using the Bradford assay, which measures total protein content irrespective of the presence of an iron-sulfur cluster. The 4Fe4S cluster loading ratio was then calculated as: [Protein concentration

based on A_{410}] / [Protein concentration based on Bradford assay] * 100. Typical cluster loading ratios for WT EndoIII were 70-75%.

Finally, to prepare the samples, concentrated solutions of EndoIII protein were mixed with the DNA duplex at a ratio of 1 mol EndoIII: 20 mol base-pairs DNA. An equivalent volume of buffer was added to EndoIII alone solutions so that for each condition (10% glycerol or no glycerol), identical concentrations of EndoIII solutions were prepared both with and without DNA. Mixtures were allowed to incubate on wet ice for 30 minutes to allow for binding before freezing in liquid nitrogen. No glycerol samples were then placed on a lyophilizer, while solution samples were stored in a -80°C freezer. When the lyophilized samples were dried, both samples were placed on dry ice and sent to Stanford University for XAS measurements.

5.2.3 X-ray absorbance spectroscopy

Lyophilized samples were ground to a fine powder, dispersed as thinly as possible on Kapton tape to minimize possible self-absorption fluorescence effects, and mounted across the window of an aluminum plate. Solution samples were loaded via a syringe into 50 µL Teflon cells with Kapton tape as the back window and 6 µm polypropylene as the front window. Measurements were performed at the Stanford Synchrotron Radiation Laboratory (SSRL) on beam line 4-3. Details of the beamline configuration have been described previously (*12*). A shutter was added between the ionization chamber for incident beam intensity and the sample box in order to decrease photoreduction. The solution samples were measured at a constant temperature of 4°C during data collection using a controlled

flow of He gas, pre-cooled by liquid N_2. The photon energy was calibrated to the maximum of the first pre-edge feature of $Na_2S_2O_3 \cdot 5H_2O$ at 2472.02 eV. Three to five scans were measured on the sample to ensure reproducibility. Raw data were calibrated and averaged using MAVE in the EXAFSPAK package. By using the PySpline program (*16*), the background was subtracted from all spectra by fitting a second-order polynomial to the pre-edge region and subtracting it from the entire spectrum. Normalization of the data was accomplished by fitting a straight line to the post-edge region and normalizing the edge jump to 1.0 at 2490.0 eV. For protein samples which also have sulfur-containing free cysteine and methionine residues, it is also necessary to normalize for the total number of sulfur atoms in the protein. EndoIII has 3 free cysteine residues (not coordinating the 4Fe4S cluster), and 2 methionine residues. Finally, the data were normalized with the 4Fe4S cluster loading ratio that is calculated as described above. The error from background subtraction and normalization is less than 1%. Intensities of the pre-edge features were quantified by fitting the data with pseudo-Voigt line shapes with a fixed 1:1 ratio of Lorentzian to Gaussian contributions, using the EDG_FIT program (*17*). The error from the fitting procedure is less than 1%. The fitted intensities were converted to %S 3p character according to previously described methods (*18*).

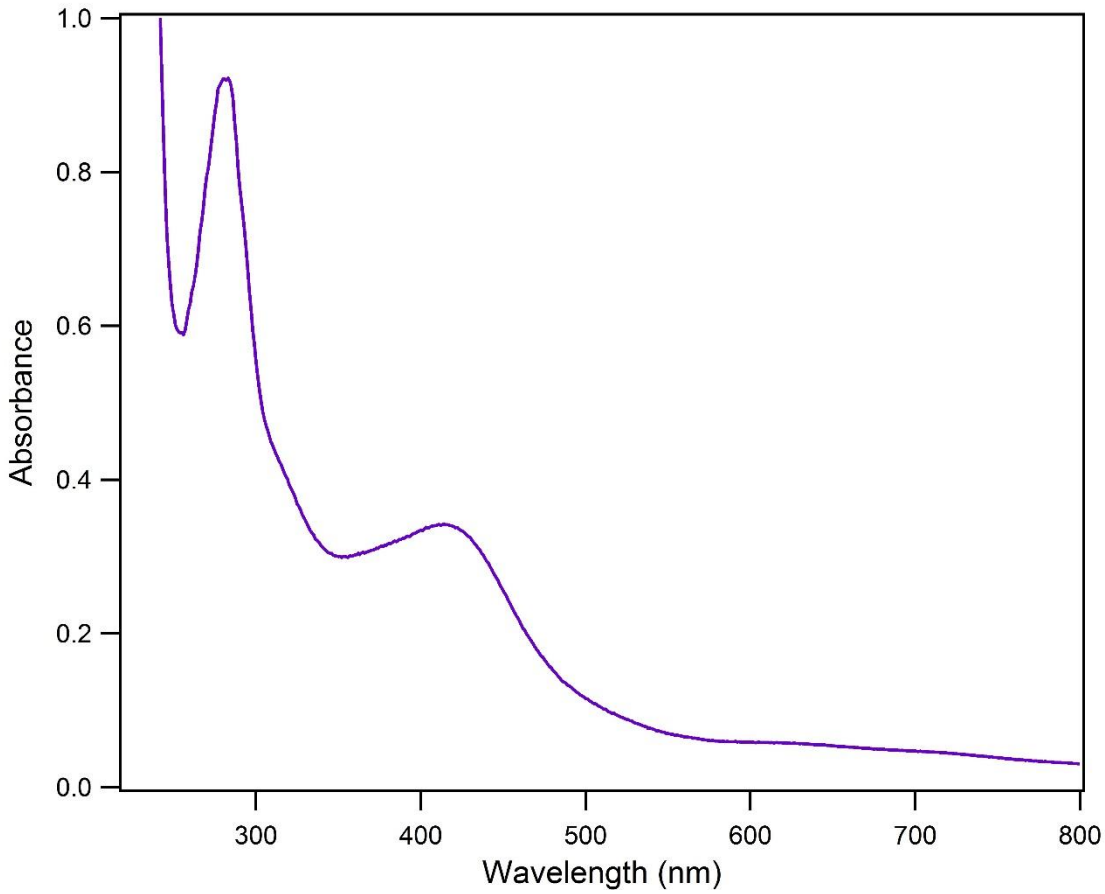

Figure 4. UV-Visible absorbance spectrum of *E. coli* EndoIII showing the shoulder at 410 nm characteristic of a 4Fe4S cluster. Buffer: 20 mM sodium phosphate, pH 7.5, 0.5 mM EDTA, 150 mM NaCl, 20% glycerol.

5.3 Results and discussion

The sulfur K-edge XAS spectra of EndoIII alone and in the presence of a 20-mer mixed sequence DNA duplex (5′-GTGAGCTAACGTGTCAGTAC-3′) at a ratio of 1 mol protein to 20 mol base-pairs was measured both in solution and in samples that had been lyophilized. High protein concentrations (1 mM or greater) are necessary for high quality data. Identical concentrations of EndoIII were compared with and without DNA, for both solution and lyophilized samples. The data were normalized according to a 4Fe4S cluster loading ratio, calculated as the protein concentration based on ε_{410} = 17,000 $M^{-1}cm^{-1}$, specific for the presence of a 4Fe4S cluster, relative to the total protein concentration as measured by the Bradford assay. Typical cluster loading ratios were 70% or greater. The normalized data of the pre-edge $S_{1s} \rightarrow Fe_{3d}$ transition are shown in Figure 5.

For both solution and lyophilized samples, an increase in the area of the pre-edge feature was observed upon DNA binding, indicating an increase in Fe-S covalency. This result is consistent with a negative shift in the redox potential of the $[4Fe4S]^{3+/2+}$ couple of EndoIII upon DNA binding, as we have observed electrochemically (*4*). A larger increase in covalency upon DNA binding is observed with solution samples, indicating that hydration is an important factor. DNA binding shifts the cluster into a more buried, less solvent-accessible environment. In lyophilized samples, where solvent has been removed, we still observe an increase in Fe-S covalency upon DNA binding: this can likely be attributed to the non-local electrostatics of the DNA poly-anion. Additionally, lower Fe-S covalency is observed upon lyophilization for both EndoIII alone and EndoIII with DNA samples. This

decrease in covalency upon lyophilization is also evident with HiPIP from *C. vinosum* (unpublished observations).

While quantitation is still preliminary, the EndoIII with DNA sample in solution has the same covalency (100% S_{3p}) as the reference model complex $[Fe_4S_4(SEt)_4]^{2-}$ in the work of Solomon *et al.* (*14*). In the EndoIII alone sample, the covalency is decreased to 93% relative to the model complex. Based on the slope that defines the relationship between covalency and $[4Fe4S]^{3+/2+}$ oxidation potential, this 7% difference would correspond to an approximately 150 mV decrease in the redox potential of the $[4Fe4S]^{3+/2+}$ couple of EndoIII upon binding DNA, remarkably similar to that observed electrochemically. The absolute values of the $[4Fe4S]^{3+/2+}$ potentials do not fall along the line in Figure 3, likely due to non-local electrostatics.

This result has been reproduced in two separate trials. In a third trial, a smaller decrease in Fe-S covalency was observed upon EndoIII binding DNA. However, in this trial, no difference was observed between the lyophilized and solution samples, suggesting that the samples had been damaged in some way. Therefore data from this trial was deemed not reliable.

Sheila David and co-workers have also participated in this collaboration, performing similar studies with the homologous 4Fe4S cluster-containing BER protein MutY (data not shown). Similar results were obtained for both EndoIII and MutY. An increase in Fe-S covalency upon DNA binding is observed for both solution and lyophilized samples that indicates a negative shift in the redox potential of the $[4Fe4S]^{3+/2+}$ cluster of MutY in the

presence of DNA. Furthermore, lower Fe-S covalency is observed upon lyophilization for both MutY alone and MutY with DNA samples, as with EndoIII. Overall, the trend of increasing Fe-S covalency upon DNA binding is consistent: (*i*) in duplicate trials, (*ii*) with both EndoIII and MutY, and (*iii*) with our previously observed DNA electrochemistry results.

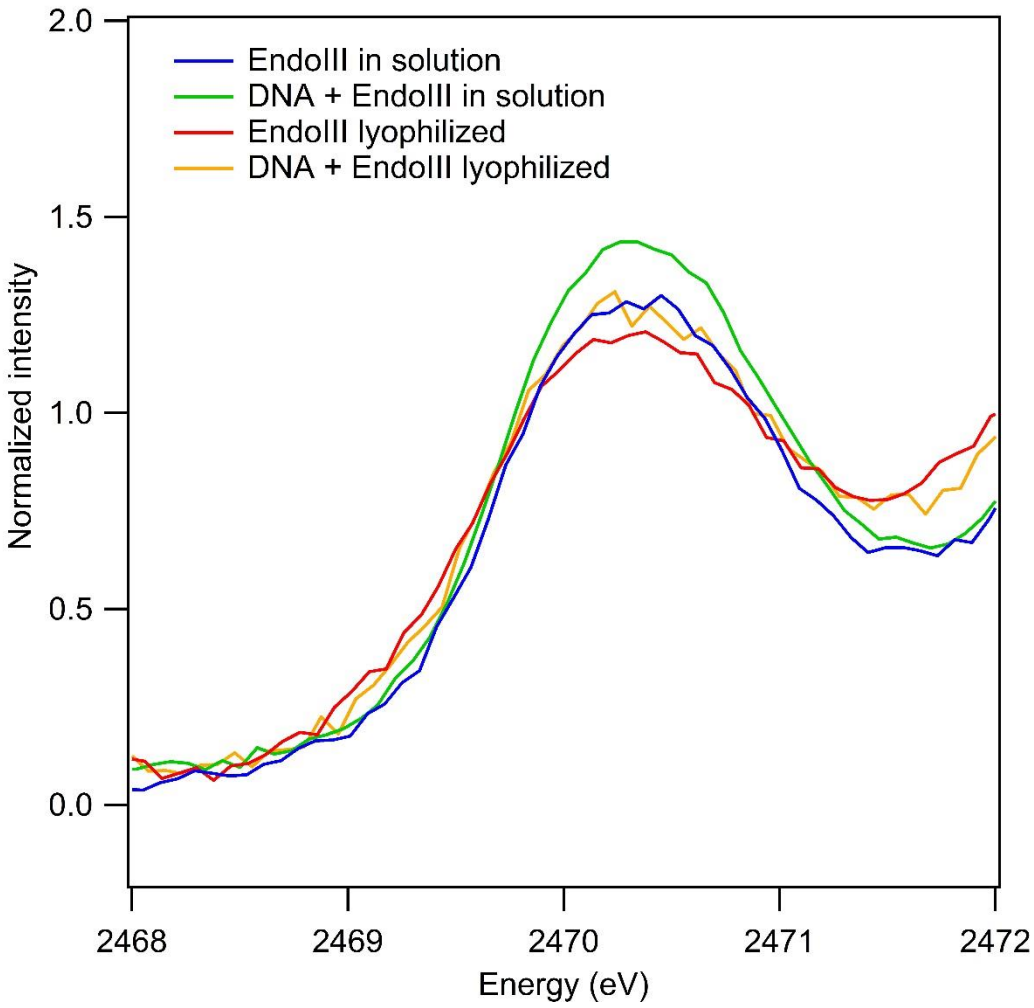

Figure 5. Sulfur K-edge XAS spectra of EndoIII alone and in the presence of a 20-mer mixed sequence DNA duplex (1 mol protein: 20 mol base-pairs), both in solution and lyophilized. Sequence of duplex: 5′-GTGAGCTAACGTGTCAGTAC-3′. Lyophilized samples: 71% cluster loading; before freezing, concentrations: EndoIII: 1.00 mM (based on A_{410}), 1.00 mM DNA duplex (20 mM base-pairs). Solution samples: 72% cluster loading; concentrations: EndoIII: 1.25 mM (based on A_{410}), 1.25 mM DNA duplex (25 mM base-pairs). Buffer: 20 mM sodium phosphate, pH 7.5, 150 mM NaCl, 0.5 mM EDTA, either with 10% glycerol (solution samples) or in the absence of glycerol (lyophilized samples).

5.4 Conclusions

Sulfur K-edge XAS can be used to directly probe the iron-sulfur covalency in 4Fe4S clusters via a pre-edge transition that gains intensity if sulfur 3p orbitals mix with Fe 3d orbitals. This Fe-S covalency has been correlated with the redox potential of 4Fe4S clusters, thus allowing quantitative examination of the electrostatic environment of the cluster under different conditions. Here with the 4Fe4S cluster-containing BER protein EndoIII we have reproducibly shown an increase in Fe-S covalency upon DNA binding, both in solution and lyophilized samples. This covalency increase is consistent with a negative shift in the redox potential of the EndoIII $[4Fe4S]^{3+/2+}$ couple of approximately 150 mV upon DNA binding. Thus the shift in Fe-S covalency upon DNA binding as measured by XAS agrees with previous electrochemistry results. Moreover, the same trend is observed in MutY, a homologous 4Fe4S cluster BER protein. Therefore we have obtained direct molecular evidence for the negative shift in the $[4Fe4S]^{3+/2+}$ cluster redox potential of BER proteins upon DNA binding. These data support the feasibility of our model whereby these proteins can utilize DNA charge transport to cooperate in order to efficiently find DNA lesions inside cells.

References

1. Kim, Y.J.; Wilson, D.M. 3rd. Overview of base excision repair biochemistry. *Curr. Mol. Pharmacol.* **2012**, *5*, 3-13.

2. Cunningham, R.P., Asahara, H., Bank, J.F., Scholes, C.P., Salerno, J.C., Surerus, K., Munck, E., McCracken, J., Peisach, J., and Emptage, M.H. Endonuclease III is an iron-sulfur protein. *Biochemistry* **1989**, *28*, 4450-4455.

3. Porello, S.L.; Cannon, M.J.; David, S.S. A substrate recognition role for the $[4Fe\text{-}4S]^{2+}$ cluster of the DNA repair glycosylase MutY. *Biochemistry* **1998**, *37*, 6465-6475.

4. Gorodetsky, A.A.; Boal, A.K.; Barton, J.K. Direct electrochemistry of Endonuclease III in the presence and absence of DNA *J. Am. Chem. Soc.* **2006**, *128*, 12082-12083.

5. Muren, N.B.; Olmon, E.D.; Barton, J.K. Solution, surface, and single molecule platforms for the study of DNA-mediated charge transport. *Phys. Chem. Chem. Phys*. **2012**, *14*, 13754-13771.

6. Boal, A.K.; Yavin, E.; Lukianova, O.A.; O'Shea, V.L.; David, S.S.; Barton, J.K. DNA-bound redox activity of DNA repair glycosylases containing [4Fe-4S] clusters. *Biochemistry* **2005**, *44*, 8397-8407.

7. Stephens, P.J.; Jollie, D.R.; Warshel, A. Protein control of redox potentials of iron-sulfur proteins. *Chem. Rev*. **1996**, *96*, 2491-2513.

8. Mui, T.P.; Fuss, J.O.; Ishida, J.P.; Tainer, J.A.; Barton, J.K. ATP-stimulated, DNA-mediated redox signaling by XPD, a DNA repair and transcription helicase. *J. Am. Chem. Soc.* **2011**, *133*, 16378-16381.

9. Grodick, M.A.; Segal, H.M.; Zwang, T.J.; Barton, J.K. DNA-mediated signaling by proteins with 4Fe-4S clusters is necessary for genomic integrity. *J. Am. Chem. Soc.* **2014**, *136*, 6470-6478.

10. Wan, C.; Fiebig, T.; Kelley, S.O.; Treadway, C.R.; Barton, J.K.; Zewail, A.H. Femtosecond dynamics of DNA-mediated electron transfer. *Proc. Natl. Acad. Sci. USA* **1999**, *96*, 6014-6019.

11. Boal, A.K.; Genereux, J.C.; Sontz, P.A.; Gralnick, J.A.; Newman, D.K.; Barton, J.K. Redox signaling between DNA repair proteins for efficient lesion detection *Proc. Natl. Acad. Sci. USA* **2009**, *106*, 15237-15242.

12. Solomon, E.I.; Hedman, B.; Hodgson, K.O.; Dey, A.; Szilagyi, R.K. Ligand K-edge X-ray absorption spectroscopy: covalency of ligand-metal bonds. *Coord. Chem. Rev*. **2005**, *249*, 97-129.

13. Bencze, K.Z.; Kondapalli, K.C.; Stemmler, T.L. X-Ray Absorption Spectroscopy. In *Applications of Physical Methods to Inorganic and Bioinorganic Chemistry*; Scott, R.A. and Lukehart, C.M., Ed.; Wiley, 2007; p. 513-528.

14. Dey, A.; Jenney, F.E. Jr.; Adams, M.W.W.; Babini, E.; Takahashi, Y.; Fukuyama, K.; Hodgson, K.O.; Hedman, B.; Solomon, E.I. Solvent tuning of electrochemical potentials in the active sites of HiPIP versus ferredoxin. *Science* **2007**, *318*, 1464-1468.

15. Pheeney, C.G.; Arnold, A.R.; Grodick, M.A.; Barton, J.K. Multiplexed electrochemistry of DNA-bound metalloproteins. *J. Am. Chem. Soc*. **2013**, *135*, 11869-11878.

16. George, G. N.; Stanford Synchrotron Radiation Laboratory: Menlo Park, CA, 1990.

17. Tenderholt, A. L.; v2.1, Ed.; Stanford University: Stanford, CA, 2007.

18. Sarangi, R.; George, S.D.; Rudd, D.J.; Szilagyi, R.K.; Ribas, X.; Rovira, C.; Almeida, M.; Hodgson, K.O.; Hedman, B.; Solomon, E.I. Sulfur K-Edge X-ray absorption spectroscopy as a probe of ligand–metal bond covalency: Metal vs ligand oxidation in copper and nickel dithiolene complexes. *J. Am. Chem. Soc*. **2007**, *129*, 2316-2326.

Chapter 6

Summary and Perspectives

Decades of research have elucidated many aspects of the phenomenon of DNA charge transport (CT) (*1*). Both electrons and electron holes are efficiently transported through the DNA π-stack over long molecular distances of at least 100 base-pairs. Despite this shallow distance dependence, DNA CT is sensitive to mismatches or lesions that disrupt π-stacking and is critically dependent on proper electronic coupling of the donor and acceptor moieties into the base stack. The mechanism of electron transfer through DNA is best described as incoherent hopping, consisting of multiple superexchange steps between delocalized (approximately 3 base pair) domains of well-coupled stacked bases that are created through conformational dynamics. Favorable DNA CT is very rapid, occurring on the picosecond timescale. Because of this speed, electron holes equilibrate along the DNA π-stack, forming a characteristic pattern of DNA damage at low oxidation potential guanine multiplets.

More recently, research in the Barton laboratory has focused on how DNA CT may be used within a biological context. These studies began with the base excision repair glycosylase enzymes MutY and EndoIII, which contain 4Fe4S clusters whose function was not well understood. While relatively insensitive to oxidation or reduction in solution, experiments on DNA-modified electrodes demonstrated different redox behavior once these proteins bound DNA. Specifically, the $[4Fe4s]^{3+/2+}$ couple of EndoIII negatively shifts by 200 mV upon binding to DNA, bringing this couple into the physiologically relevant range (*2*). A thermodynamic consequence this reduction potential shift is a significantly higher

DNA-binding affinity in the oxidized, $[4Fe4S]^{3+}$ state, rather than the reduced, $[4Fe4S]^{2+}$ state.

Intriguingly, more 4Fe4S cluster DNA processing enzymes, such as the helicases XPD and DinG, have been discovered to have DNA-bound $[4Fe4s]^{3+/2+}$ reduction potentials similar to those of EndoIII and MutY, of approximately 80 mV versus NHE (*3*,*4*). These findings prompted a model whereby DNA processing enzymes with 4Fe4S clusters can perform DNA-mediated electron transfer (ET) self-exchange reactions with other 4Fe4S cluster proteins, even if the proteins are quite dissimilar (from different repair pathways and even different organisms), as long as the DNA-bound $[4Fe4S]^{3+/2+}$ redox potentials are conserved. This mechanism would allow low copy number DNA repair proteins to find their lesions efficiently within the cell. Support for this model began with *in vitro* evidence, such as spectroscopic studies indicating the feasibility of MutY oxidation by guanine radicals (*5*). Grodick *et al.* have now obtained compelling *in vivo* evidence with an InvA *E. coli* strain for the necessity of DNA-mediated communication between EndoIII and DinG in order to maintain genomic stability (*4*).

DNA CT may also be used biologically for the long-range, selective activation of redox-active transcription factors. SoxR is a bacterial transcription factor with a $[2Fe2S]^{2+/+}$ cluster that responds to superoxide stress. Lee *et al.* demonstrated that SoxR can become oxidized, and transcriptionally active, by irradiating a construct with a metallointercalating photooxidant tethered 80 base-pairs from the SoxR promoter binding site (*6*). Thus SoxR can be transcriptionally activated from a distance via oxidation though DNA CT. Work has

also focused on p53, a vital tumor suppressor that contains a network of redox-active cysteine residues that modulate the DNA-binding affinity of p53. Schaefer *et al.* have revealed that sequence selective oxidation of these cysteine residues via DNA CT and subsequent dissociation of p53 is a viable mechanism by which p53 decides cellular fates through selective binding to different promoter sites within the genome (*7*). Overall, current work is now focused on discovering other proteins that may utilize DNA CT within the cell, as well as further elucidating aspects of the DNA-mediated ET self-exchange reaction of 4Fe4S cluster proteins.

Towards this end, we have investigated whether the DNA-binding bacterial ferritin Dps, which is known to protect DNA from oxidative stress, can utilize DNA CT to protect the genome from a distance. Dps proteins are implicated in the survival and virulence of pathogenic bacteria; thus understanding the specific mechanism by which Dps proteins protect the bacterial genome could inform the development of new antibiotics. One aspect of Dps protection involves ferroxidase activity, whereby ferrous iron is bound and oxidized selectively by hydrogen peroxide, thereby preventing formation of damaging hydroxyl radicals via Fenton chemistry; another aspect of this protection is non-specific DNA-binding. We explored the possibility of protection from a distance via DNA CT by using an intercalating ruthenium photooxidant to generate oxidative DNA damage via the flash-quench technique, which localizes to a low potential guanine triplet in mixed sequence DNA. We find that Dps loaded with ferrous iron, in contrast to Apo-Dps and ferric iron-loaded Dps, which lack available reducing equivalents, significantly attenuates the yield of

oxidative DNA damage at the guanine triplet (*8*). These data demonstrate that ferrous iron-loaded Dps is selectively oxidized to fill guanine radical holes, thereby restoring the integrity of the DNA. Luminescence studies indicate no direct interaction between the ruthenium photooxidant and Dps, supporting the DNA-mediated oxidation of ferrous iron-loaded Dps. Thus DNA CT may be a mechanism by which Dps efficiently protects the genome of pathogenic bacteria from a distance.

Further work has focused on spectroscopic characterization of the DNA-mediated oxidation of ferrous iron-loaded Dps. We have found that, because of the difference in affinity at the di-iron ferroxidase site, only the higher affinity iron site is occupied under anaerobic conditions. X-band EPR was used to monitor the oxidation of DNA-bound Dps after DNA photooxidation via the flash-quench technique. Upon irradiation with poly(dGdC)$_2$, a signal arises with $g = 4.3$, consistent with the formation of mononuclear high-spin Fe(III) sites of low symmetry, the expected oxidation product of Dps with one iron bound at each ferroxidase site. When poly(dGdC)$_2$ is substituted with poly(dAdT)$_2$, the yield of Dps oxidation is decreased significantly, indicating that guanine radicals facilitate Dps oxidation. The more favorable oxidation of Dps by guanine radicals supports the feasibility of a long-distance protection mechanism via DNA CT where Dps is oxidized to fill guanine radical holes in the bacterial genome produced by reactive oxygen species.

We have also explored possible electron transfer intermediates in the DNA-mediated oxidation of ferrous iron-loaded Dps. Dps proteins contain a conserved tryptophan residue in close proximity to the ferroxidase site (W52 in *E. coli* Dps) that it located between the

iron site and the protein surface. In comparison to WT Dps, in EPR studies of the oxidation of ferrous iron-loaded Dps following DNA photooxidation, W52Y and W52A mutants were deficient in forming the characteristic EPR signal at $g = 4.3$, with a larger deficiency for W52A compared to W52Y. In addition to EPR, we also probed the role of W52 Dps in cells using a hydrogen peroxide survival assay. Cells with W52Y Dps survived the hydrogen peroxide challenge more similarly to those containing WT Dps, whereas cells with W52A Dps died off as quickly as cells without Dps. Combined, these results suggest the possibility of W52 as a CT hopping intermediate.

Overall, we have discovered that the DNA-binding bacterial ferritin Dps can protect the bacterial genome from a distance via DNA CT, perhaps contributing to pathogen survival and virulence. We have spectroscopically confirmed the oxidation of *E. coli* Dps following DNA photooxidation with the flash-quench technique, suggested the possibility of an ET hopping intermediate, and moved towards understanding the role of DNA CT with Dps in inside cells. More work is required to fully elucidate the roles of Dps *in vivo*.

DNA-modified electrodes have become an essential tool for the study of the redox chemistry of DNA processing enzymes with 4Fe4S clusters. In many cases, it is necessary to investigate different complex samples and substrates in parallel in order to elucidate this chemistry. Therefore, we optimized and characterized a multiplexed electrochemical platform with the 4Fe4S cluster base excision repair glycosylase Endonuclease III (EndoIII) (*9*). Closely packed DNA films, where the protein has limited surface accessibility, produce EndoIII electrochemical signals sensitive to an intervening mismatch, indicating a DNA-

mediated process. Multiplexed analysis allowed more robust characterization of the CT-deficient Y82A EndoIII mutant, as well as comparison of a new family of mutations altering the electrostatics surrounding the [4Fe-4S] cluster in an effort to shift the reduction potential of the cluster. While little change in the DNA-bound midpoint potential was found for this family of mutants, likely indicating the dominant effect of DNA-binding on establishing the protein redox potential, significant variations in the efficiency of DNA-mediated electron transfer were apparent. On the basis of the stability of these proteins, examined by circular dichroism, we proposed that the electron transfer pathway in EndoIII can be perturbed not only by the removal of aromatic residues but also through changes in solvation near the cluster.

Other work has also focused on elucidating important factors in the DNA-mediated ET self-exchange reaction of 4Fe4S cluster proteins. While a reduction potential shift upon DNA binding has been demonstrated with electrochemistry experiments, these studies do not provide direct molecular evidence for the species being observed. In contrast, sulfur K-edge X-ray absorbance spectroscopy (XAS) can be used to probe directly the covalency of iron-sulfur clusters, which is correlated to their reduction potential (*10*). We have shown that the Fe-S covalency of the 4Fe4S cluster of EndoIII increases upon DNA binding, stabilizing the oxidized $[4Fe4S]^{3+}$ cluster, consistent with a negative shift in reduction potential. The 7% increase in Fe-S covalency corresponds to an approximately 150 mV shift, remarkably similar to DNA electrochemistry results. Therefore we have obtained direct molecular evidence for the shift in 4Fe4S reduction potential of EndoIII upon DNA

binding, supporting the feasibility of our model whereby these proteins can utilize DNA CT to cooperate in order to efficiently find DNA lesions inside cells.

These studies contribute to the understanding of possible DNA-mediated protein oxidation within cells. More work is necessary in the future to characterize the kinetics of DNA-protein electron transfer. Previous work has been limited by the time resolution of a diffusing quencher. Time-resolved infrared (TRIR) studies with proteins containing IR-active ligands appended to the iron-sulfur cluster may provide detailed kinetic information at fast timescales (picoseconds). Furthermore, research is ongoing regarding how other DNA processing enzymes with 4Fe4S clusters, such as primase and DNA polymerase, may use DNA CT in a cellular context. Finally, new families of proteins that may utilize this chemistry await discovery. For example, the MarR family of transcriptional repressors dissociate from DNA upon the oxidation of redox-active cysteine residues, allowing expression of various virulence factors and antibiotic resistance genes. These small proteins respond to a diverse array of structures under physiological conditions, prompting the question of secondary signals (*11*). Could these secondary signals be long distance oxidation via DNA CT?

References

1. Genereux, J.C.; Barton, J.K. Mechanisms for DNA charge transport. *Chem. Rev*. **2010**, *110*, 1642-1662.

2. Gorodetsky, A.A.; Boal, A.K.; Barton, J.K. Direct electrochemistry of Endonuclease III in the presence and absence of DNA *J. Am. Chem. Soc.* **2006**, *128*, 12082-12083.

3. Mui, T.P.; Fuss, J.O.; Ishida, J.P.; Tainer, J.A.; Barton, J.K. ATP-stimulated, DNA-mediated redox signaling by XPD, a DNA repair and transcription helicase. *J. Am. Chem. Soc.* **2011**, *133*, 16378-16381.

4. Grodick, M.A.; Segal, H.M.; Zwang, T.J.; Barton, J.K. DNA-mediated signaling by proteins with 4Fe-4S clusters is necessary for genomic integrity. *J. Am. Chem. Soc.* **2014**, *136*, 6470-6478.

5. Yavin, E.; Boal, A.K.; Stemp, E.D.A.; Boon, E.M.; Livingston, A.L.; O'Shea, V.L.; David, S.S.; Barton, J.K. Protein-DNA charge transport: Redox activation of a DNA repair protein by guanine radical. *Proc. Nat. Acad. Sci. USA* **2005**, *102*, 3546-3551.

6. Lee, P.E.; Demple, B.; Barton, J.K. DNA-mediated redox signaling for transcriptional activation of SoxR. *Proc. Natl. Acad. Sci. USA* **2009**, *106*, 13164-13168.

7. Schaefer, K.N.; Barton, J.K. DNA-mediated oxidation of p53. *Biochemistry* **2014**, *53*, 3467-3475.

8. Arnold, A.R.; Barton, J.K. DNA protection by the bacterial ferritin Dps via DNA charge transport. *J. Am. Chem. Soc.* **2013**, *135*, 15726-15729.

9. Pheeney, C.G.; Arnold, A.R.; Grodick, M.A.; Barton, J.K. Multiplexed electrochemistry of DNA-bound metalloproteins. *J. Am. Chem. Soc.* **2013**, *135*, 11869-11878.

10. Dey, A.; Jenney, F.E. Jr.; Adams, M.W.W.; Babini, E.; Takahashi, Y.; Fukuyama, K.; Hodgson, K.O.; Hedman, B.; Solomon, E.I. Solvent tuning of electrochemical potentials in the active sites of HiPIP versus ferredoxin. *Science* **2007**, *318*, 1464-1468.

11. Chen, P.R.; Brugarolas, P.; He, C. Redox signaling in human pathogens. *Antioxid. Redox Signal.* **2011**, *14*, 1107-1118.